

UNIVERSITY OF BELGRADE
School of Electrical Engineering

UNIVERSITY OF ANTWERP
Department of Physics

Nemanja A. Čukarić

Modelling the electron and hole states
in semiconductor nanostructures by the
multiband $k \cdot p$ theory

Doctoral dissertation

Belgrade, 2015.

UNIVERZITET U BEOGRADU
Elektrotehnički fakultet

UNIVERZITET U ANTVERPENU
Departman za fiziku

Nemanja A. Čukarić

Modelovanje elektronskih i šupljinskih
stanja u poluprovodničkim nanostrukturama
pomoću višezonske k·p teorije

Doktorska disertacija

Beograd, 2015.

Committee members

Supervisors:

Dr. Milan Ž Tadić - full professor, School of Electrical Engineering, University of Belgrade, Serbia

Dr. François M. Peeters - full professor, Department of Physics, University of Antwerp, Belgium

Members:

Dr Dejan Gvozdić - full professor, School of Electrical Engineering, University of Belgrade, Serbia

Dr Bart Partoens - full professor, Department of Physics, University of Antwerp, Belgium

Dr Vladimir Arsoški - assistant professor, School of Electrical Engineering, University of Belgrade, Serbia

Date of the defense:

To Sanja

Acknowledgements

First of all, I would like to express my deepest gratitude to my supervisor from the University of Belgrade, Prof. Milan Tadić, for introducing and guiding me through the interesting areas of nanoscale physics and nanoelectronics. His advices, enthusiasm, and knowledge, which he unselfishly shared, have been invaluable. I also thank him for having faith in me, even when I did not. The last 8 years, during which we have collaborated, have indeed been an enriching experience for me. Above all, I appreciate his human qualities, and feel lucky for having the opportunity to work with him.

I am also grateful to Prof. François Peeters, my supervisor from the University of Antwerp, for offering me the opportunity to be a member of his group. During the stays at the UA I got benefit of his immense knowledge in condensed matter physics and nanoscale systems, vast research experience, and unprecedented open-mindedness. As a consequence, it gave a substantial impetus to my work. I especially mention his help during preparing the results of my research for publications. Moreover, I express my gratitude for his useful remarks and help in preparing the final version of the text of the thesis. To summarize, working with Prof. Peeters has been very inspiring experience for me.

I am very thankful to Prof. Bart Partoens for the help during my work on the silicon nanostructures modelling. We exchanged many ideas regarding the 30-band $\mathbf{k} \cdot \mathbf{p}$ modeling. I enjoyed working in his neighbourhood, since it allowed me to discuss many interesting topics in physics of nanostructures in a very creative manner. I was indeed able to catch his view and ideas very fast, which strengthen our connection during the work on the thesis. Also, his suggestions and comments helped me to improve the research papers on silicon quantum wells. Finally, I have to express the hope that we will continue collaborating in future.

I thank my colleague and friend Prof. Vladimir Arsoški for making calculations of the mechanical strain distributions in quantum dots. Also, we had numerous gatherings when we discussed subtle points of the $\mathbf{k} \cdot \mathbf{p}$ theory. Those discussions improved considerably my understanding of the theory. We indeed took every opportunity to get into a very detail of each feature that appeared in my calculations.

I owe my deepest gratitude to my parents, Aleksandar and Slađana, and sister Jovana, for the constant support and encouragement during my studies.

Finally, I thank my wife Sanja for the joy of life. The thesis is dedicated to her.

Modelling the electron and hole states in semiconductor nanostructures by the multiband $\mathbf{k} \cdot \mathbf{p}$ theory

Abstract. The dissertation presents a study of the electron and hole states in various semiconductor nanostructures using the $\mathbf{k} \cdot \mathbf{p}$ formalism. Si/SiO₂ quantum wells, GaAs/(Al,Ga)As quantum wells, GaAs/(Al,Ga)As ringlike quantum dots grown by droplet epitaxy, and ringlike (In,Ga)As/GaAs quantum dots formed by epitaxy in the Stranski-Krastanov mode are all considered. An overview of the techniques which are used to fabricate the analyzed nanostructures is first given. The most basic properties of the electronic structure of silicon and III-V compounds are briefly described.

The fundamentals of the $\mathbf{k} \cdot \mathbf{p}$ theory are explained, and then applied to derive the equations of the single-band effective-mass theory. The $\mathbf{k} \cdot \mathbf{p}$ theory for degenerate energy levels, which is the case in the valence band of diamond and zinc-blende semiconductors, is then presented. By using the perturbation theory, the three-band Dresselhaus-Kip-Kittel model of the valence-band states is derived for the case of absent spin-orbit interaction. The spin-orbit interaction is taken into account in the 6-band Luttinger-Kohn model, whose derivation is also briefly described. The conduction and valence band states of wide band-gap direct semiconductors and their nanostructures are usually well described by the single-band effective-mass theory and the 6-band Luttinger-Kohn model, respectively. The mentioned $\mathbf{k} \cdot \mathbf{p}$ models are well suited for low \mathbf{k} states, whereas they cannot be straightforwardly adopted to model states which are far away from the Γ point. Such a situation arises in silicon, where low energy states in the conduction band have large \mathbf{k} . The model which has recently been proposed to handle such a situation is the 30-band $\mathbf{k} \cdot \mathbf{p}$ theory. It is the full-zone approach, which provides an accurate description of the electronic structure of both direct and indirect semiconductors in the whole Brillouin zone. The envelope function approximation, which is a way to apply the $\mathbf{k} \cdot \mathbf{p}$ theory to nanostructures, is also briefly discussed. Also, it is demonstrated how effects of magnetic

field and mechanical strain are modelled in the $\mathbf{k} \cdot \mathbf{p}$ theory. When applied to nanostructures, the multiband $\mathbf{k} \cdot \mathbf{p}$ theory could give rise to spurious solutions, which are an artifact due to an incomplete description of the electronic structure by the $\mathbf{k} \cdot \mathbf{p}$ theory. In practice, spurious solutions are difficult to control, and therefore could make havoc in electronic structure computation. Therefore, spurious solutions, their effects, and possible ways to control them are discussed.

The 30-band and 6-band $\mathbf{k} \cdot \mathbf{p}$ models are applied to electronic-structure calculations of the Si/SiO₂ quantum wells. The hard-wall confinement potential is assumed, and the conduction and valence band states are both calculated using the 30-band model. A wave function is expanded into the basis consisting of standing waves. Numerous spurious solutions in the conduction-band and valence-band energy spectra are found and are identified to be of two types: 1) spurious states which have large contributions of the bulk solutions with large wave vectors (the high- k spurious solutions), and 2) states which originate mainly from the spurious valley outside the Brillouin zone (the extra-valley spurious solutions). An algorithm to remove all those nonphysical solutions from the electron and hole energy spectra is proposed. Furthermore, slow and oscillatory convergence of the hole energy levels with the number of basis functions is found and is explained by the peculiar band mixing and the confinement in the considered quantum well. We discovered that assuming the hard-wall potential leads to numerical instability of the hole states computation. Nevertheless, allowing the envelope functions to exponentially decay in a barrier of finite height is found to improve the accuracy of the computed hole states.

The interband optical absorption in Si/SiO₂ quantum wells is calculated as function of the well width (W) and the evolution from an indirect to a direct gap material as function of the well width is investigated. In order to compute the electron states in the conduction band, the 30-band $\mathbf{k} \cdot \mathbf{p}$ model is employed, whereas the 6-band Luttinger-Kohn model is used for the hole states. We found that the effective direct band gap in the quantum well agrees very well with the W^{-2} scaling result of the single-band model. The interband matrix elements for linear polarized light oscillate with the quantum well width, which agrees qualitatively with a single band calculation. Our theoretical results indicate that the absorption can be maximized by a proper choice of the well width. However, the obtained absorption coefficients are at least an order of magnitude smaller than for a typical direct

semiconductor.

The models of the electron and hole states which were developed for the silicon quantum wells were then adopted to compute the electron and hole states in GaAs/(Al,Ga)As quantum wells. The conduction-band states are computed by the effective-mass model, and those results are compared with the results obtained by means of the 30-band model. Similarly, the hole states are computed by both the 6-band and the 30-band $\mathbf{k} \cdot \mathbf{p}$ theory, and the results of the two computations are compared. The discrepancy of the results of both the single-band and the 6-band $\mathbf{k} \cdot \mathbf{p}$ theory from the results of the 30-band calculation is found to be smaller for wider quantum wells. It is a consequence of the fact that all 3 models are well suited for modelling states in the bulk GaAs around Γ point. Also, as could be *a priori* inferred, the $\mathbf{k} \cdot \mathbf{p}$ models are found to deliver states which deviate less from the results of the 30-band model when the in-plane wave vector k_{\parallel} is smaller. And agreement between the single-band model and the 30-band model is better for low energy subbands, when the states are composed of low k_z bulk solutions. The same applies to the valence band states extracted from the 6-band calculations. Moreover, it is found that the 6-band models exhibits better agreement with the 30-band theory than the single-band theory. Also, the Dresselhaus spin-orbit splitting in the conduction band is calculated using the 30-band model and the approximate 2-band model. We show that there is qualitative agreement between these two models, but the 2-band model is found to overestimate the SO splitting.

In the second part of the thesis we investigate the ringlike quantum dots, which are grown by either droplet epitaxy or in the Stranski-Krastanov mode. These quantum dots are assumed to have shapes similar to rings, but lacking the ring opening. The simplified model, which consists of a disk and a ring surrounding it, is proposed. The whole system is embedded in higher-bandgap material, and its shape resembles realistic ring structures grown by the droplet epitaxy technique. We first consider unstrained GaAs/(Al,Ga)As quantum dots. The conduction-band states in the structure are modeled by the single-band effective-mass theory, while the 4-band Luttinger-Kohn model is adopted to compute the valence-band states. We analyze how the electronic structure of the ringlike structure evolves from the one of a quantum ring when the size of either the disk or the ring is changed. For that purpose, 1) the width of the ring, 2) the disk radius, and 3)

the disk height are separately varied. For dimensions typical for experimentally realized structures, we find that the electron wavefunctions are mainly localized inside the ring, even when the thickness of the inner layer is 90% of the ring thickness. These calculations indicate that topological phenomena, like Aharonov-Bohm effect, could emerge in experiments even when the layer inside the ring is present.

The magnetic-field dependence of the hole states in ringlike quantum dots is also determined by the Luttinger-Kohn model for the unstrained GaAs/(Al,Ga)As and the strained (In,Ga)As/GaAs systems. Aharonov-Bohm oscillations due to angular momentum transitions of the hole ground state appear with periods that vary with the thickness of the disk. The strain in the (In,Ga)As/GaAs quantum dot is sensitive to the disk thickness and favors the spatial localization of the heavy holes inside the disk. Therefore, the angular momentum transitions between the valence-band states disappear for much thinner disks than in the case of the unstrained GaAs/(Al,Ga)As ringlike quantum dots. In both systems, the oscillations in the energy of the hole ground state are found to disappear for thinner inner layer than in the electron ground-state energy. This is due to the different confining potentials and the mixing between the heavy- and light-hole states. As a consequence, magnetization of the single hole is found to strongly depend on the bottom thickness of the strained (In,Ga)As/GaAs quantum dot. Furthermore, we found that the strain can lead to a spatial separation of the electron and the hole, as in type-II band alignment, which is advantageous for the appearance of the excitonic Aharonov-Bohm effect.

The main results and contributions of the thesis are eventually summarized and the conclusions are made.

Keywords: silicon, III-V compounds, quantum well, quantum dot, quantum ring, $\mathbf{k} \cdot \mathbf{p}$ theory, multiband, 30-band Hamiltonian, optical absorption, Aharonov-Bohm effect

Scientific field: Electrical and Computer Engineering

Research area: Nanoelectronics and Photonics

UDC number: 621.3

Modelovanje elektronskih i šupljinskih stanja u poluprovodničkim nanostrukturama pomoću višezonske $\mathbf{k} \cdot \mathbf{p}$ teorije

Rezime: Disertacija predstavlja analizu elektronskih i šupljinskih stanja u različitim nanostrukturama korišćenjem $\mathbf{k} \cdot \mathbf{p}$ formalizma. Razmatrane su Si/SiO₂ kvantne jame, GaAs/(Al,Ga)As kvantne jame, prstenolike GaAs/(Al,Ga)As kvantne tačke formirane metodima kapljične epitaksije i (In,Ga)As/GaAs kvantne tačke proizvedene epitaksijom u Stranski-Krastanov modu. Dat je pregled tehnika fabrikacije koje se obično koriste za proizvodnju razmatranih nanostrukture. Osnovna svojstva elektronske strukture silicijuma i III-V jedinjenja su takođe ukratko razmatrana.

Zatim su predstavljeni osnovi $\mathbf{k} \cdot \mathbf{p}$ teorije. Prvo je prikazan koncept ove teorije, a zatim je $\mathbf{k} \cdot \mathbf{p}$ formalizam primenjen na izvođenje jednozonske jednačine efektivnih masa. Zatim je predstavljena $\mathbf{k} \cdot \mathbf{p}$ teorija degenerisanih energetskih nivoa, što je slučaj u valentnoj zoni poluprovodnika sa dijamantskom i sfaleritnom rešetkom. Izveden je Dresselhaus-Kip-Kittelov model stanja u valentnoj zoni u odsustvu spin-orbitne interakcije korišćenjem vremenski nezavisne teorije perturbacija za degenerisana stanja. Potom je uzeta u obzir spin-orbitna interakcija u okviru šestozonskog Latindžer-Konovog modela. Stanja u provodnoj i valentnoj zoni u poluprovodnicima sa širokim energetskim procepom obično se mogu dobro opisati jednozonskom teorijom efektivnih masa i šestozonskim Latindžer-Konovim modelom, respektivno. Međutim, primena ovih modela je ograničena na stanja sa malim vrednostima talasnog vektora elektrona \mathbf{k} , dok se ne mogu primeniti za opis elektronske strukture daleko od Γ tačke. Potreba za dobrim opisom disperzije elektronskih zona daleko od centra Brilloune zone postoji u silicijumu, gde niskoenergetska elektronska stanja imaju veliku vrednost \mathbf{k} . Pogodna teorija za ovaj slučaj je 30-zonski $\mathbf{k} \cdot \mathbf{p}$ model. Ovaj metod omogućuje računanje elektronske strukture u celoj prvoj Brillounoj zoni, stoga se može koristiti kako za direktne, tako i za indirektno poluprovodnike. Zatim je ukratko izložena aproksimacija anvelopnih funkcija, koja predstavlja metod za pri-

menu $\mathbf{k} \cdot \mathbf{p}$ teorije na nanostrukture. Takođe je prikazan postupak uključivanja magnetskog polja i mehaničkog naprezanja u $\mathbf{k} \cdot \mathbf{p}$ formalizam. Primena $\mathbf{k} \cdot \mathbf{p}$ teorije na nanostrukture može da uzrokuje pojavu lažnih rešenja koja su posledica nekompletnog opisa elektronske strukture poluprovodnika. Lažna rešenja se u praksi teško kontrolišu i mogu da predstavljaju značajan problem u proračunu elektronske strukture. Stoga je dat kratak pregled osobina lažnih rešenja, efekata koje izazivaju i mogućih načina za njihovu kontrolu.

Tridesetozonski i šestozonski $\mathbf{k} \cdot \mathbf{p}$ modeli su iskorišćeni za proračun elektronske strukture Si/SiO₂ kvantnih jama. Elektronska i šupljinska stanja su izračunata pomoću 30-zonskog modela, uz aproksimaciju beskonačno duboke kvantne jame. Talasna funkcija je predstavljena u bazu stojićih talasa. Brojna lažna rešenja koja se javljaju u proračunu klasifikovana su u dve grupe: 1) lažna rešenja koja imaju visok doprinos balkovskih stanja sa velikim \mathbf{k} -vektorom (lažna rešenja visokog k) i 2) stanja koja su većinski sačinjena od balkovskih stanja koja pripadaju lažnoj dolini koja se nalazi van prve Brilluene zone (lažna rešenja iz dodatne doline). Predložen je algoritam za uklanjanje lažnih rešenja iz spektra. Pored navedenog, utvrđena je spora konvergencija stanja u valentnoj zoni, koja se ogleda u oscilatornom ponašanju šupljinskih energija u funkciji veličine bazisa. Ovo ponašanje je objašnjeno specifičnim mešanjem zona i nametnutim graničnim uslovima. Pokazano je da pretpostavka o konfiniranju u beskonačno dubokoj kvantnoj jami dovodi do nestabilnosti proračuna. Za konačnu dubinu potencijalne jame, međutim, talasna funkcija eksponencijalno opada u oblasti barijere, što dovodi do stabilnog numeričkog proračuna.

Izračunata je međuzonska optička apsorpcija u Si/SiO₂ kvantnoj jami u funkciji širine jame (W). Analiziran je prelaz strukture sa indirektnim procepom u strukturu sa direktnim procepom sa promenom širine jame. Elektronska stanja su određena pomoću 30-zonskog $\mathbf{k} \cdot \mathbf{p}$ modela, dok su šupljinska stanja izračunata korišćenjem 6-zonskog Latindžer-Konovog modela. Pokazano je da se efektivni zonski procep dobro poklapa sa rezultatima jednozonskog modela, prema kome procep opada sa širinom jame shodno funkciji W^{-2} . Matrični element međuzonskog prelaza za linearno polarizovanu svetlost je oscilatorna funkcija širine jame, što se takođe slaže sa rezultatima jednozonskog modela. Dobijeni rezultati pokazuju da se apsorpcija može optimizovati dobrim izborom širine kvantne jame. Međutim, vrednosti apsorpcije dobijene proračunom su za red veličine

manje nego u kvantnoj jami na bazi direktnih poluprovodnika.

Model elektronskih i šupljinskih stanja u Si/SiO₂ kvantnim jamama je primenjen za računanje elektronske strukture GaAs/Al_{0,3}Ga_{0,7}As kvantne jame. Stanja u provodnoj zoni su izračunata pomoću teorije efektivnih masa i dobijeni rezultati su upoređeni sa rezultatima 30-zonskog modela. Šupljinska stanja su određena pomoću 6-zonske i 30-zonske $\mathbf{k} \cdot \mathbf{p}$ teorije i rezultati dobijeni pomoću ova dva pristupa su međusobno upoređeni. Razlika rezultata dobijenih pomoću jednozonskog i 6-zonskog modela sa jedne strane i 30-zonskog sa druge strane je manja za široke jame. Ovo je posledica činjenice da sva tri modela dobro opisuju zonsku strukturu masivnog GaAs u okolini Γ tačke. Pored toga, stanja izračunata pomoću jednozonskog i 6-zonskog modela manje odstupaju od rezultata 30-zonskog modela ukoliko je ravanski talasni vektor k_{\parallel} manji, kao što se može *a priori* zaključiti. Nađeno je da je slaganje jednozonskog i 30-zonskog modela bolje za niže podzone, koje su dominantno sačinjene od balkovskih stanja sa malom vrednošću talasnog broja k_z . Isto važi i za šupljinska stanja dobijena pomoću 6-zonskog $\mathbf{k} \cdot \mathbf{p}$ modela. Pored toga, slaganje 6-zonskog i 30-zonskog modela je bolje od slaganja jednozonskog i 30-zonskog modela. Navedeni proračun je dopunjen razmatranjem Dresselhausove spin-orbitne interakcije u provodnoj zoni. Upoređeni na 30-zonski i aproksimativni 2-zonski model. Pokazano je da se navedeni modeli kvalitativno dobro slažu. Međutim, dvozonki model daje znatno veće spin-orbitno cepanje nivoa od 30-zonskog modela.

U drugom delu teze razmatrane su prstenolike kvantne tače, koje se proizvode kapljičnom epitaksijom ili Stranski-Krastanov tehnikom. Ove kvantne tačke imaju oblik sličan prstenu, ali sa tankim slojem zaostalim unutar nominalnog otvora. Pretpostavljen je jednostavni geometrijski model kvantne tačke, sačinjen od diska i prstena koji ga okružuje. Kvantna tačka je smeštena u matricu od materijala sa većim energetske procenom. Ovakav model dobro opisuje strukture proizvedene pomoću kapljične epitaksije. Prvo je razmatrana nenapregnuta GaAs/(Al,Ga)As kvantna tačka. Provodna zona je modelovana jednozonskom teorijom efektivnih masa, dok je 4-zonski Latindžer-Konov hamiltonijan korišćen za određivanje stanja u valentnoj zoni. Posmatrano je kako se elektronska struktura prstenolike tačke menja pri promeni dimenzija njenih sastavnih delova, diska i prstena. U navedenom razmatranju varirane su sledeće dimenzije: 1) širina prstena, 2) poluprečnik diska i 3) visina diska. Za tipične dimenzije eksperimentalne strukture

pokazano je da su nosioci naelektrisanja dominantno lokalizovani u prstenu, čak i kada je visina diska 90% visine prstena. Proračuni ukazuju da se topološki fenomeni, kao što je Aharonov-Bohmov efekat, mogu javiti i u slučaju da postoji sloj materijala unutar otvora prstena.

Takođe je razmatran uticaj magnetskog polja na šupljinska stanja u prstenolikim kvantnim tačkama baziranim na nenapregnutim GaAs/(Al,Ga)As i napregnutim (In,Ga)As/GaAs sistemima. Elektronska struktura je određena pomoću 4-zonskog Latindžer-Konovog modela. Aharonov-Bohmove oscilacije elektronskih stanja se manifestuju u promeni ugaonog momenta osnovnog šupljinskog stanja sa porastom magnetskog polja. Oblik ovih oscilacija određen je debljinom diska. Naprezanje u (In,Ga)As/GaAs kvantnim tačkama zavisi od debljine diska i dovodi do lokalizacije teške šupljine unutar diska. Stoga ukrštanja šupljinskih stanja različitih orbitalnih momenata nestaju za mnogo manju debljinu diska nego kod nenapregnutih GaAs/(Al,Ga)As prstenolikih kvantnih tačaka. Pokazano je da Aharonov-Bohmove oscilacije energije osnovnog stanja u valentnoj zoni nestaju pri manjim debljinama diska u poređenju sa sličnim oscilacijama u provodnoj zoni. Razlika u osetljivosti Aharonov-Bohmovih oscilacija na debljinu diska u valentnoj i provodnoj zoni je posledica drugačijih konfinirajućih potencijala i mešanja zona teških i lakih šupljina. To za posledicu ima visoku osetljivost magnetizacije u valentnoj zoni (In,Ga)As/GaAs prstenolike kvantne tačke na debljinu diska. Pored toga, pokazano je da mehaničko naprezanje dovodi do prostorne razdvojenosti elektrona i šupljine, kao u slučaju kvantnih tačaka drugog tipa, što predstavlja pogodan sistem za pojavu ekscitonskog Aharonov-Bohmovog efekta.

Na kraju su navedeni najbitniji rezultati i doprinosi disertacije.

Ključne reči: silicijum, III-V jedinjenja, kvantna jama, kvantna tačka, kvantni prsten, $\mathbf{k} \cdot \mathbf{p}$ teorija, višezonski, 30-zonski hamiltonijan, optička apsorpcija, Aharonov-Bohmov efekat

Naučna oblast: Elektrotehnika i računarstvo

Uža Naučna oblast: Nanoelektronika i fotonika

UDC broj: 621.3

Contents

1	Introduction	1
1.1	Silicon nanostructures	3
1.2	Fabrication techniques	6
1.2.1	Fabrication of Si/SiO₂ quantum wells	7
1.2.1.1	Sputtering	7
1.2.1.2	Plasma enhanced chemical vapour deposition (PECVD)	9
1.2.1.3	Molecular beam epitaxy (MBE)	10
1.2.1.4	Thermal/chemical processing - silicon-on-insulator . .	12
1.2.2	Fabrication of GaAs/(Al,Ga)As quantum wells	14
1.2.3	Fabrication of ringlike quantum dots	16
1.2.3.1	Droplet epitaxy	16
1.2.3.2	Fabrication of strained quantum rings	18
1.3	Bulk properties of Si, GaAs, InAs, and AlAs	20
1.3.1	Silicon	21
1.3.2	III-V semiconductors	22
1.4	Overview of the thesis	25
2	The multiband $\mathbf{k} \cdot \mathbf{p}$ theory	27
2.1	The particle in a periodic potential	29
2.2	The single-band effective-mass model	31
2.3	The valence-band electronic structure	33
2.3.1	The Dresselhaus-Kip-Kittel Hamiltonian	34
2.3.2	The six-band Luttinger-Kohn model	36
2.4	The 30-band $\mathbf{k} \cdot \mathbf{p}$ Hamiltonian	41

2.5	The envelope function approximation	45
2.6	Nanostructures in a magnetic field	48
2.7	Modelling strained quantum dots	49
2.8	Spurious solutions in the MEFA	51
3	The electronic structure of silicon quantum wells	55
3.1	The bulk band structure of silicon	56
3.2	The quantum well states	57
3.3	The origin of spurious states	58
3.4	The spurious solutions removal	61
3.5	The hole states	65
3.6	The case of the finite band offset	66
4	Interband optical transitions in silicon quantum wells	70
4.1	Theoretical model	70
4.2	Interband transition energies	71
4.3	Interband transition matrix elements and interband absorption	75
5	The 30-band model of the GaAs/(Al,Ga)As quantum wells	79
5.1	The electron states	81
5.1.1	The subband dispersion relations	81
5.1.2	The Dresselhaus spin-orbit splitting	85
5.2	The hole states	88
6	Electron and hole states in ringlike quantum dots grown by droplet epitaxy	93
6.1	The theoretical model	94
6.2	Numerical results and discussion	97
6.2.1	$R_2 = const, R_1$ varies	98
6.2.2	$W = const, R_1$ varies	99
6.2.3	$h = const, t$ varies	100
7	Ringlike quantum dots in a magnetic field	105
7.1	Theoretical models	107

7.2	Numerical results and discussion	109
7.2.1	The effective potentials	110
7.2.2	The conduction-band states	111
7.2.3	The valence-band states	114
7.2.4	Comparisons between the conduction and valence band states . .	116
7.2.5	Influence of the geometry	119
8	Conclusion	123
	References	127
A	Si, GaAs and AlAs band parameters	149
	Biography	151
	List of Publications	153

Chapter 1

Introduction

Nanotechnology is a multidisciplinary field that encompasses fabrication, engineering, and application of nanoscaled physical systems which are called *nanostuctures*. During the last few decades downscaling of electronic devices has been governed by the Moore's law [1], which led to the development of *nanoelectronics*. It is the subfield of *nanoscience* which deals with electrical, optical, and mechanical properties of nanostructures. Since nanostructures have dimensions comparable to the de Broglie wavelength of the electron, their properties relevant for nanoelectronic applications are described by quantum mechanics, which is in contrast with classical microelectronics. Nanostructures can be formed out of various materials, either metals, dielectrics, or semiconductors. Graphene and other two-dimensional materials have been admittedly in focus of experimental and theoretical research during the last decade. Yet, the interest in *semiconductor nanostructures*, which are composed of semiconductors, has not ceased with the graphene discovery. In fact, they remain to be important for the modern technology, and a few of them will be the topic of the present thesis.

Various fabrication techniques have been employed to grow semiconductor nanostructures, and are known to cause the electron confinement along certain directions. Depending on number of directions along which the electron motion is confined, semiconductor nanostructures are generally classified as *quantum wells*, *quantum wires (nanowires)*, and *quantum dots (nanodots)*. In quantum wells the electrons and holes are confined along a single direction, whereas their motion remains free (in terms of the effective mass theory [2]) along the other two directions. Quantum wires are semiconductor nanostructures

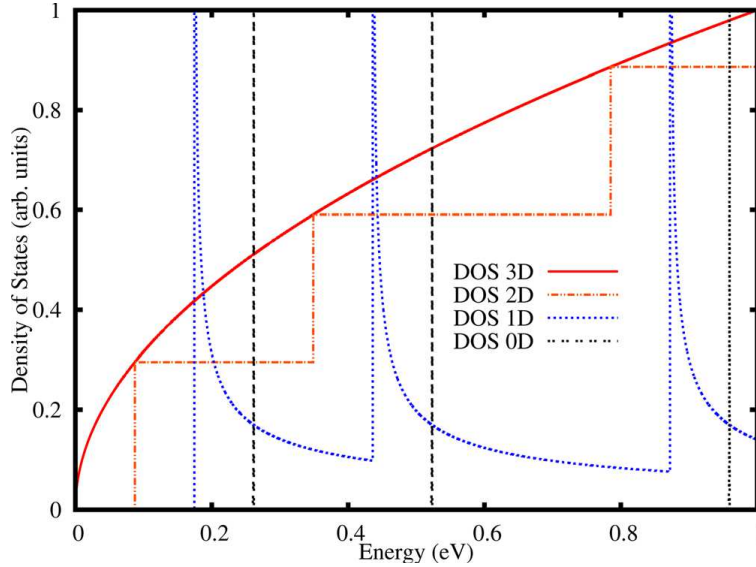


Figure 1.1: Density of states as function of energy in bulk semiconductor (the 3D case), semiconductor quantum well (the 2D case), quantum wire (the 1D case), and quantum dot (the 0D case) (from Ref. [3]).

where the charge carriers are confined in two spatial directions. In quantum dots there exists the electron and hole confinement along all three spatial directions.

Quantum confinement is most vividly illustrated in the dependence of the density of states ρ on energy E , as Fig. 1.1 displays. In a bulk semiconductor, ρ is proportional to \sqrt{E} (where electron energy is measured from the band extremum), and in quantum wells it consists of sharp steps, which take place at the subband bottoms. In quantum wires, ρ is proportional to $1/\sqrt{E}$, and in quantum dots it is expressed as a sum of the Dirac functions which take place at bound states.

Many semiconductors have been shown to form nanostructures: the group IV elements, III-V compounds, II-VI compounds, and alloys of these compounds. Among the elemental semiconductors, Si has been the most frequent choice, whereas GaAs has unprecedented use among all III-V compounds. Those materials distinguish themselves from the others by relative ease of fabrication their bulk samples. Thus, they are convenient substrates, but could also be combined with other semiconductors to make nanostructures. Furthermore, their properties are well investigated, such that numerous electronic and photonic devices have been fabricated out of semiconductors. And both materials have paramount importance for applications, which are quite numerous and diversified

[4–8].

In this thesis, we analyze Si/SiO₂ and GaAs/(Al,Ga)As quantum wells [2, 9–11]. Also, we consider ringlike GaAs/AlGaAs and InGaAs/GaAs quantum dots, where the Aharonov-Bohm (AB) effect [12–16] was found. Nonetheless, a few recent achievements in silicon nanostructures and silicon-based materials will be briefly corroborated.

1.1 Silicon nanostructures

Silicon remains to be the most important semiconductor, and is used to build numerous electronic [17, 18] and photonic devices [4, 5, 8, 19–24]. And the investments in developing the silicon technology have been enormous since the invention of the bipolar transistor. The main use of silicon remains in electronics, yet to establish that the Moore's law validity will be extended to the foreseeable future, it has been recently combined with other materials, for example germanium. And silicon has numerous and diversified applications in photonics. The silicon band gap equals 1.17 eV [25], which is in the near infrared region. Therefore, it is a convenient choice for photonic detectors [26, 27], solar cells [5, 19, 22, 23], light-emitting devices [8, 20, 28, 29] etc. Also, silicon is a convenient substrate for integrating lasers based on III-V semiconductors with electronics [30, 31]. Various combinations of silicon with other materials, such as Si/SiGe and Si/SiO₂ heterojunctions, are found to form quantum wells [5, 32–34]. Also, freestanding Si nanowires, core-shell Si/Ge nanowires [18, 35, 36], Si/SiGe, Si/SiO₂ and dopant-based quantum dots [37–39], have all been produced and their properties have been examined.

Quite recently, samples of the 2D silicon, called *silicene* has been produced, and are found to exhibit quite exotic properties, which differ from 3D silicon samples [41–44]. The possibility of formation the 2D silicon layers has been investigated since mid-nineties [45, 46]. Yet, it took more than a decade before samples became available in laboratory [40, 41, 47]. Silicene is usually grown by super-heating silicon and evaporating its atoms onto the silver substrate [40], which leads to the layers stable when exposed to air [48].

Silicene has hexagonal honeycomb lattice, similar to graphene (see Fig. 1.2), and exhibits ordered ripples [49]. The interlayer coupling in silicene is found to be significantly stronger than in graphene [48]. However, it has similar electronic structure to graphene,

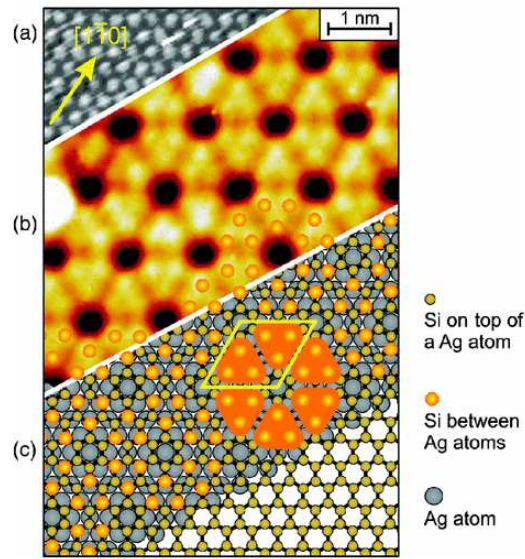


Figure 1.2: The STM images of: (a) the initially clean surface of Ag(111) and (b) the surface after covering by the silicene sheet. (c) The silicene (orange balls) electronic structure is computed by using the ball-and-stick model, shown in the bottom right corner (from Ref. [40]).

with the minimum of the conduction band at the K point and linear dispersion of the energy bands close to this point [50]. Furthermore, the silicene band gap can be tuned by external electric field and doping [51]. Therefore, it has been considered to be a promising candidate for implementation of the tunnel field-effect transistor (TFET) concept [51], which is expected to be the leading integrated-circuit technology in future. Moreover, the hydrogenization of silicene is an exothermic process, which makes silicene a good candidate for hydrogen storage [52].

In addition to formation of silicene, the silicon technology has also advanced in photonics. One such application is laser diode based on an ultrathin silicon layer embedded within layers of SiO_2 , which is demonstrated in Ref. [29], and whose structure is displayed in Fig. 1.3. Here, the resonant cavity is made of the Si_3N_4 grating embedded in SiO_2 (see inset in Fig. 1.3(b)). Freestanding silicon layers are placed on the top of the $1.3 \mu\text{m}$ thick suspended membrane made of SiO_2 . The Si quantum well had the (100) orientation and was 3 nm wide, therefore the electron states are quantized, and moreover stimulated emission was experimentally verified. It was achieved by current injection at the room temperature, and the peaks of the emission spectra correspond to the interband

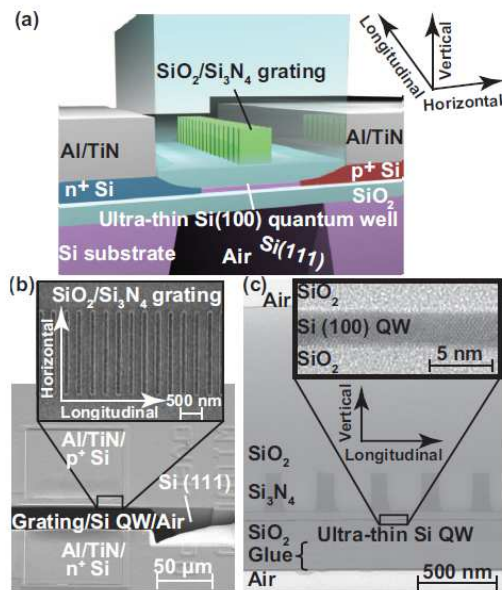


Figure 1.3: The structure of the Si quantum-well laser diode. (a) A schematic view of the device structure. (b) The SEM image after focused ion beam etching. Inset shows the $\text{SiO}_2/\text{Si}_3\text{N}_4$ grating. (c) The TEM images after completed processing, with inset showing crystalline Si quantum well having the (100) orientation (from Ref. [29]).

transitions in the infrared wavelength range. The silicon quantum-well laser diodes are expected to be better integrated with CMOS electronics than lasers based on III-V compounds.

Another potential application of Si/SiO_x layers in photonics is for fabrication of the third generation solar cells. The first generation of solar cells was based on bulk materials, the second generation used a few micrometer thick layers, whereas the third generation is based on nanostructures, such as quantum wells, quantum wires, nanotubes etc. Nanostructures are deliberately employed to increase quantum efficiency above the Shockley-Queisser limit [54]. Single and multiple silicon-based quantum wells have been extensively studied for this purpose [5, 22, 23, 53]. Thinning of the silicon layer leads to increase of the bandgap, thus visible light becomes more efficiently absorbed than in bulk samples. An example of the multilayer Si/SiO_x system is shown in Fig. 1.4 [53]. Periodic Si/SiO_x structures generally have low conductivity due to high barrier in the Si/SiO_x heterojunction. It could be a drawback for application in solar cells, which should exhibit high conductivity. However, when the sample is annealed, the layer of crystalline silicon intrudes the SiO_x layers, as Fig. 1.4 shows. As a consequence, a dense network of

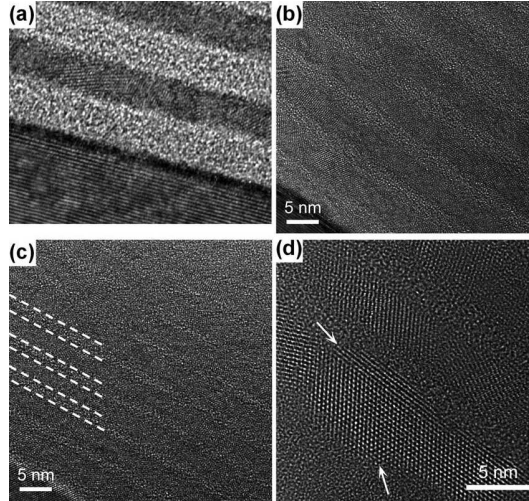


Figure 1.4: The TEM images of ten-period piles of annealed stoichiometric Si/SiO_x samples for the ratio between the Si and SiO_x thicknesses: (a) 3 nm/4 nm, (b) 4.5 nm/2.5 nm, (c) 3.2 nm/1.8 nm, and (d) same as (b) but with reduced spot size. The micrograph demonstrates facets (indicated by arrows) of the crystalline Si layer intruding the amorphous SiO_x barrier layers (from Ref. [53]).

conducting paths is created, which increases the sample conductivity [53]. Also, varying the stoichiometry x affects both the bandgap value and the conductivity, which are crucial parameters of the solar cells performance.

1.2 Fabrication techniques

There are various techniques to fabricate semiconductor nanostructures. Some of them could be employed to grow layers of quite general composition, such as molecular beam epitaxy. But some processes have been recently employed to grow nanostructures of quite specific shape and composition, such as *sputtering*, *plasma enhanced chemical vapor deposition*, and *ion cut process*. They are all used to form layers of silicon embedded within dielectric layers of SiO₂. For quantum dots, epitaxy of strained nanostructures ((In,Ga)As/GaAs, for example) in the *Stranski-Krastanov* (SK) mode has been known for some time, but recently *droplet epitaxy* (DE) has been developed to grow the GaAs/(Al,Ga)As nanostructures, which are made of the lattice matched semiconductors.

In the following text, we present the techniques which are employed to grow the nanostructures analyzed in this thesis: the Si/SiO₂ quantum wells, the GaAs/(Al,Ga)As

quantum wells, the unstrained GaAs/(Al,Ga)As quantum dots, and the strained (In,Ga)As/GaAs quantum dots.

1.2.1 Fabrication of Si/SiO₂ quantum wells

Here, we discuss several planar processes which are employed to form layered structures based on the Si/SiO₂ heterojunction. Therefore, all the methods presented below could be employed to produce layers whose widths are comparable to the Bohr radius, when effects of quantum confinement can be experimentally observed [28, 29, 55–58]. The presented techniques usually produce layers which have amorphous structures but could be transformed into the crystalline state by subsequent annealing. The drawback of the annealing is that the interface between Si and SiO₂ becomes disturbed by the diffusion of oxygen atoms into the silicon layer [59]. Yet, if the annealing is properly controlled, the defect concentration can be kept low [55, 60–62].

1.2.1.1 Sputtering

The essential feature of sputtering is that it delivers the material to be grown at the substrate from the other sample, called the target. To remove atoms from the target, it is bombarded by high-energy ions, usually those of argon (Ar⁺). The removed atoms create a vapor phase, and are subsequently deposited onto the substrate. The scheme of a typical sputtering process is shown in Fig. 1.5. The target material is biased negative with respect to the substrate, with typical voltage of 2 kV.

The operation starts with the gas evacuation from the chamber, and continues with pumping the buffering gas (argon) into the system, which results into a low (1-10 Pa) pressure in the chamber [3]. The strong electric field brings about the ionization of the Ar atoms, which become attracted by the negatively charged target material. A magnetron field is introduced to increase ionisation efficiency and to trap the ions near the target surface.

To fabricate the Si/SiO₂ quantum well, the first step is the formation of the Si layer from the Si target. It then proceeds with the forming of the SiO₂ layer, which could be created by thermal oxidation of the layer of the sputtered silicon [63]. The alternative technique is *co-sputtering*, where Si and O are deposited from different target materials

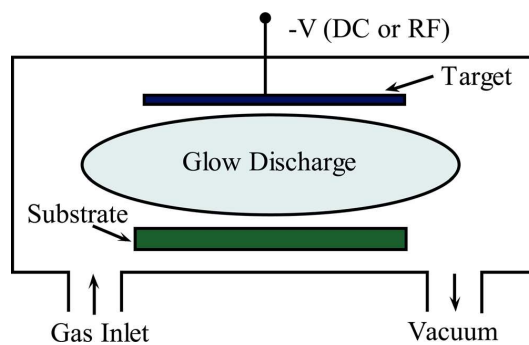


Figure 1.5: A scheme of the sputtering apparatus (from Ref. [3]).

placed in the chamber [64]. In this technique, the silicon target is bombarded to extract the Si atoms, and the SiO_2 target is bombarded to extract the atoms of oxygen [65]. The Si and O atoms chemically react in the vapor phase outside the substrate, and form the layer of SiO_x onto the previous Si layer. The stoichiometry and the structure of the SiO_x layer depends on the parameters of the sputtering process: kinetic energy of the sputtered particles, types and fluxes of the particles, growth temperature, pressure, and RF power [66]. Those parameters can be adjusted to realize the stoichiometry of SiO_2 . The Si and SiO_x layers are amorphous, thus annealing is required to convert the amorphous silicon layer to the crystalline state [67]. The annealing is performed at typical temperature of 1100°C .

Typical dimensions of the quantum wells fabricated by sputtering range from 2 nm to 30 nm [68]. However, their quality could not be good for photonic applications. But improvements of the process are expected to occur in the future, with the aim to improve reproducibility of such formed quantum wells. Even though they have crystalline form, their photoluminescence (PL) spectra exhibit two peaks, at wavelengths 600 nm and 790 nm, which are found to be independent of well width [60, 67, 69]. Hence, it is concluded that they arise from defects. As a matter of fact, a substantial diffusion of oxygen into the silicon layers is found to cause them [63]. And as a consequence, the Si/ SiO_2 wells fabricated by sputtering do not exhibit high luminous efficiency, which limits their applications in photonics.

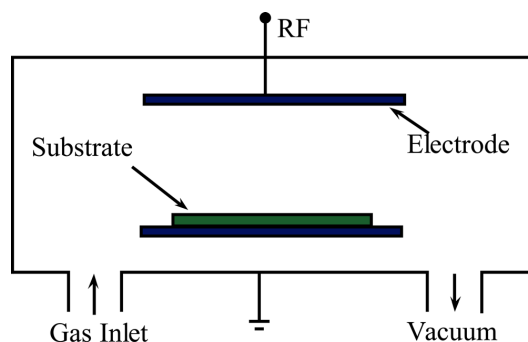


Figure 1.6: A scheme of the PECVD apparatus (from Ref. [3]).

1.2.1.2 Plasma enhanced chemical vapour deposition (PECVD)

Plasma enhanced chemical vapour deposition (PECVD) is a modified technique of chemical vapour deposition (CVD), where the chemical reactions, which occur in the vapor phase, are catalyzed by creating a plasma of the reacting gases. A scheme of the typical PECVD equipment is shown in Fig. 1.6. Here, the substrate is placed between two electrodes, with one of them being the wall of the reaction chamber and is grounded, whereas the other electrode is connected to a RF or a DC source [66]. The deposition starts with the introduction of the gas mixture in the reaction chamber, and continues by the induction of the plasma under the RF field. The reactions in the ionized gas are more pronounced than in the standard CVD process which uses the neutral precursors [3].

The silicon deposition occurs due to the thermal decomposition of silane (SiH_4), which is introduced in the chamber in the gas phase. Silane is directed over the hot substrate, and becomes decomposed by the heat originating from the substrate, which is a process described by $\text{SiH}_4(\text{g}) \rightarrow \text{Si}(\text{s}) + 2\text{H}_2(\text{g})$. The silicon atoms are then adsorbed to the substrate surface, which results in the formation of the silicon layer. To deposit films of SiO_x , the mixture contains silane and helium with added nitrous oxide (N_2O) or oxygen.

The PECVD process can be used to produce rather thin quantum wells. For example, in Ref. [70] it was demonstrated that the quantum well width could be in range from 2 nm to 5 nm. High deposition rates, which are in the range 1-10 nm/s, are achieved by the PECVD. The film quality depends on: composition of the gas mixture, pressure, substrate temperature, flow rate of the gas, electron density in the plasma, discharge energy,

RF power etc. For example, in order to minimize defect concentration in the film, the deposition rate has to be compatible with the relaxation rate of the atoms at the surface [71]. Also, high deposition rates could lead to non-uniform layer thickness [72].

The fabricated structures suffer from low reproducibility [71]. Nonetheless, the standard CVD process used to grow the Si/SiO₂ quantum wells exhibit even lower performance, since it usually results in isolated islands of the deposited material [73]. Also, the fabricated quantum wells have amorphous structure, with high concentration of unstable Si-O-Si bonds, which break at the interface and form the -OH defects in the silicon-oxide layer. The annealing should then be applied to form quantum wells with crystalline structure. And, the interface mixing which occurs due to the annealing is smaller than in quantum wells fabricated by the co-sputtering technique [62, 74].

1.2.1.3 Molecular beam epitaxy (MBE)

Molecular beam epitaxy (MBE) is a process which allows straightforward fabrication of high quality epitaxial layers which could be even few monolayers thick. A scheme of the typical MBE apparatus is shown in Fig. 1.7. It consists of the growth chamber kept under extremely low pressure (of about 10^{-7} Pa). The substrate is positioned in the chamber, and is heated and rotated to facilitate growth of layers of uniform thickness. The sources of materials which form the epitaxial layers are located in the effusion cells. For example, to grow a silicon layer, the sources of silane or disilane (Si₂H₆) are used. The material which is evaporated or sublimed from the effusion cell is collimated into the beam and directed toward the heated substrate. Because of ultra-high vacuum in the chamber, atoms or molecules move ballistically from the effusion cell to the substrate, thus a molecular flow is established.

The MBE growth of epitaxial layers depends on the number of dangling bonds at the substrate surface. Depending on the growth conditions, three morphologies could occur: (1) Frank-van der Merwe (FM), where growth occurs layer by layer, 2) Volmer-Weber (VM), where 3D islands are formed leaving a part of the substrate unexposed [76], and 3) Stranski-Krastanov, where 3D islands are formed on the thin wetting layer [77–79]. The FM and VM growth could be realized for small difference between the lattice constants of the substrate and the deposited material. When the lattice mismatch is larger, the

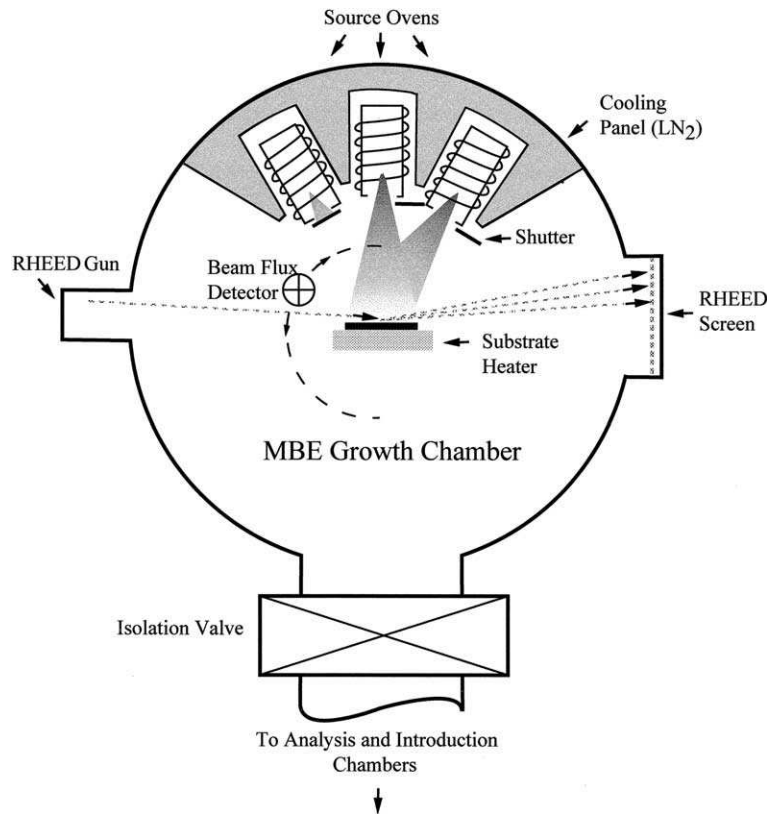


Figure 1.7: A schematic view of the equipment for molecular beam epitaxy (from Ref. [75]).

energy due to mechanical strain becomes larger than the free energy of the interface, and consequently the growth occurs in the SK mode [80]. The layer morphology depends on type of the substrate or the pre-layer, growth temperature, deposition rate, etc. [3]. The MBE equipment contains a probe for reflection high-energy electron diffraction (RHEED) (see Fig. 1.7), which allows in-situ monitoring and characterization of the growth process. The RHEED provides various informations about the crystal symmetry, imperfections which may appear during the growth, and indicate if the growth has 2D or 3D character [81, 82].

Quantum wells are generally grown in the Frank-van der Merwe mode. To form a layered structure, complete wetting of the substrate should occur [83]. When this condition is not satisfied, layers thinner than the critical thickness will be stable, whereas if the material supply becomes exceedingly increasing, islands are formed instead of films [80, 83]. To form the layers of SiO_2 , the silicon layer is deposited first, and then exposed to oxygen [84]. Similar to sputtering and PECVD, silicon layers produced by the MBE

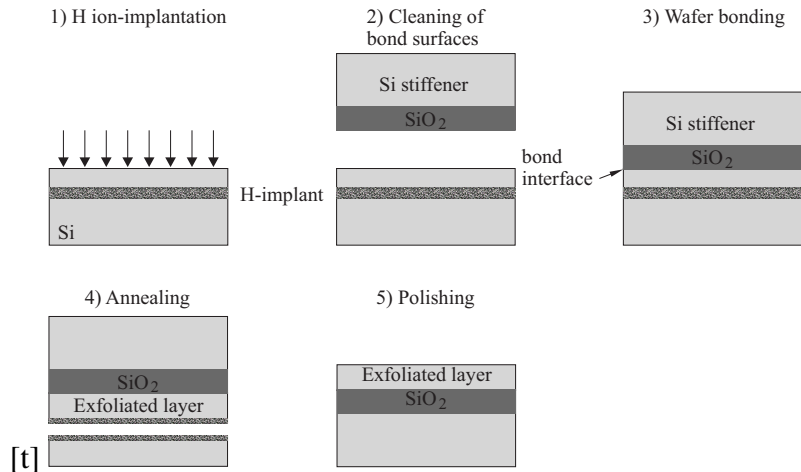


Figure 1.8: An illustration of the processing steps of the ion-cut process used to produce SOI structures (after Ref. [85]).

are amorphous, therefore they are annealed after the growth is finished. Yet, contrary to sputtering and PECVD, the layers fabricated by MBE are highly reproducible.

The PL experiments show that the Si/SiO₂ quantum wells grown by MBE are of similar quality to quantum wells formed by sputtering [84]. Similar to the layers produced by sputtering, during the MBE growth, Si and O atoms interdiffuse in the vicinity of the interface, which results in the formation of an interfacial layer where the holes are confined [84]. Also, the layers of Si and SiO₂ do not completely crystallize [28, 86], which is explained by a large interfacial stress even at temperatures as high as 1100 °C [84, 87].

MBE is a powerful technique for production of various quantum well structures, therefore, quantum wells and superlattices made of either silicon or III-V semiconductors can be efficiently fabricated by this technique. Furthermore, the MBE process is controllable, flexible, clean, and as mentioned, does not suffer from low reproducibility, dissimilar to the other processes discussed here.

1.2.1.4 Thermal/chemical processing - silicon-on-insulator

The Si/SiO₂ quantum wells can also be fabricated by the technique of combined thermal and chemical treatment of silicon layers on insulator (SOI). The SOI structure could be fabricated using the *ion cut process* (ICP) [85], whose steps are shown in Fig. 1.8. It consists of the following steps: 1) implantation of the hydrogen ions into the Si wafer, 2) cleaning of the surfaces which are to be bonded, 3) bonding of the implanted wafer to the

other substrate which is oxidized, and 4) annealing of the bonded wafer and subsequent exfoliation. This process is found to produce a clean interface between the crystalline silicon and the amorphous silicon-dioxide.

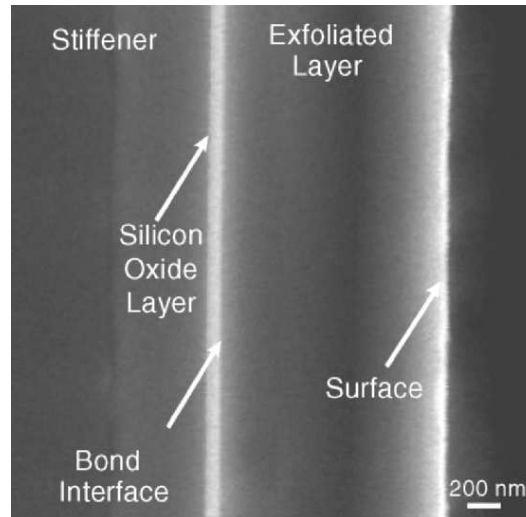


Figure 1.9: The SEM image of the silicon surface layer after bonding and ion-cutting (from Ref. [85]).

With more details, the process starts with the hydrogen implantation into the monocrystalline silicon wafer to a depth which depends on the width of the future quantum well (see Fig. 1.8(a)). The wafer surface is then cleaned from the contamination which arises during the H-ion implantation. The other wafer, called the stiffener, is capped by silicon-dioxide, and the two wafers are bonded (see Figs. 1.8(b) and (c)). The formed structure is then heated at 200°C for a few hours to strengthen the bonds between the wafers. After this step the bonded wafers are annealed at about 400°C, which gives rise to the bubbles of the H₂ gas. The pressure inside the bubbles could be high, up to 50 kbar [85]. At a certain moment of the processing, the bubbles create a propagating crack throughout the sample, which brings about a separation of the sample into two parts (see Fig. 1.8(d)). After the annealing, the surface of the sample is polished to remove the damage that arises from the cracking. The SEM image of the structure at this stage is shown in Fig. 1.9. In the final stage of the fabrication, the layer of SiO₂ is formed by the thermal oxidation of the silicon surface. This SiO₂ layer has the monocrystalline quality, the uniform width, and contains low concentration of the defects. Therefore, its quality is better than of layers produced by sputtering, PECVD and MBE.

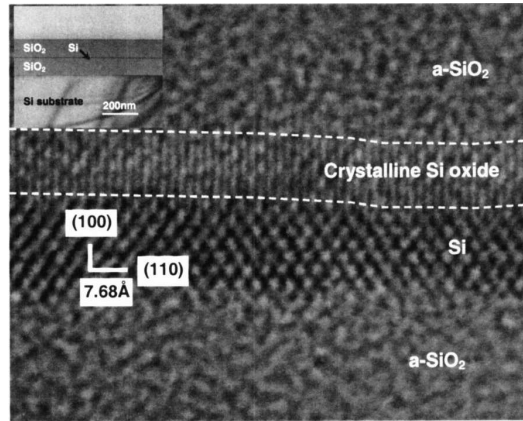


Figure 1.10: The TEM image of the Si/SiO₂ quantum well fabricated by the SIMOX process (from Ref. [61]).

In addition to the ion-cut process, monocrystalline layers of silicon can be fabricated by the SIMOX technique (separation by implantation of oxygen) [55–57, 88]. In this process, the oxygen atoms are implanted in the Si wafer and the sample is subsequently annealed, which lasts for several days. This process results in the formation of a buried silicon-dioxide layer. The second layer of SiO₂ is formed on the sample surface by the annealing in dry oxygen. The quantum wells fabricated by the SIMOX technique are found to have not as good quality as the quantum wells made by the ion-cut technique [85]. However, a modification of the SIMOX process called the epitaxial layer transfer (ELTRAN) [89] was found to improve the formed SOI layers [61]. The TEM image of the Si/SiO₂ quantum well produced by SIMOX is shown in Fig. 1.10.

1.2.2 Fabrication of GaAs/(Al,Ga)As quantum wells

The GaAs/(Al,Ga)As heterojunction is the most studied system of all the combinations of III-V semiconductors which form nanostructures. The GaAs/(Al,Ga)As nanostructures have been used to build numerous electronic and photonic devices, such as single-electron transistors [90], quantum-well lasers [91, 92], photodetectors [93, 94], quantum-cascade lasers [11, 95], photovoltaic cells [96] etc. GaAs and (Al,Ga)As have very similar lattice constants, and practically constitute a lattice matched system. Therefore, these structures are unstrained, and their layers can have almost arbitrary thicknesses. They are usually made by MBE [75, 97–100] or metalorganic chemical vapor deposition (MOCVD) [101].

Use of MBE is preferable for producing high quality layers, thus the details of the MBE fabrication of the GaAs/(Al,Ga)As quantum wells will be briefly explained [102].

In order to fabricate the GaAs/(Al,Ga)As quantum wells, the effusion cells should be filled with the elemental Ga, Al, and As. The growth rate could vary depending on the temperature and pressure variation in the chamber. For example, to grow the GaAs layer with the rate of 1000 nm/h, the wafer should be kept at the temperature of 580°C, the effective pressure of the gallium beam should be 7×10^{-5} Pa, the temperature in the Ga effusion cell 1185°C, the pressure of the arsenic beam 7×10^{-4} Pa, and the temperature in the arsenic effusion cell should be 310°C [102]. The beams originating from the effusion cells should be properly tuned to grow the $\text{Al}_x\text{Ga}_{1-x}\text{As}$ layers with a specific mole fraction x . The abrupt variation of the composition in the quantum well is achieved by opening and closing of the shutters in front of the effusion-cells.

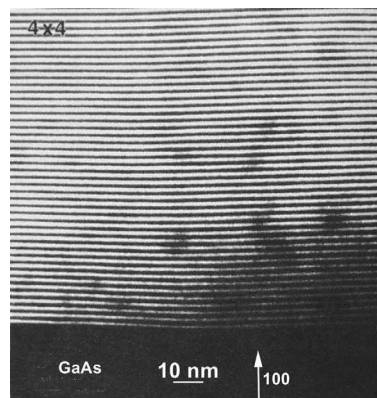


Figure 1.11: The TEM image of the GaAs/AlAs superlattice fabricated by MBE (from Ref. [75]).

As discussed in Sec. 1.2.1.3, the MBE is equipped with the RHEED system, which allows an *in situ* characterization, and is used to control interactions of the particles before forming the uniform layer. In the RHEED, the electron beam is projected onto the growing surface, wherefrom it diffracts and produces a pattern on the phosphorescent screen. The RHEED is able to show how the composition varies beneath the sample surface to a depth of a few layers [75, 82]. In GaAs/(Al,Ga)As quantum wells it is found to depend on temperature in the As effusion cell and the effective pressure of the As beam. As a matter of fact, the conditions can be established to realize a layer of say Ga atoms at the substrate surface. The As atoms are then attached to the dangling bonds at the sample

surface, and the GaAs monolayer is formed. By using the RHEED, the temperature in the effusion cell and the beam effective pressure could be adjusted to obtain a specific structure. The accumulation rate of Ga and As atoms at the surface is different for the same beam effective pressure. The As atoms are found to vigorously leave the hot surface, therefore they should be kept under an order of magnitude larger flux than the atoms in the Ga beam [103]. A cross section of the GaAs/(Al,Ga)As superlattice fabricated by alternating the molecular beams is shown in Fig. 1.11 [75].

1.2.3 Fabrication of ringlike quantum dots

The second part of the thesis deals with ringlike quantum dots (RQDs), which are also referred to as *quantum rings* or *nanorings*. A perfect ring has a full opening, and therefore has the doubly-connected topology, whose consequence is emergence of the Aharonov-Bohm effect, orbital magnetism, and persistent currents [12, 13, 104–108]. The mentioned effects are employed to realize superconducting quantum interference devices (SQUID's) [109, 110], high-density magnetic memories [111], terahertz photodetectors [112], and lasers [113]. The ringlike quantum dots are usually formed by the following two methods:

1. droplet epitaxy, which is used for to fabricate GaAs/(Al,Ga)As quantum dots;
2. Stranski-Krastanov mode of epitaxial growth which leads to formation of strained ringlike quantum dots.

1.2.3.1 Droplet epitaxy

The technique of droplet epitaxy employs the MBE equipment to self-assemble the droplets of the group III material, such as gallium. The droplets then crystallize under supply of the group V material, which is the mechanism based on the Volmer-Weber mode of epitaxial growth [3, 80]. During the last decade this method has been used to fabricate various nanostructures, such as quantum dots, quantum-dot molecules, quantum rings, and concentric quantum rings [114–117].

Here, we explain the process of fabrication of the GaAs/(Al,Ga)As ringlike quantum dots by the DE. Different procedures have been proposed, differing in details only. Hence,

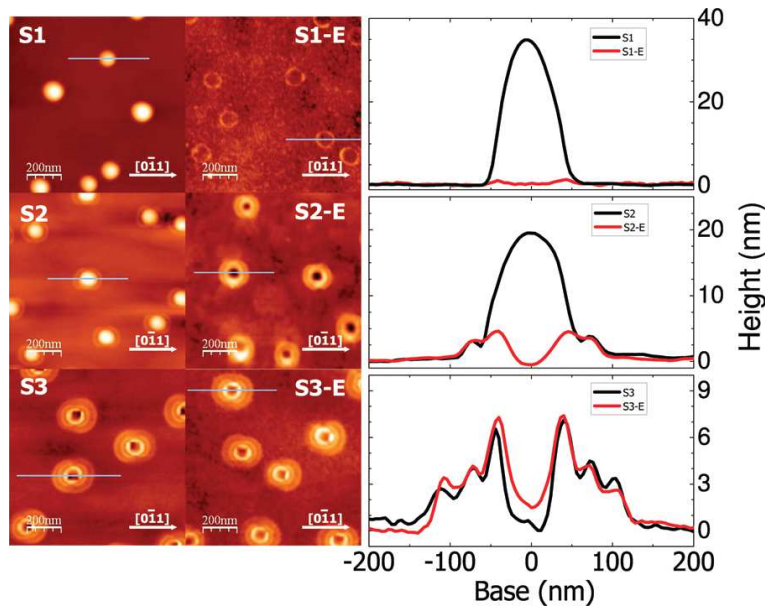


Figure 1.12: The AFM images of the different GaAs/AlGaAs samples grown by DE. (Left panel) The unetched samples denoted by S1, S2, and S3. (Central panel) The etched samples S1-E, S2-E and S3-E. (Right panel) Variation of the dot height along the directions shown by the horizontal lines in the left and right panels (from Ref. [114]).

the procedure described below can be regarded to be typical for the DE formation of quantum dots [114]. The standard MBE equipment is used to grow the 750 nm thick layer of the semi-insulating GaAs. The 200 nm thick $\text{Al}_{0.3}\text{Ga}_{0.7}\text{As}$ layer is then grown at the temperature of 580°C . The temperature is subsequently reduced to 350°C and the shutter of the effusion cell containing arsenic is closed. At 350°C the surface of the sample becomes rich in As [118]. The sample is then supplied with the Ga atoms until the Ga droplets are formed, and the temperature is further reduced to 250°C . The sample is afterward irradiated by the As beam for 20 seconds. Finally, the temperature is increased to 300°C , without changing the flux of the As beam for 20 minutes. The result of this process is the crystallization of Ga droplets and the formation of the ringlike quantum dots. The AFM images of the sample surface after each of the mentioned processing steps are shown in Fig. 1.12 (S1, S2 and S3 image). After the third step the formed quantum dots are almost perfectly axially symmetric [114]. In order to remove the Ga atoms which have not reacted with the As atoms from the substrate surface, the islands are etched, as shown in the right panel of Fig. 1.12 (images denoted by S1-E, S2-E, and S3-E).

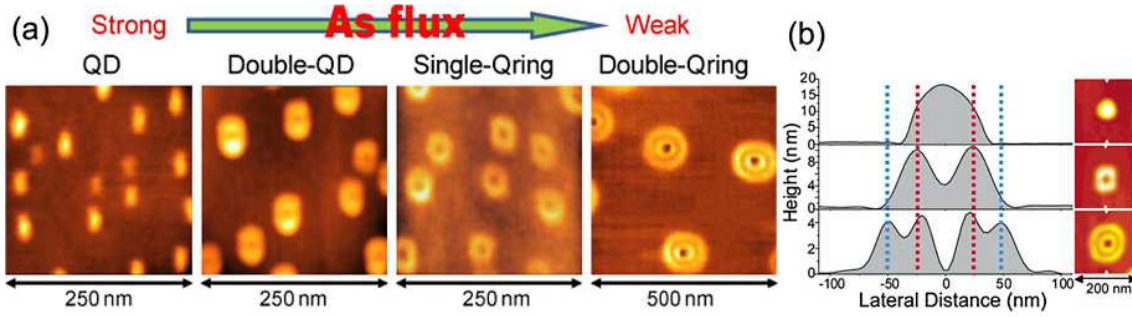


Figure 1.13: (a) The AFM images of GaAs/(Al,Ga)As quantum dots fabricated by the DE. The As flux decreases from left to right. (b) The height variation with the lateral distance in a few vertical cross sections (from Ref. [80]).

The cross sections of the fabricated nanostructures in different phases of their formation are shown in right panel of Fig. 1.12. The completed islands have shapes similar to rings, yet their topology is not doubly connected, since a layer of GaAs remains inside the (nominal) ring opening. Also, notice that even after the second step of the processing (the short exposure to the As beam) ringlike dots are obtained, which would not be known if the samples were not etched. In the final stage, the ensemble of the quantum dots is covered by the $\text{Al}_{0.3}\text{Ga}_{0.7}\text{As}$ layer [114].

It was found that the exact shape of the formed quantum dots depends on the flux of the As atoms, as illustrated in Fig. 1.13. When the As beam equivalent pressure (BEP) is high, such as 2.7×10^{-2} Pa, the singly connected GaAs quantum dots are produced [117, 119]. Decrease of the As BEP leads to the formation of the anisotropic GaAs quantum dots [80, 120]. When the As BEP is further reduced (to 1.3×10^{-3} Pa), the islands take ringlike shape [80, 120]. If the As BEP is even further reduced (to 1.3×10^{-4} Pa), the ringlike dots are found to have shapes similar to concentric rings [116].

1.2.3.2 Fabrication of strained quantum rings

The nanometer-sized strained quantum rings have been fabricated by either the Stranski-Krastanov growth sequence [77, 79, 121] or using lithography [13]. The SK growth starts with the formation of a 2D layer on a lattice-mismatched substrate, which accumulates the strain energy and is called the *wetting layer*. When the thickness of this layer reaches the critical value, the system relaxes by the transformation of the 2D layer into 3D islands.

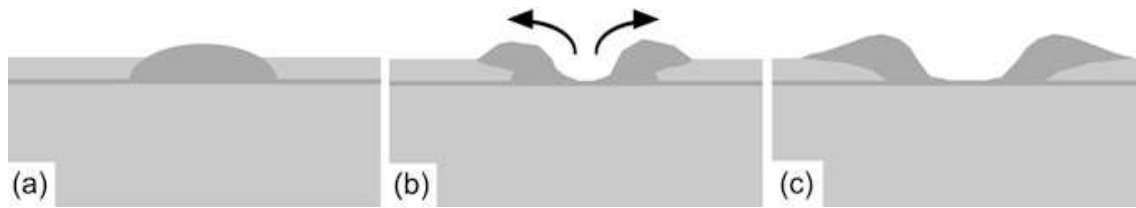


Figure 1.14: A schematic view of the InAs quantum dot transformation to an InGaAs quantum ring due to annealing (from Ref. [80]).

The critical thickness depends on the lattice mismatch between the substrate and the epitaxial layer. The quantum rings are produced from the 3D islands by partially covering the sample with a thin capping layer. The sample is annealed at high temperature for a short period of time, which leads to a relocation of the material close to the dot center to the quantum dot periphery [121, 122]. This process is known as the *dewetting*.

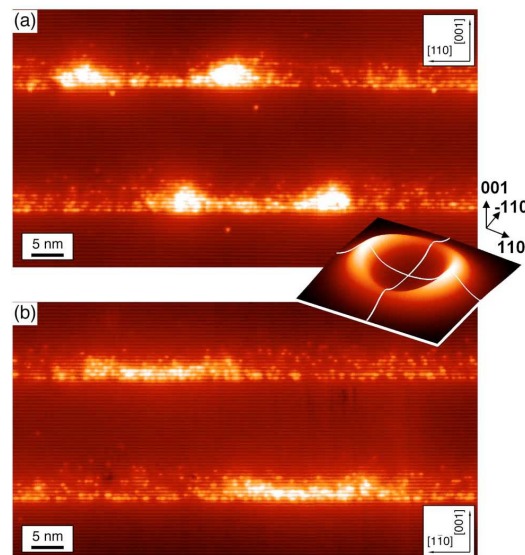


Figure 1.15: The X-STM images of: (a) the $[110]$ and (b) the $[1\bar{1}0]$ cross sections of the InGaAs/GaAs ringlike quantum dots. Inset shows a 3D view of the quantum dot (from Ref. [121]).

For example, the fabrication of the (In,Ga)As/GaAs ring by the Stranski-Krastanov growth starts with the formation of the InAs quantum dots on the GaAs substrate [79]. The epitaxial layer of GaAs is grown first on the GaAs substrate of the orientation $[100]$ at 600°C . The function of this layer is to ensure smooth surface during subsequent processing steps. Temperature is then lowered to 530°C and the substrate is irradiated with

the In and As atoms. In the experiment of Ref. [79] the quantity of InAs is chosen to correspond to 1.7 monolayers covering the whole substrate, and is slightly larger than the critical thickness. The layer then rearranges into randomly distributed quantum dots, which are immediately partially covered by the 4 nm thick layer of GaAs, and the growth is then interrupted for 30 seconds. During this time, the sample is kept at high temperature, therefore the annealing takes place. A consequence of the annealing and mechanical strain which arises from the covering layer [122] is transformation of the dots into the (almost complete) rings. The sketch of how the dots are transformed into the rings is shown in Fig. 1.14. This process also leads to intermixing between InAs and GaAs, therefore the ring becomes (In,Ga)As island in the matrix of GaAs. Also, the mole fraction of InAs is position-dependent [105].

After the rings were completed, they were characterized by the technique of cross-sectional scanning tunneling microscopy (X-STM) [114, 121]. Fig. 1.15 shows the X-STM image of the InGaAs/GaAs quantum ring. By comparing Figs. 1.14(a) and (b), we see that there exists slight anisotropy of the ring shape [105, 121], which has been recently theoretically studied [105, 123]. The X-STM images also indicate that the ring is not opened, but some portion of the quantum dot material resides inside the nominal ring opening after the dewetting process. Height of this layer is smaller than height of the ring's rim, but it profoundly affects the single particle and the excitonic energy spectra in magnetic field [123, 124], which will be explored in Chapters 6 and 7.

1.3 Bulk properties of Si, GaAs, InAs, and AlAs

The models of the electronic structure of the quantum wells and quantum dots analyzed in this thesis are based on the models of bulk semiconductors. Furthermore, the parameters of the bulk band structure are taken at the sinput of the electron and hole states calculations in nanostructures. Therefore, we briefly discuss the basic structural properties and the band structure of silicon (Si), gallium-arsenide (GaAs), indium-arsenide (InAs), and aluminium-arsenide (AlAs).

1.3.1 Silicon

Silicon is an elemental semiconductor of the group IV of the periodic table. The crystal structure of silicon is diamond cubic, whose feature is that each atom is tetrahedrally coordinated with the other silicon atoms [125]. The lattice constant of silicon is $a_0 = 0.357$ nm [126], and the unit cell of the silicon crystal is shown in Fig. 1.16.

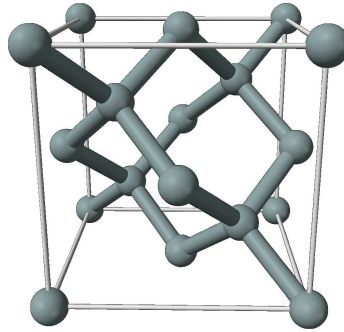


Figure 1.16: The unit cell of the silicon crystal (from Ref. [127]).

Silicon is an indirect semiconductor, as the band diagram in Fig. 1.17 shows. The valence-band (VB) top is located at the Γ ($\mathbf{k} = 0$) point in the Brillouin zone, and is double degenerate (fourfold if the spin degeneracy is taken into account) state of the heavy and light holes. The split-off band is separated from the heavy and light-hole bands by means of spin-orbit (SO) interaction. The spin-orbit split-off energy in silicon amounts to $\Delta_{SO} = 44$ meV, which is much lower than in GaAs, where $\Delta_{SO} = 341$ meV [25]. The energy minimum of the conduction band (CB) in silicon is a state whose wave vector is $k_0 = 0.85\pi/a_0$ and lies along the $[100]$ direction. Because of the crystal symmetry, there are six equivalent $\langle 100 \rangle$ directions, therefore six such minima exist. Along with the spin degeneracy, the state of the CB energy minimum is twelvefold degenerate.

Because the silicon band gap is indirect, it exhibits low optical absorption in comparison to direct-gap semiconductors (GaAs and InAs, for example). The interband transitions between the VB maximum and the CB minimum in the bulk silicon require participation of third particle, which is usually a phonon (see Fig. 1.18). A possible way to increase quantum efficiency of silicon for photonic applications is to confine charge carriers in a nanostructure [28, 129–132]. When the electrons and holes are confined, the conserva-

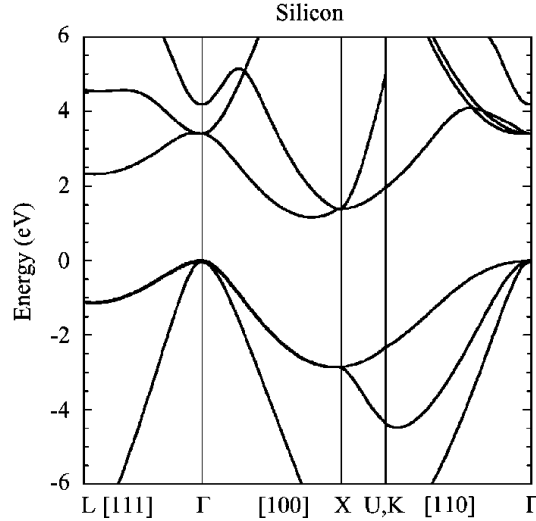


Figure 1.17: The diagram of the energy bands dispersion relations in silicon obtained from the 30-band $\mathbf{k} \cdot \mathbf{p}$ model (from Ref. [128]).

tion of the electron momentum is not a strict rule, hence direct transitions between the VB maximum and the CB minimum of energies comparable to the indirect transitions, might occur [133, 134]. Furthermore, when the quantum well width decreases, the band gap becomes direct, as was indeed observed in PL experiments on silicon quantum wells [29, 55, 61, 86], quantum wires [135, 136], and quantum dots [137, 138]. Moreover, the transition matrix elements are found to increase when the nanostructure dimensions decrease [55, 61, 133, 134], and mechanical strain may enhance such a trend [25].

1.3.2 III-V semiconductors

III-V semiconductors are binary compounds of the group-III and the group-V elements. The examples of such materials are GaAs, AlSb, InAs, InP, GaN, BN, etc. Most III-V compounds could have the zinc-blende crystal structure, yet some III-nitrides have the wurtzite crystal structure [125, 139]. The unit cell of a zinc-blende crystal is shown in Fig. 1.19. It consists of two interpenetrating face-centered cubic lattices which are separately occupied with the group-III atoms and the group-V atoms. Similar to the diamond crystal structure, each atom of the group-III (group-V) element is tetrahedrally coordinated with the atoms of the group-V (group-III) element. Therefore the unit cells of the zinc-blende and diamond crystals are similar (compare Figs. 1.16 and 1.19), except that

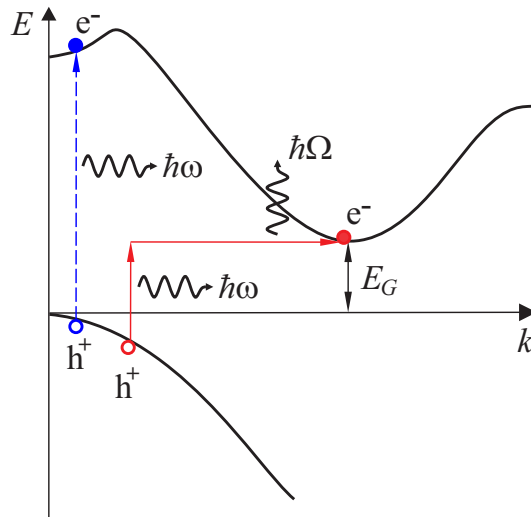


Figure 1.18: A sketch of the band diagram and two types of interband transitions in silicon: indirect optical transitions (red solid lines) are assisted by a phonon of the energy $\hbar\Omega$, whereas direct optical transitions (blue dashed line) do not need participation of third particle.

two different atoms occupy the unit cell of the zinc-blende crystal. It implies that in the zinc-blende crystals there does not exist center of the inversion symmetry, which has important consequences for their applications in spintronics [140, 141].

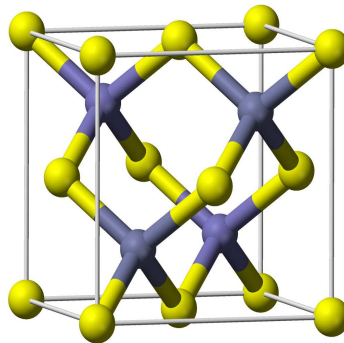


Figure 1.19: The unit cell of a zinc blende crystal (from Ref. [127]).

Different III-V compounds have different lattice constants, therefore their nanostructures are usually strained. For example, the lattice constant of InAs is 0.606 nm, and the lattice constant of GaAs is 0.565 nm [139]. It means that a thin layer of InAs embedded within two thick layers of GaAs is compressively strained. The theoretical analysis of the strain influence on the electron states in quantum wells usually assumes that the barriers

are infinitely thick and that the sample has infinite extension in the quantum well plane. It then follows that only the thin layer is strained, and thus it is simple to model the influence of the strain on the electron and hole subbands. In a quantum dot, however, the 3D island of one material (for example InAs) is embedded in the other material (for example GaAs), and equations of elasticity theory should be solved to find the strain distribution. Therefore, modelling of strained quantum dots could be quite involved.

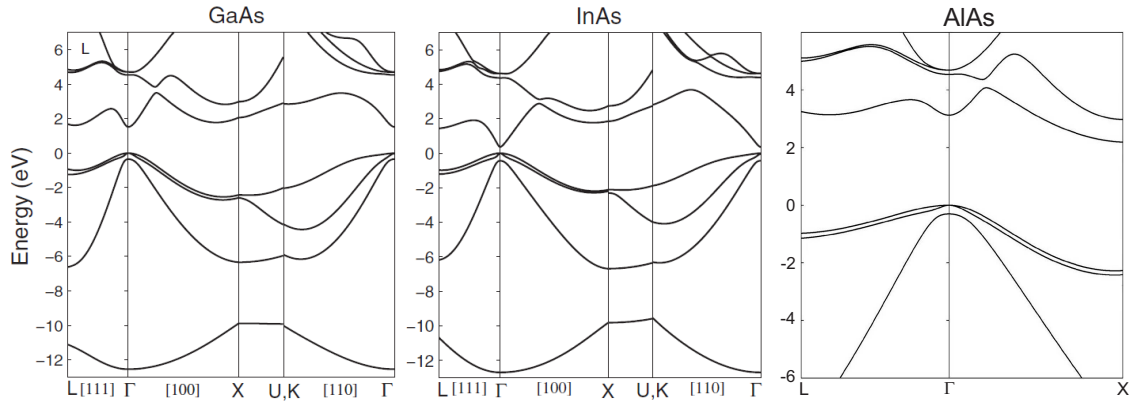


Figure 1.20: The band diagrams in GaAs, InAs and AlAs (from Refs. [142, 143]).

In addition to binary III-V compounds, alloys of III-V compounds are usually used to form nanostructures. The alloying might be used to realize strain-free nanostructures, such as those based on $\text{In}_{0.53}\text{Ga}_{0.47}\text{As}/\text{In}_{0.52}\text{As}_{0.48}\text{As}$ and $\text{In}_{0.51}\text{Ga}_{0.49}\text{As}/\text{InP}$ heterojunctions. However, GaAs and AlAs makes a lattice-matched system, and are alloyed to form $\text{Al}_x\text{Ga}_{1-x}\text{As}$, which is lattice matched to both GaAs and AlAs. It is one of the main reasons for popularity of the GaAs/ $\text{Al}_x\text{Ga}_{1-x}\text{As}$ nanostructures in both fundamental and applied research during the last few decades.

Along with Si/SiO₂ quantum wells, in this thesis we explore GaAs/(Al,Ga)As quantum wells and quantum dots, and also model strained (In,Ga)As/GaAs quantum dots. The band diagrams of GaAs, InAs, and AlAs are shown in Fig. 1.20. It is obvious that the energy gap in GaAs and InAs is direct, whereas AlAs has an indirect band gap, with the minimum of the conduction band located at the X point in the Brillouin zone. Nevertheless, $\text{Al}_x\text{Ga}_{1-x}\text{As}$ is an indirect semiconductor when $x < 0.4$. The top of the valence band is located at the Γ point in all three semiconductors, which is a consequence of the cubic symmetry of the unit cell. And similar to silicon, the $\mathbf{k} = 0$ state in the valence band is

a degenerate state of the heavy and light holes. Furthermore, GaAs and AlAs have wide band gaps ($E_g^\Gamma(\text{GaAs}) = 1.519$ eV, $E_g^X(\text{AlAs}) = 2.240$ eV, and $E_g^\Gamma(\text{AlAs}) = 3.099$ eV), whereas InAs is a narrow-gap semiconductor whose band gap is $E_g^\Gamma(\text{InAs}) = 0.417$ eV [139]. The band gaps in ternary alloys are determined from the empirical Vegard law [144]:

$$E_g(A_xB_{1-x}D) = xE_g(AD) + (1-x)E_g(BD) - Cx(1-x). \quad (1.1)$$

This interpolation formula describes quite well variation of the effective masses with the mole fractions. Here, the deviation from the linear dependence on the mole fractions is described by the last term, which is quadratic dependence on x , and is multiplied by the *bowing parameter* C [139].

1.4 Overview of the thesis

The present thesis deals with the application of the $\mathbf{k} \cdot \mathbf{p}$ theory to the electronic structure calculations. Four different nanostructures are considered:

1. Si/SiO₂ quantum wells;
2. GaAs/(Al,Ga)As quantum wells;
3. GaAs/(Al,Ga)As ringlike quantum dots;
4. (In,Ga)As/GaAs ringlike quantum dots.

The common property of all these nanostructures is that they are grown in the [001] direction. However, because of different band-structure of the materials they are composed from $\mathbf{k} \cdot \mathbf{p}$ models of different complexity are employed to calculate the electron and hole states in them. They are:

1. the single-band effective mass theory,
2. the 4-band Luttinger-Kohn model,
3. the 6-band Luttinger-Kohn model, and
4. the 30-band $\mathbf{k} \cdot \mathbf{p}$ model.

In Chapter 2 the basics of the $\mathbf{k} \cdot \mathbf{p}$ theory are given. The effective mass approximation is discussed. Also, the multiband $\mathbf{k} \cdot \mathbf{p}$ theory, which describes the hole states in the vicinity of the Γ point is derived using the perturbation theory for degenerate energy levels. The principles of the 30-band $\mathbf{k} \cdot \mathbf{p}$ Hamiltonian are explained. Finally, the application of $\mathbf{k} \cdot \mathbf{p}$ models to nanostructures through the envelope-function approximation is discussed.

In Chapters 3 and 4 Si/SiO₂ quantum wells grown along the [001] direction are considered using the 30-band $\mathbf{k} \cdot \mathbf{p}$ formalism. In Chapter 3 the electronic structure is calculated, and the method for removal of the spurious solutions is proposed. Also, the numerical stability of the method is discussed. Chapter 4 presents the calculation of the interband optical absorption. The transition energies and the interband transition matrix elements as function of the quantum well width are discussed. The results of the 30-band model are compared with the model of lower order.

Chapter 5 presents the results of the electronic-structure calculations of (Ga,As)/(Al,Ga)As quantum wells. The electron states obtained from the 30-band and the single-band Hamiltonian are compared. The hole states are calculated using the 30-band model and the 6-band Luttinger-Kohn model, and the results are compared. The Dresselhaus spin-orbit interaction in the conduction band is also considered.

Ringlike quantum dots are considered in Chapters 6 and 7. They are assumed to have the shape of a ring surrounding a disk. The electron states are calculated using the single-band effective mass model, whereas the hole states are obtained by the 4-band Luttinger-Kohn model. The influence of the dimensions of the GaAs/(Al,Ga)As ringlike quantum dots, which are grown by droplet epitaxy, is investigated in Chapter 6. (In,Ga)As/GaAs quantum dots in a perpendicular magnetic field are considered in Chapter 7. Here, the influence of the disk height variation on the Aharonov-Bohm oscillations of the electron and hole energy levels is explored. In order to examine how the presence of mechanical strain affects the Aharonov-Bohm oscillations, the energy level dependence on the magnetic field in the GaAs/(Al,Ga)As ringlike quantum dots is also computed.

The most important results of the thesis are summarized in Chapter 8.

Chapter 2

The multiband $\mathbf{k} \cdot \mathbf{p}$ theory

A widely used method of the electronic structure theory of semiconductors during the last few decades is the multiband $\mathbf{k} \cdot \mathbf{p}$ theory [123, 124, 145–147]. In essence, it is a kind of the linear variational method whose basis is formed out of the Bloch functions in the center of the Brillouin zone. It was initially employed to approximately describe the bulk band structure of semiconductors [148–150], and for cases of present imperfections [151] and external magnetic field [150]. But its application has been subsequently extended to semiconductor nanostructures [2].

By its construction, the multiband $\mathbf{k} \cdot \mathbf{p}$ theory takes into account spin-orbit interaction, therefore it provides a useful way to explore effects of importance for semiconductor spintronics [152–154]. Furthermore, it could accurately model a range of *internal effects* in both bulk semiconductors and semiconductor nanostructures, such as influences of impurities and mechanical strain. *External effects*, which are consequence of external electric and magnetic fields, are also straightforward to take into account in the theory.

In practical applications for nanostructures, the $\mathbf{k} \cdot \mathbf{p}$ theory exhibits numerous advantages over *ab initio* methods. In addition to being relatively simple, its use requires modest computational resources. Yet, it is able to quite accurately model the electron and hole dispersion relations in bulk semiconductors and semiconductor nanostructures. Furthermore, the method depends on small number of input parameters, which makes it a convenient choice for modelling the optical and transport properties of semiconductor nanostructures.

Since the dawn of work on the subject, which occurred around the middle of the

twentieth century, various $\mathbf{k} \cdot \mathbf{p}$ models were devised. The very difference between them is in number of the energy bands taken in the basis. For semiconductors which have the diamond and zinc-blende crystal structure, the 4-band and 6-band Luttinger-Kohn (LK) models are usually employed to compute the electronic structure of the valence band [2, 123, 124, 155, 156], whereas the 8-band model can model states in both the valence and conduction bands [147, 157–159]. Increase of the number of bands included in the basis makes modelling more complex, but generally brings the theoretical results closer to results of more elaborate approaches and experiment. However, models of multiparticle states based on the multiband $\mathbf{k} \cdot \mathbf{p}$ theory could be too complex, thus one usually relies on the single-band approximation to make model tractable [107, 123, 160]. Furthermore, use of the multiband $\mathbf{k} \cdot \mathbf{p}$ models is usually restricted to small regions in the Brillouin zone where the extrema of the conduction and valence bands are located [148–150]. Finally, use of the *ad hoc* formulated symmetrization rules is needed to make the Hamiltonian matrix Hermitian. But, this difficulty was overcome by the development of the $\mathbf{k} \cdot \mathbf{p}$ models which are suited for nanostructures and take into account spatial variation of parameters in the model [158, 161].

The $\mathbf{k} \cdot \mathbf{p}$ theory has been extended by taking into account 30 or even 40 zone-center states, which led to the models capable to accurately describe the dispersion relations of the energy bands in the whole Brillouin zone [128, 142, 143, 162, 163]. An important advantage of the multiband Hamiltonian of such large order is that it is capable to model indirect band-gap semiconductors and their nanostructures [25, 128, 164–166].

In this Chapter we briefly explain the $\mathbf{k} \cdot \mathbf{p}$ theory. The concept of the multiband $\mathbf{k} \cdot \mathbf{p}$ theory is first explained, and then employed to derive the single-band effective-mass theory. The derivation of the 6-band model Luttinger-Kohn models is then presented. Finally, we describe the 30-band model, and comment on how the multiband $\mathbf{k} \cdot \mathbf{p}$ theory is employed to compute the electron and hole states in semiconductor nanostructures.

2.1 The particle in a periodic potential

We start from the single-electron Schrödinger equation

$$H_0\Psi_{n\mathbf{k}}(\mathbf{r}) = E_n^0(\mathbf{k})\Psi_{n\mathbf{k}}(\mathbf{r}), \quad (2.1)$$

where H_0 denotes the microscopic Hamiltonian consisting of the kinetic part and the periodic crystal potential V_0 :

$$H_0 = \frac{p^2}{2m_0} + V_0(\mathbf{r}). \quad (2.2)$$

Solutions of equation (2.1) have the form of the Bloch functions,

$$\Psi_{n\mathbf{k}}(\mathbf{r}) = u_{n\mathbf{k}}(\mathbf{r})\exp(i\mathbf{k} \cdot \mathbf{r}). \quad (2.3)$$

Quite generally, spin-orbit interaction leads to notable effects on the band structure, and therefore should be included in the Hamiltonian,

$$H = H_0 + \frac{\hbar}{4m_0^2c^2}(\boldsymbol{\sigma} \times \nabla V_0) \cdot \mathbf{p}. \quad (2.4)$$

When Eqs. (2.1), (2.3) and (2.4) are combined, the following equation for the periodic part of the Bloch function $u_{n\mathbf{k}}$ is derived:

$$\begin{aligned} & \left[H_0 + \frac{\hbar}{m_0}\mathbf{k} \cdot \mathbf{p} + \frac{\hbar}{4m_0^2c^2}(\boldsymbol{\sigma} \times \nabla V_0) \cdot \mathbf{p} + \frac{\hbar}{4m_0^2c^2}(\boldsymbol{\sigma} \times \nabla V_0) \cdot \mathbf{k} \right] u_{n\mathbf{k}}(\mathbf{r}) \\ & = \left(E_n(\mathbf{k}) - \frac{\hbar^2k^2}{2m_0} \right) u_{n\mathbf{k}}(\mathbf{r}). \end{aligned} \quad (2.5)$$

It has the form of the Schrödinger equation, but contains \mathbf{k} -dependent terms. Because of the $\mathbf{k} \cdot \mathbf{p}$ term, it is called the $\mathbf{k} \cdot \mathbf{p}$ equation. The third term in the brackets is often neglected, because it is much smaller than the other terms [167, 168].

In order to solve equation (2.5), the $\mathbf{k} \cdot \mathbf{p}$ theory employs an idea of expanding $u_{n\mathbf{k}}$ into a set of the periodic parts of the Bloch functions in the center of the Brillouin zone u_{m0}

$$u_{n\mathbf{k}}(\mathbf{r}) = \sum_{m=1}^N c_m u_{m0}(\mathbf{r}). \quad (2.6)$$

Substituting Eq. (2.6) in Eq. (2.5) leads to the matrix eigenvalue problem:

$$\begin{bmatrix} H_{11} & H_{12} & \dots & H_{1N} \\ H_{21} & H_{22} & & \vdots \\ \vdots & & \ddots & \\ H_{N1} & \dots & & H_{NN} \end{bmatrix} \begin{bmatrix} c_1 \\ c_2 \\ \vdots \\ c_N \end{bmatrix} = E \begin{bmatrix} c_1 \\ c_2 \\ \vdots \\ c_N \end{bmatrix}. \quad (2.7)$$

The diagonal elements of this matrix arise from H_0 , whereas the off-diagonal matrix elements are due to the other three terms in equation (2.5). Because the basis is not complete, such a calculation is not exact, yet its accuracy can be systematically improved by increasing the basis order N . Also, error of computed energy levels due to incomplete basis is proportional to \mathbf{k} . Therefore, the $\mathbf{k} \cdot \mathbf{p}$ theory could be adopted to model states with small wave vector, which in fact mostly contribute to optical and transport processes in direct-band-gap semiconductor nanostructures.

In practice, when the basis order increases, the multiband $\mathbf{k} \cdot \mathbf{p}$ theory offers more accurate results, but with a tradeoff of more complex modelling. For direct band-gap semiconductors, such as GaAs, InAs and InSb, the Hamiltonian is usually a matrix of the order less than or equal 8. And the Hamiltonians of different N are given specific names. For example, the $\mathbf{k} \cdot \mathbf{p}$ theory for $N = 1$ is known as the *single-band effective mass theory*. The models which take into account $N = 4$ and $N = 6$ zone-center states in the valence band are called the *4-band and 6-band Luttinger-Kohn Hamiltonians*, respectively [145, 146, 150, 156]. The Hamiltonian of the order 8 which uses the basis of 6 zone-center states in the valence band and 2 zone-center states in the conduction band is simply called the *8-band model* and is sometimes referred to as the *Pidgeon-Brown model* [169]. The dispersion relations of the energy bands in direct semiconductors, which are determined from the $\mathbf{k} \cdot \mathbf{p}$ theory, agree quite well with experiments, but only for \mathbf{k} smaller than approximately 10% of the reciprocal lattice constant [170].

The most recent developments in the $\mathbf{k} \cdot \mathbf{p}$ theory are the derivations of the 30-band and 40-band models [25, 142, 165], which are able to accurately reproduce dispersion relations of the electrons in the conduction and valence bands in the whole Brillouin zone. Because of this property, they are named the *full-zone $\mathbf{k} \cdot \mathbf{p}$ models*. Hence, they could, in principle, be employed for modelling nanostructures made of indirect band-gap

semiconductors [25, 128, 143, 163–166]. The 30-band model will be presented later in this chapter, after we explain the details of the simpler $\mathbf{k} \cdot \mathbf{p}$ models which are employed in this work: the single-band effective mass theory, the 4-band Luttinger-Kohn model, and the 6-band Luttinger-Kohn model.

2.2 The single-band effective-mass model

The simplest $\mathbf{k} \cdot \mathbf{p}$ approach is the single-band effective mass model, which uses the basis of a single periodic part of the Bloch function in the center of the Brillouin zone. Even though Eq. (2.5) could be exactly solved, within the framework of the single-band $\mathbf{k} \cdot \mathbf{p}$ theory, the $\mathbf{k} \cdot \mathbf{p}$ and SO terms are considered to be small perturbations. Therefore Eq. (2.5) is solved by means of the perturbation theory [168]. Furthermore, the SO interaction negligibly affects the conduction band states in wide-band-gap direct semiconductors, hence it can be neglected.

All nanostructures analyzed in this thesis consist of semiconductors having the zinc-blende or the diamond crystal structures. In the case of the zinc-blende lattice, the lowest conduction band is composed of the zone-center states originating from the atomic s orbitals, and are therefore spherically symmetric. The momentum operator alters parity, which leads to the vanishing matrix elements of the $\mathbf{k} \cdot \mathbf{p}$ operator between the s -like states. Hence, according to the first order perturbation theory, there is no correction of the electron energy. However, the second-order correction is finite, and results into

$$E_n(\mathbf{k}) = E_n(0) + \frac{\hbar^2 k^2}{2m_0} + \frac{\hbar^2}{m_0^2} \sum_{l \neq n} \frac{|\mathbf{k} \cdot \langle u_{n0} | \mathbf{p} | u_{l0} \rangle|^2}{E_n(0) - E_l(0)}. \quad (2.8)$$

Here, the sum is performed over all the other zone-center states. According to the single-band $\mathbf{k} \cdot \mathbf{p}$ theory, the band dispersion relation is parabolic

$$E_n(\mathbf{k}) = E_n(0) + \frac{\hbar^2 k^2}{2m^*}, \quad (2.9)$$

and m^* is the *effective mass*

$$\frac{1}{m^*} = \frac{1}{m_0} + \frac{2}{k^2 m_0^2} \sum_{l \neq n} \frac{|\mathbf{k} \cdot \langle u_{n0} | \mathbf{p} | u_{l0} \rangle|^2}{E_n(0) - E_l(0)}. \quad (2.10)$$

This expression could be simplified by considering symmetry of the zone-center functions [167]. The periodic parts of the Bloch functions at $\mathbf{k} \neq 0$ are determined by the first-order perturbation theory,

$$u_{n\mathbf{k}} = u_{n0} + \frac{\hbar}{m_0} \sum_{l \neq n} \frac{|\mathbf{k} \cdot \langle u_{n0} | \mathbf{p} | u_{l0} \rangle|}{E_n(0) - E_l(0)} u_{l0}. \quad (2.11)$$

The accuracy of the single-band approach can be improved by taking into account spin-orbit interaction, which gives the dispersion relation of the form

$$E_n(\mathbf{k}) = E_n(0) + \frac{\hbar^2 k^2}{2m_0} + \frac{\hbar}{m_0} \mathbf{k} \cdot \langle u_{n0} | \boldsymbol{\pi} | u_{n0} \rangle + \frac{\hbar^2}{m_0^2} \sum_{l \neq n} \frac{|\mathbf{k} \cdot \langle u_{n0} | \boldsymbol{\pi} | u_{l0} \rangle|^2}{E_n(0) - E_l(0)}, \quad (2.12)$$

where

$$\boldsymbol{\pi} = \mathbf{p} + \frac{\hbar}{4m_0^2 c^2} (\boldsymbol{\sigma} \times \nabla V). \quad (2.13)$$

The single-band effective mass approach has been usually adopted to compute the conduction band dispersion relations in direct semiconductors. Since the zone-center wave functions are rarely accurately known, the effective mass values are extracted from experiments. Also, the accuracy of the method depends on difference between the energies of the conduction band bottom and other zone-center states. Therefore, if denominators in Eqs. (2.10) and (2.11) are large, as it appears in wide-gap semiconductors, the single-band effective-mass model could be quite accurate for practical applications. Furthermore, from equations of the single-band model it is obvious that *band mixing* refers to the matrix elements between the zone center states divided by differences between the zone center energies. Therefore, the band mixing is small if either the difference between the relevant energy levels is large, or if the linear momentum matrix elements are small (see Eq. 2.8). Furthermore, the single-band theory is a convenient approximation for computation of the states close to the minimum of the conduction band, i.e. when \mathbf{k} is much smaller than the reciprocal lattice constant. Fig. 2.1 shows the comparison of the conduction band dispersion relation in GaAs obtained by the single-band model, with

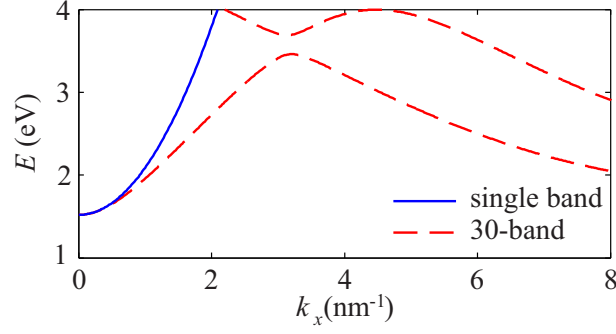


Figure 2.1: The conduction-band dispersion relation in the GaAs bulk computed by the effective-mass model (blue solid line) and the full-zone 30-band Hamiltonian (red dashed line).

the more accurate 30-band model. A good agreement is obviously achieved close to the Γ point, whereas the single-band approach fails to accurately describe the dispersion far away from the zone centre.

The derivation of the single-band theory that we presented implicitly assumes that the zone-center states are non-degenerate, as in the conduction band. The valence-band states are, however, degenerate in the center of the Brillouin zone, as we illustrated for a few semiconductors in Chapter 1. Therefore, the perturbation theory for degenerate states should be employed to model the valence-band states by the $\mathbf{k} \cdot \mathbf{p}$ theory.

2.3 The valence-band electronic structure

Because the heavy-hole and light-hole zone-center states are degenerate in the center of the Brillouin zone, the perturbation theory for degenerate energy levels should be adopted in the $\mathbf{k} \cdot \mathbf{p}$ approach. Such a $\mathbf{k} \cdot \mathbf{p}$ theory was developed by Dresselhaus, Kip, and Kittel (DKK) for the case of no spin-orbit interaction [149]. This model was subsequently extended by Luttinger and Kohn (LK) [150], who included spin-orbit interaction in the model. We note that DKK and LK used different symbols to label the zone-center states in the valence band, which originate from the p_x , p_y , and p_z atomic orbitals. They have symmetries of the x , y , and z axis, and are thus denoted by $|X\rangle$, $|Y\rangle$, and $|Z\rangle$ in the LK work. This is called *Kane's notation* [148]. On the other hand, DKK labelled the zone center states by $|yz\rangle$, $|zx\rangle$, and $|xy\rangle$, thereby referring to the directions along which the

zone center functions are even. It means that $|X\rangle = |yz\rangle$, $|Y\rangle = |zx\rangle$, and $|Z\rangle = |xy\rangle$.

2.3.1 The Dresselhaus-Kip-Kittel Hamiltonian

We start from the Hamiltonian

$$\left[\frac{p^2}{2m_0} + \frac{\hbar}{m_0} \mathbf{k} \cdot \mathbf{p} + V(\mathbf{r}) + \frac{\hbar^2 k^2}{2m_0} \right] u_{n\mathbf{k}}(\mathbf{r}) = E_n(\mathbf{k}) u_{n\mathbf{k}}(\mathbf{r}). \quad (2.14)$$

When $\mathbf{k} = 0$, the valence band states are threefold degenerate, due to the degeneracy of the p orbitals. DKK classified the zone center functions into two groups. The valence-band zone center states $u_{n0}^r = \varepsilon_r^+$, $r = 1, 2, 3$, are assumed to belong to the group A . All the other zone-center states u_{l0} are classified into the group B . According to the symmetry theory of the diamond-cubic and zinc-blende crystals, three A states belong to the Γ_{25l} representation [149] of the crystal point group, and are denoted by $\varepsilon_1^+ = |yz\rangle$, $\varepsilon_2^+ = |zx\rangle$ and $\varepsilon_3^+ = |xy\rangle$.

For $\mathbf{k} \neq 0$, Eq. (2.14) is solved by means of the perturbation theory for degenerate energy levels. Because of equal parities of the zone-center states, the first-order correction of the electron energy $\langle \varepsilon_r^+ | \mathbf{k} \cdot \mathbf{p} | \varepsilon_s^+ \rangle$ equals zero, which is similar to the result of the single-band model. Therefore, the second-order perturbation theory should be adopted [171] to find the solution of Eq. (2.14). Its matrix elements have the form [149]:

$$H_{rs} = \frac{\hbar^2}{m_0^2} \sum_{l \in B} \frac{\langle r | \mathbf{k} \cdot \mathbf{p} | l \rangle \langle l | \mathbf{k} \cdot \mathbf{p} | s \rangle}{E_n(0) - E_l(0)} = \frac{\hbar^2}{m_0^2} \sum_{i,j=x,y,z} k_i k_j \sum_{l \in B} \frac{\langle r | p_i | l \rangle \langle l | p_j | s \rangle}{E_n(0) - E_l(0)}. \quad (2.15)$$

Here, $|r\rangle$ and $|s\rangle$ denote the states of the group A , whereas $|l\rangle$ is a state of the group B .

Eq. (2.15) can be simplified by taking into account the particular symmetry of the zone-center states. We demonstrate it first for the diagonal matrix elements ($r = s$), and take $r = s = xy$ as an example. A consequence of the cubic symmetry [168] is that the term $i = j = 3$ in the second sum of Eq. (2.15), which has the form $\langle xy | p_i | l \rangle \langle l | p_j | xy \rangle$, is nonzero if x , y , or z appear in the matrix element even number of times, either as the subscripts of the momentum operators or the states labels. For example,

$$\langle xy | p_x | l \rangle \langle l | p_j | xy \rangle \quad (2.16)$$

is nonzero for only $j = x$. The other two nonzero cases are $i = j = y$ and $i = j = z$. Thus, the diagonal matrix element H_{33} has the following form:

$$H_{33} = \frac{\hbar^2}{m_0^2} \left[(k_x^2 + k_y^2) \sum_{l \in B} \frac{|\langle xy | p_x | l \rangle|^2}{E_n(0) - E_l(0)} + k_z^2 \sum_{l \in B} \frac{|\langle xy | p_z | l \rangle|^2}{E_n(0) - E_l(0)} \right], \quad (2.17)$$

and the expressions for the elements H_{11} and H_{22} are obtained by cyclic permutations of the coordinates in Eq. (2.17).

The off-diagonal ($r \neq s$) matrix elements are similarly simplified. As an example, we take the matrix element between the ε_3^+ ($r = xy$) and ε_1^+ ($s = yz$) zone-center functions,

$$\langle xy | p_i | l \rangle \langle l | p_j | yz \rangle. \quad (2.18)$$

As for the diagonal matrix elements, the total number of the coordinate symbols appearing either as the momentum indices or the states labels should be even. Therefore, it is straightforward to find that only

$$\langle xy | p_x | l \rangle \langle l | p_z | yz \rangle \quad (2.19)$$

and

$$\langle xy | p_z | l \rangle \langle l | p_x | yz \rangle \quad (2.20)$$

are nonzero. Thus, the off-diagonal element H_{31} has the form:

$$H_{31} = \frac{\hbar^2}{m_0^2} k_x k_z \sum_{l \in B} \frac{\langle xy | p_x | l \rangle \langle l | p_z | yz \rangle + \langle xy | p_z | l \rangle \langle l | p_x | xy \rangle}{E_n(0) - E_l}, \quad (2.21)$$

and H_{21} and H_{32} are determined by cyclic permutations of the indices in Eq. (2.21).

The presented second order perturbation theory gives as a result the matrix,

$$H_{DKK} = \begin{bmatrix} Lk_x^2 + M(k_y^2 + k_z^2) & Nk_x k_y & Nk_x k_z \\ Nk_x k_y & Lk_y^2 + M(k_x^2 + k_z^2) & Nk_y k_z \\ Nk_x k_z & Nk_y k_z & Lk_z^2 + M(k_x^2 + k_y^2) \end{bmatrix}, \quad (2.22)$$

which is known as the *Dresselhaus-Kip-Kittel Hamiltonian* [149]. From the description

on how H_{33} and H_{31} are derived, it is easy to determine that the coefficients L , M , and N have the following form:

$$L = \frac{\hbar^2}{m_0^2} \sum_{l \in B} \frac{|\langle xy | p_z | l \rangle|^2}{E_n(0) - E_l(0)}, \quad (2.23)$$

$$M = \frac{\hbar^2}{m_0^2} \sum_{l \in B} \frac{|\langle xy | p_x | l \rangle|^2}{E_n(0) - E_l(0)}, \quad (2.24)$$

and

$$N = \frac{\hbar^2}{m_0^2} \sum_{l \in B} \frac{\langle xy | p_x | l \rangle \langle l | p_z | yz \rangle + \langle xy | p_z | l \rangle \langle l | p_x | xy \rangle}{E_n(0) - E_l(0)}. \quad (2.25)$$

The complete Hamiltonian H_k is thus given by

$$H_k = \left(E_n(0) + \frac{\hbar^2 k^2}{m_0} \right) I_{3 \times 3} + H_{DKK}, \quad (2.26)$$

where $I_{3 \times 3}$ is the unit matrix of order 3.

2.3.2 The six-band Luttinger-Kohn model

Soon after Dresselhaus, Kip, and Kittel derived their model, Luttinger and Kohn extended it with the spin-orbit interaction terms:

$$H_{SO}(\mathbf{k}) = \frac{\hbar}{4m_0^2 c^2} (\boldsymbol{\sigma} \times \nabla V) \cdot \mathbf{p} + \frac{\hbar}{4m_0^2 c^2} (\boldsymbol{\sigma} \times \nabla V) \cdot \mathbf{k} = H_{SO}^p + H_{SO}^k. \quad (2.27)$$

It was indeed necessary, since the spin-orbit interaction effects on the valence band states in semiconductors are usually appreciable, in shear opposite to the conduction band. However, the term proportional to \mathbf{k} in Eq. (2.27) is much smaller than the term proportional to \mathbf{p} , and could thus be neglected [148, 170]. Since H_{SO} is spin dependent, the basis is doubled and contains the following functions: $\varepsilon_1^+ |\uparrow\rangle$, $\varepsilon_2^+ |\uparrow\rangle$, $\varepsilon_3^+ |\uparrow\rangle$, $\varepsilon_1^+ |\downarrow\rangle$, $\varepsilon_2^+ |\downarrow\rangle$ and $\varepsilon_3^+ |\downarrow\rangle$, where $|\uparrow\rangle$ and $|\downarrow\rangle$ are the eigenspinors of the spin-up and spin-down states. This basis is therefore formed out of the eigenstates of orbital momentum \mathbf{L} and spin, therefore it is called the LS basis.

The rest of the $\mathbf{k} \cdot \mathbf{p}$ Hamiltonian is not spin-dependent, therefore it is the DKK Hamiltonian (see Eq. (2.14)) [150]. However, Luttinger and Kohn changed the notation to $\varepsilon_1^+ = |X\rangle$, $\varepsilon_2^+ = |Y\rangle$ and $\varepsilon_3^+ = |Z\rangle$ [148]. Furthermore, H_k in Eq. (2.26) is written as

$H_k = E_n(0)I_{3 \times 3} + D$, where

$$D = \frac{\hbar^2 k^2}{2m_0} + H_{DKK} = \begin{bmatrix} A_L k_x^2 + B_L (k_y^2 + k_z^2) & C_L k_x k_y & C_L k_x k_z \\ C_L k_x k_y & A_L k_y^2 + B_L (k_x^2 + k_z^2) & C_L k_y k_z \\ C_L k_x k_z & C_L k_y k_z & A_L k_z^2 + B_L (k_x^2 + k_y^2) \end{bmatrix}. \quad (2.28)$$

Furthermore, the coefficients A_L , B_L , and C_L are given by

$$A_L = \frac{\hbar^2}{2m_0} + L, \quad (2.29)$$

$$B_L = \frac{\hbar^2}{2m_0} + M, \quad (2.30)$$

and

$$C_L = N. \quad (2.31)$$

The part of the multiband Hamiltonian which arises from the spin-orbit interaction can be derived by considering the p -like symmetry of the basis states, which lead to the single spin-orbit parameter in the model of the Γ_{25l} states,

$$\Delta \equiv -\frac{3i\hbar}{4m_0^2 c^2} \langle X | (\nabla V \times \mathbf{p})_y | Z \rangle. \quad (2.32)$$

In the employed LS basis, the total Hamiltonian is given by

$$H_{LK}^{LS}(\mathbf{k}) = E_n(0)I_{6 \times 6} + D \otimes I_{2 \times 2} + H_{SO}, \quad (2.33)$$

where H_{SO} denotes the part which describes spin-orbit interaction,

$$H_{SO} = \frac{\Delta}{3} \begin{bmatrix} 0 & -i & 0 & 0 & 0 & 1 \\ i & 0 & 0 & 0 & 0 & -i \\ 0 & 0 & 0 & -1 & i & 0 \\ 0 & 0 & -1 & 0 & i & 0 \\ 0 & 0 & -i & -i & 0 & 0 \\ 1 & i & 0 & 0 & 0 & 0 \end{bmatrix}. \quad (2.34)$$

H_{LK}^{LS} is known as the 6-band *Luttinger-Kohn Hamiltonian* [150].

From Eqs. (2.28), (2.34), and (2.33) we see that H_{LK}^{LS} is not a diagonal matrix even at $\mathbf{k} = 0$, but it could be made diagonal by changing the basis. Such a basis is straightforwardly derived by diagonalizing H_{SO} [148]:

$$\begin{aligned}
|3/2, 3/2\rangle &= -\frac{i}{\sqrt{2}} |(X + iY) \uparrow\rangle, \\
|3/2, 1/2\rangle &= (-i) \left[\frac{1}{\sqrt{6}} |(X + iY) \downarrow\rangle - \sqrt{\frac{2}{3}} |Z \uparrow\rangle \right], \\
|3/2, -1/2\rangle &= i \left[\frac{1}{\sqrt{6}} |(X - iY) \uparrow\rangle + \sqrt{\frac{2}{3}} |Z \downarrow\rangle \right], \\
|3/2, -3/2\rangle &= \frac{i}{\sqrt{2}} |(X - iY) \downarrow\rangle, \\
|1/2, 1/2\rangle &= \frac{i}{\sqrt{3}} [| (X + iY) \downarrow\rangle + |Z \uparrow\rangle], \\
|1/2, -1/2\rangle &= \frac{i}{\sqrt{3}} [| (X - iY) \uparrow\rangle - |Z \downarrow\rangle].
\end{aligned} \tag{2.35}$$

These basis functions have the symmetry of the atomic $|j, m_j\rangle$ states, where j and m_j denote the quantum numbers of the total angular momentum J and its projection onto the z axis J_z . It is easy to demonstrate that H_{SO} in Eq. (2.27) commutes with neither L^2 nor L_z , therefore the orbital quantum number l and the magnetic quantum number m are not good quantum numbers. However, H_{SO} commutes with J^2 and J_z , where $\mathbf{J} = \mathbf{L} + \mathbf{S}$ is the total angular momentum, hence j and m_j are good quantum numbers at $\mathbf{k} = 0$. This basis is enlisted in Eq. (2.35) and is called the JM_J basis.

The spin-orbit matrix in the JM_J basis is diagonal,

$$H'_{SO} = \frac{\Delta}{3} \begin{bmatrix} 1 & 0 & 0 & 0 & 0 & 0 \\ 0 & 1 & 0 & 0 & 0 & 0 \\ 0 & 0 & 1 & 0 & 0 & 0 \\ 0 & 0 & 0 & 1 & 0 & 0 \\ 0 & 0 & 0 & 0 & -2 & 0 \\ 0 & 0 & 0 & 0 & 0 & -2 \end{bmatrix}. \tag{2.36}$$

It is evident that the spin-orbit interaction breaks the sixfold degeneracy into the quadru-

plet of the $|3/2, m_j\rangle$ states and the doublet of the $|1/2, m_j\rangle$ states. The Hamiltonian is further simplified by setting the reference level for energy at the top of the valence band, therefore $E_n(0) = -\Delta/3$.

The $\mathbf{k} \cdot \mathbf{p}$ Hamiltonian in the JM_J basis which is the result of this theory is

$$H_{LK}(\mathbf{k}) = \begin{bmatrix} P+Q & R & S & 0 & \frac{1}{\sqrt{2}}R & \sqrt{2}S \\ R^* & P-Q & 0 & S & -\sqrt{2}Q & -\sqrt{\frac{3}{2}}R \\ S^* & 0 & P-Q & -R & -\sqrt{\frac{3}{2}}R^* & \sqrt{2}Q \\ 0 & S^* & -R^* & P+Q & -\sqrt{2}S^* & \frac{1}{\sqrt{2}}R^* \\ \frac{1}{\sqrt{2}}R^* & -\sqrt{2}Q^* & -\sqrt{\frac{3}{2}}R & -\sqrt{2}S & -\Delta+P & 0 \\ \sqrt{2}S^* & -\sqrt{\frac{3}{2}}R^* & \sqrt{2}Q^* & \frac{1}{\sqrt{2}}R & 0 & -\Delta+P \end{bmatrix}, \quad (2.37)$$

where

$$\begin{aligned} P &= -\frac{\hbar^2}{2m_0}\gamma_1 k^2, \\ Q &= -\frac{\hbar^2}{2m_0}\gamma_2 (k_x^2 + k_y^2 - 2k_z^2), \\ R &= 2\sqrt{3}\frac{\hbar^2}{2m_0}\gamma_3 k_z k_-, \\ S &= \sqrt{3}\frac{\hbar^2}{2m_0} \left[\left(\frac{\gamma_3 + \gamma_2}{2} \right) k_-^2 - \left(\frac{\gamma_3 - \gamma_2}{2} \right) k_+^2 \right], \\ k_{\pm} &= k_x \pm ik_y. \end{aligned} \quad (2.38)$$

The Hamiltonian in Eq. (2.37) is called the 6-band Luttinger-Kohn Hamiltonian [150]. The parameters γ_1 , γ_2 , and γ_3 are called the *Luttinger parameters* and are related to the effective masses of the valence-band electrons along certain directions. Also, the Luttinger parameters are related to the parameters of the *DKK* model, A_L , B_L , and C_L (see Eqs. (2.29)-(2.31)), according to:

$$\begin{aligned} \gamma_1 &= -\frac{2m_0}{3\hbar^2} (A_L + 2B_L), \\ \gamma_2 &= -\frac{m_0}{3\hbar^2} (A_L - B_L), \\ \gamma_3 &= -\frac{m_0}{3\hbar^2} C_L. \end{aligned} \quad (2.39)$$

The essential feature of the Luttinger-Kohn model is that the mixing with states out-

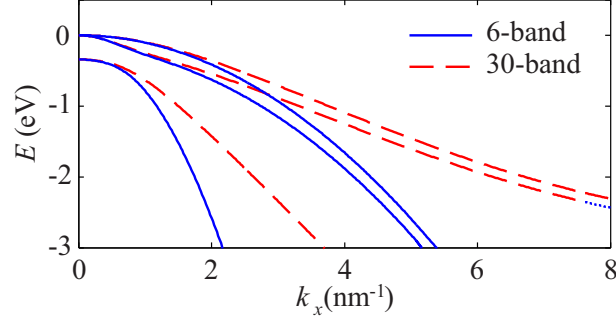


Figure 2.2: The valence-band dispersion relations in the GaAs bulk obtained by the 6-band Luttinger-Kohn Hamiltonian (blue solid line) and the full-zone 30-band Hamiltonian (red dashed line).

side the Γ_{25l} basis is treated as a perturbation, and leads to modifications of the Luttinger parameters. Influence of the group B bands diminishes when they largely differ from the zone center states of the group A . Thus, the 6-band Luttinger-Kohn Hamiltonian is a convenient choice for modelling the valence-band states in wide band-gap semiconductors, such as GaAs, InP, AlAs etc. Fig. 2.2 depicts the valence-band dispersion relation in GaAs along the $[100]$ direction obtained by the 6-band LK model and the full-zone 30-band model. It is evident that the results of the two models agree for small k , whereas when $k_x > 2 \text{ nm}^{-1}$ the difference between them becomes large.

For narrow band-gap materials, such as InSb, the perturbation theory fails to correctly describe the mixing between the Γ_{25l} valence band and the Γ_{2l} conduction band. This hurdle can be avoided if the mixing between the valence-band and conduction-band states is treated explicitly, as in the 8-band $\mathbf{k} \cdot \mathbf{p}$ model [147, 157]. The results can be improved if more than 8 bands are included in the basis, as in the 14-band theory [146], where the conduction p -like Γ_{15} band is included, or the more comprehensive 30-band models [25, 128]. One should be aware that the Luttinger parameters of these more complex models are renormalized by mixing with additional bands [147, 169, 172].

In some cases, however, smaller number of the bands can be taken in the basis. For example, the spin-orbit split-off energy in GaAs equals 341 meV, therefore the mixing between the split-off band with the heavy-hole and light-hole bands could be discarded if the energy range of interest is not below -100 meV from the valence-band top [145]. When Δ is large, the terms which mix the SO band with the HH and LH bands in the fifth

and sixth columns of the matrix in Eq. (2.37) can be discarded. It results in the 4-band Luttinger-Kohn model

$$H_{LK}^{4 \times 4}(\mathbf{k}) = \begin{bmatrix} P+Q & R & S & 0 \\ R^* & P-Q & 0 & S \\ S^* & 0 & P-Q & -R \\ 0 & S^* & -R^* & P+Q \end{bmatrix}, \quad (2.40)$$

The 4-band Luttinger-Kohn model could have limited accuracy when Δ is small. For example, $\Delta = 44$ meV in silicon [25], therefore the 6-band Luttinger-Kohn model should at least be used. Also, silicon has an indirect band gap, thus to model the electron states in the conduction band it is necessary to increase the number of bands. Such a model is the 30-band $\mathbf{k} \cdot \mathbf{p}$ theory, which has become recently popular for modelling semiconductors [25, 128, 143] and semiconductor quantum wells [134, 165, 166] with modest computational resources. In addition to being able to correctly model the electron states close to the conduction band minimum, this model allows the calculation of the hole states dispersion relations in the whole Brillouin zone. Therefore, it is suitable for modelling the interband optical transitions in silicon nanostructures.

2.4 The 30-band $\mathbf{k} \cdot \mathbf{p}$ Hamiltonian

The conduction band minimum in silicon is located at the point $\mathbf{k}_0 = (0.85, 0, 0)2\pi/a_0$ and five more points along the equivalent $\langle 100 \rangle$ directions in the Brillouin zone. Because of large \mathbf{k}_0 , the models which rely on the perturbation theory, like the DKK and LK models, cannot reproduce the dispersion relations for large \mathbf{k} . A possible solution of this problem was provided by Cardona and Pollak, who abandoned the use of the perturbation theory, and based their theory on the expansion of the bulk states in the zone-center Bloch functions of the s - p - and d -like symmetry [164] (see Table A.3).

The 15-band model of Cardona and Pollak was the first *full-zone* $\mathbf{k} \cdot \mathbf{p}$ approach, but was limited for practical use since spin-orbit interaction was not included in the model. It was Bailey et al. [162] who extended the Cardona-Pollak model with the spin-orbit interaction terms. The basis is constructed as the direct product of the zone-center states

Table 2.1: The basis functions of the 15-band Hamiltonian.

Band-edge (BE) states	Corresponding plane-wave (units π/a) and atomic states
Γ_{1l}	$[000] s^+$
Γ_{25l}	$[111] p^+$
Γ_{15}	$[111] p^+$
Γ_{2l}	$[111] s^-$
Γ_{1u}	$[111] s^+$
Γ_{12}	$[200] d^-$
Γ_{25u}	$[200] d^+$
Γ_{2u}	$[200] s^-$

in the 15-band model and the eigenspinors of the spin-up and spin-down states. The crystal symmetry is then taken into account which leads to the 30-band Hamiltonian [25]:

$$H_{30} = \begin{bmatrix} H_{\Gamma_{2u}}^{2 \times 2} & P_3^* H_k^{2 \times 6} & 0 & 0 & 0 & 0 & 0 & P_2^* H_k^{2 \times 6} \\ P_3 H_k^{6 \times 2} & H_{\Gamma_{25u}}^{6 \times 6} & R_1 H_k^{6 \times 4} & 0 & 0 & Q_1 H_k^{6 \times 6} & P_1 H_k^{6 \times 2} & H_{\Gamma_{25u}, \Gamma_{25l}}^{SO} \\ 0 & R_1^* H_k^{4 \times 6} & H_{\Gamma_{12}}^{4 \times 4} & 0 & 0 & 0 & 0 & R_0^* H_k^{4 \times 6} \\ 0 & 0 & 0 & H_{\Gamma_{1u}}^{2 \times 2} & 0 & T_0 H_k^{2 \times 6} & 0 & 0 \\ 0 & 0 & 0 & 0 & H_{\Gamma_{1l}}^{2 \times 2} & T_1 H_k^{2 \times 6} & 0 & 0 \\ 0 & Q_1^* H_k^{6 \times 6} & 0 & T_0^* H_k^{6 \times 2} & T_1^* H_k^{6 \times 2} & H_{\Gamma_{15}}^{6 \times 6} & 0 & Q_0^* H_k^{6 \times 6} \\ 0 & P_1^* H_k^{2 \times 6} & 0 & 0 & 0 & 0 & H_{\Gamma_{2l}}^{2 \times 2} & P_0^* H_k^{2 \times 6} \\ P_2 H_k^{6 \times 2} & H_{\Gamma_{25l}, \Gamma_{25u}}^{SO} & R_0 H_k^{6 \times 4} & 0 & 0 & Q_0 H_k^{6 \times 6} & P_0 H_k^{6 \times 2} & H_{\Gamma_{25l}}^{6 \times 6} \end{bmatrix}. \quad (2.41)$$

Here, the symbol $i \times j$ in the subscript of the matrix element denotes the block matrix having i rows and j columns. The block matrices on the main diagonal have the forms

$$\begin{aligned} H_{\Gamma}^{2 \times 2} &= \left(E_{\Gamma} + \frac{\hbar^2 k^2}{2m_0} \right) I_{2 \times 2}, \\ H_{\Gamma}^{4 \times 4} &= \left(E_{\Gamma} + \frac{\hbar^2 k^2}{2m_0} \right) I_{4 \times 4}, \\ H_{\Gamma}^{6 \times 6} &= \left(-\frac{\Delta_{\Gamma}}{3} + E_{\Gamma} + \frac{\hbar^2 k^2}{2m_0} \right) I_{6 \times 6} + H_{\Gamma}^{SO}, \end{aligned} \quad (2.42)$$

and H_{Γ}^{SO} is the 6×6 spin-orbit matrix defined in equation (2.34). These matrices obviously depend on the energies of the zone center states E_{Γ} and the spin-orbit coupling energy Δ_{Γ} .

The block matrices positioned off-diagonally in Eq. (2.41) are given by

$$H_k^{2 \times 6} = \begin{bmatrix} k_x & k_y & k_z & 0 & 0 & 0 \\ 0 & 0 & 0 & k_x & k_y & k_z \end{bmatrix}, \quad (2.43)$$

$$H_k^{4 \times 6} = \begin{bmatrix} 0 & \sqrt{3}k_y & -\sqrt{3}k_z & 0 & 0 & 0 \\ 2k_x & -k_y & -k_z & 0 & 0 & 0 \\ 0 & 0 & 0 & 0 & \sqrt{3}k_y & -\sqrt{3}k_z \\ 0 & 0 & 0 & 2k_x & -k_y & -k_z \end{bmatrix}, \quad (2.44)$$

$$H_k^{6 \times 6} = \begin{bmatrix} 0 & k_z & k_y & 0 & 0 & 0 \\ k_z & 0 & k_x & 0 & 0 & 0 \\ k_y & k_x & 0 & 0 & 0 & 0 \\ 0 & 0 & 0 & 0 & k_z & k_y \\ 0 & 0 & 0 & k_z & 0 & k_x \\ 0 & 0 & 0 & k_y & k_x & 0 \end{bmatrix}, \quad (2.45)$$

and $H^{6 \times 2}$ and $H_k^{6 \times 4}$ are transpose of $H^{2 \times 6}$ and $H_k^{4 \times 6}$,

$$H_k^{6 \times 2} = \left(H_k^{2 \times 6} \right)^T, \quad H_k^{6 \times 4} = \left(H_k^{4 \times 6} \right)^T. \quad (2.46)$$

$P_0, P_1, P_2, P_3, Q_0, Q_1, R_0, R_1, T_0$ and T_1 in Eq. (2.41) denote the matrix elements of the electron momentum \mathbf{p} , and are given in Table A.3. Note that there are 10 independent matrix elements of \mathbf{p} and 4 spin-orbit parameters in semiconductors having the diamond crystal structure, such as silicon and germanium (see Fig. 2.3(a)). Usually, energy is measured with respect to $E_{\Gamma_{25l}}$, i.e. it is usually assumed that $E_{\Gamma_{25l}} = 0$ [25, 164].

The essential aspect of the $\mathbf{k} \cdot \mathbf{p}$ theory is that just symmetry, not the exact shape, of the basis (zone-center) functions should be known before the multiband Hamiltonian is derived. Therefore, the parameters of the 30-band model, like the momentum matrix elements, could not be determined from this theory, but are obtained from comparison of the theoretical results with measurements or first-principle calculations [25, 128, 162, 164].

We note that the Hamiltonian in Eq. (2.41) is valid for semiconductors having the di-

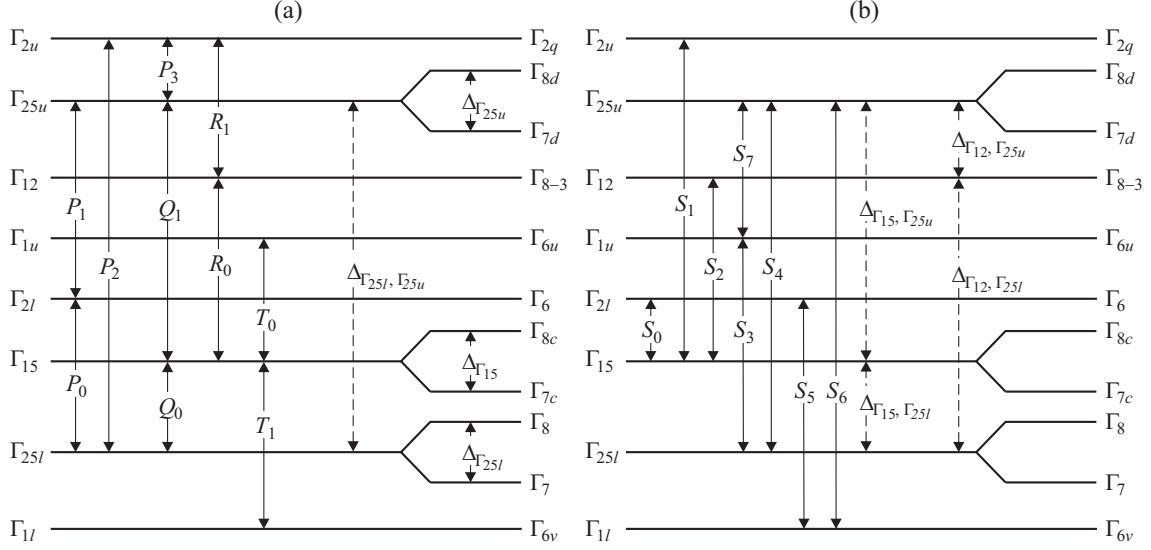


Figure 2.3: A schematic representation of the 30-band zone-center energy levels. (a) The matrix elements of the momentum and spin-orbit interaction in a diamond-cubic semiconductor are included in the diagram. (b) Illustration of the additional momentum and spin-orbit matrix elements which appear in the theory and are a consequence of the lacking inversion symmetry in zinc-blende semiconductors. The left-positioned symbols represent the notation from Ref. [164], while right-positioned symbols are from T_d double-group notation from Ref. [128].

among cubic crystal structure. For the zinc-blende semiconductors, which do not possess a center of inversion symmetry, in addition to 10 mentioned momentum matrix elements, there are 8 others [128] (see Fig. 2.3(b)). Also, 4 additional spin-orbit parameters emerge in the zinc-blende case [128]. Nonetheless, the experimental dispersion relations could be fitted with smaller number of parameters, thus there could be less than 18 nonzero elements [128, 143], which simplifies the calculation. The values of the non-zero momentum matrix elements and the spin-orbit parameters of the 30-band model for Si, GaAs, and AlAs are given in the Appendix.

The number of bands taken into account in the model has been subsequently extended to 34 [163] and 40 [142]. In addition to modelling the bulk band structure of Si, GaAs, InAs, InSb, InP, and other semiconductors, the 30-band theory has been adopted to model the subbands in quantum-well structures [165, 166, 173]. For such cases, it is implemented within the framework of the envelope function approximation.

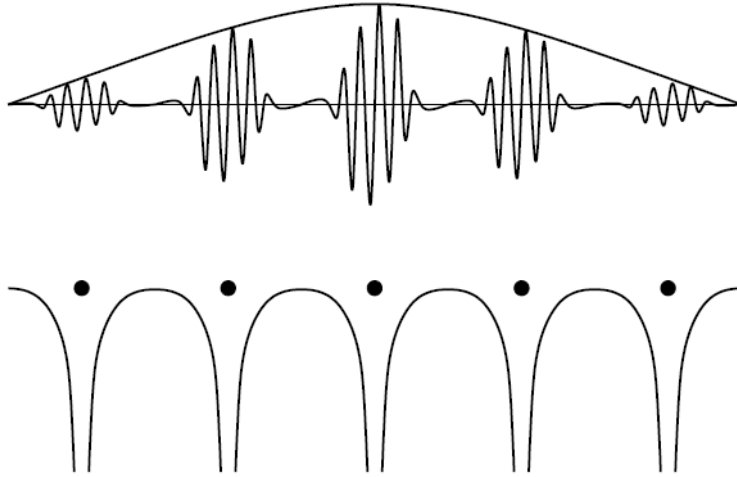


Figure 2.4: The illustration of the electron wavefunction in the EFA formalism (the upper part) and periodic potential (from Ref. [167]).

2.5 The envelope function approximation

Motion of the electrons in semiconductors might be perturbed by external causes, such as electric field, magnetic field, or mechanical stress. In some cases, the perturbation has an internal character, arising from an impurity, band offsets, or mechanical strain due to lattice mismatch. If the perturbing potential is a slowly varying function on the scale of the lattice constant, the appropriate and quite accurate description of the electronic structure is provided by the envelope function approximation [167]. In this approach, the electron states are found from the single-electron Schrödinger equation,

$$\left[\frac{(-i\hbar\nabla)^2}{2m_0} + V_0(\mathbf{r}) + \frac{\hbar}{4m_0^2c^2} (-i\hbar\nabla) \cdot (\boldsymbol{\sigma} \times \nabla V_0) + V(\mathbf{r}) \right] \chi(\mathbf{r}) = E\chi(\mathbf{r}), \quad (2.47)$$

where $V_0(\mathbf{r})$ is the periodic potential of the crystal lattice, $V(\mathbf{r})$ represents the slowly varying perturbation, and $\chi(\mathbf{r})$ denotes the wave function of the electron. The perturbation is assumed to be small, therefore, the spin-orbit interaction is assumed to depend on V_0 only.

To solve Eq. (2.47), we write $\chi(\mathbf{r})$ as

$$\chi(\mathbf{r}) = \sum_{l', \sigma'} \psi_{l' \sigma'}(\mathbf{r}) u_{l'0}(\mathbf{r}) |\sigma'\rangle, \quad (2.48)$$

where $u_{l'0}(\mathbf{r})$ denote the zone-center Bloch function of the band l' , $|\sigma'\rangle$ is the eigenspinor of the spin-up or the spin-down state, and $\psi_{l' \sigma'}(\mathbf{r})$ are the position-dependent functions, which are subsequently assumed to vary slowly over the crystal unit cell. We note that the kets $u_{l'0}|\sigma'\rangle$, having the periodicity of the crystal lattice, are employed here as the basis functions, yet the expansion coefficients are not constant, otherwise $\chi(\mathbf{r})$ would be periodic. The form of the solution in Eq. (2.48) is well suited for slowly varying $V(\mathbf{r})$, when $\psi_{l' \sigma'}$'s are almost constant in the crystal unit cell. In such a case, $\psi_{l' \sigma'}(\mathbf{r})$'s represent the envelopes of the $u_{l'0}(\mathbf{r})$ functions, and are therefore called the *envelope functions* (see Fig. 2.4).

The procedure to solve the Schrödinger equation (2.47) starts with its multiplication by the conjugate of the basis function $u_{l'0}|\sigma'\rangle$. The resulting equation is then integrated over the crystal unit cell, with an assumption that $V(\mathbf{r})$ is a slowly varying function in the cell, such that it can be approximately taken to be constant and taken out of the integral [168]. This derivation gives the system of the differential equations

$$\begin{aligned} \sum_{l', \sigma'} \left\{ \left[E_{l'}(0) + \frac{-i\hbar\nabla}{2m_0} + V(\mathbf{r}) \right] \delta_{\sigma\sigma'} \delta_{ll'} \right. \\ \left. + \frac{1}{m_0} (-i\hbar\nabla) \cdot \mathbf{P}_{l\sigma l' \sigma'} + \Delta_{l\sigma l' \sigma'} \right\} \psi_{l' \sigma'}(\mathbf{r}) \\ = E \psi_{l\sigma}(\mathbf{r}). \end{aligned} \quad (2.49)$$

Here, $\mathbf{P}_{l\sigma l' \sigma'}$ and $\Delta_{l\sigma l' \sigma'}$ denote the linear-momentum matrix element and the spin-orbit matrix element, respectively. We previously showed that the multiband $\mathbf{k} \cdot \mathbf{p}$ theory of the bulk semiconductor represents a system of linear equations where the electron wave vector \mathbf{k} is good quantum number (see Eqs. (2.7) and (2.3)). However, when the translational symmetry of the crystal is perturbed, \mathbf{k} is not good quantum number anymore. Hence, opposite to the bulk case, where all the parameters of the Hamiltonian are constants, the envelope functions $\psi_{l\sigma}(\mathbf{r})$ in a nanostructure are determined from the system of the differential equations. This theory is called the *multiband envelope-function approximation*

(MEFA), and has the form

$$H\Psi = E\Psi, \quad (2.50)$$

where H is the MEFA Hamiltonian, and Ψ is the multiband envelope function spinor, $\Psi = [\psi_{l\sigma}(\mathbf{r})]$.

Note that Eq. (2.50) has the same form as Eq. (2.7) which was derived for the bulk case, except that the electron wave vector is not good quantum number. Furthermore, the vector of the expansion coefficients is replaced with the envelope function spinor. Because of this similarity, the MEFA Hamiltonian for a nanostructure can be obtained directly from the bulk Hamiltonian by means of the substitution $\mathbf{k} \rightarrow -i\nabla$, and adding the potential $V(\mathbf{r})$ to the diagonal terms of the Hamiltonian matrix [167]. Furthermore, the material parameters, such as the effective masses and the Luttinger parameters, are usually position dependent in the nanostructure. Therefore, care should be taken to write the Hamiltonian in the Hermitian form. It is established by imposing the symmetrization rules [174, 175]

$$\begin{aligned} a(\mathbf{r})k_\alpha &\rightarrow \frac{1}{2} [a(\mathbf{r})k_\alpha + k_\alpha a(\mathbf{r})], \\ a(\mathbf{r})k_\alpha k_\beta &\rightarrow \frac{1}{2} [k_\alpha a(\mathbf{r})k_\beta + k_\beta a(\mathbf{r})k_\alpha], \\ &\alpha, \beta \in \{x, y, z\}. \end{aligned} \quad (2.51)$$

We note that an essential condition for the application of the envelope-function approximation is slow variation of both the perturbing potential and the envelope functions on the scale of the lattice constant. In compositional nanostructures the potential varies almost abruptly at a heterojunction, but the envelope function approximation could be used even for that case. As a matter of fact, the envelope function approximation is not able to describe well the wave function χ close to interfaces between different semiconductors [161, 176]. Nevertheless, these regions are quite narrow, and therefore the inaccurately determined envelope functions in them does not appreciably affect modeling the overall localization of the electrons in the nanostructure. The situation is however different if layers of the nanostructure are ultrathin (in practice just a few monolayers thick). In this case, the wave function $\chi(\mathbf{r})$ could vary substantially in the unit cell, thus the MEFA is not able to give quantitatively correct result. Nonetheless, the multiband $\mathbf{k} \cdot \mathbf{p}$ theory has been adopted to compute states in various nanostructures. Yet, an empirical criterion that

no any dimension of the system is comparable to the size of the crystal unit cell should be obeyed for a successful application of the theory [168].

2.6 Nanostructures in a magnetic field

We previously noted that external fields are straightforward to include in the MEFA Hamiltonian, as could be demonstrated here, when external magnetic field \mathbf{B} is applied. The standard prescription to model effects of the applied magnetic field on the electron states is to substitute the canonical momentum \mathbf{p} with the mechanical momentum $\Pi = -i\hbar\nabla + e\mathbf{A}$,

$$\mathbf{p} \rightarrow -i\hbar\nabla + e\mathbf{A}. \quad (2.52)$$

Here, \mathbf{A} denotes the magnetic vector potential, which obeys $\mathbf{B} = \nabla \times \mathbf{A}$, and e is the elementary charge. Magnetic field also causes the *Zeeman effect*, which is manifested by splitting of the spin degenerate states. The later could not be described within the nonrelativistic quantum mechanics. Rather, the relativistic Dirac equation should be used to model the Zeeman effect in atomic systems [171]. The result of this theory is that the states are spin split by $g\mu_B\boldsymbol{\sigma} \cdot \mathbf{B}$, where $g \approx 2$ is the Landé g -factor and μ_B is the Bohr magneton. The single-particle Hamiltonian is therefore given by

$$H = \frac{(-i\hbar\nabla + e\mathbf{A})^2}{2m_0} + V_0(\mathbf{r}) + \frac{\hbar}{4m_0^2c^2} (-i\hbar\nabla + e\mathbf{A}) \cdot (\boldsymbol{\sigma} \times \nabla V_0) + V(\mathbf{r}) + \frac{g}{2}\mu_B\boldsymbol{\sigma} \cdot \mathbf{B}. \quad (2.53)$$

The MEFA Hamiltonian is constructed from this Hamiltonian by assuming that the electron wavefunction is given by Eq. (2.48). In the single-band effective-mass theory, and for magnetic field oriented along the z direction, it leads to equation

$$\begin{aligned} H_e\Psi_e &= \left(-\frac{\hbar^2}{2m^*}\nabla^2 - \frac{i\hbar eB}{m^*}\frac{\partial}{\partial\varphi} + \frac{(eB\rho)^2}{8m^*} \pm \frac{g_{eff}}{2}\mu_BB + V_e(\mathbf{r}) \right) \Psi_e \\ &= E\Psi_e, \end{aligned} \quad (2.54)$$

where we assume that the magnetic field is oriented along z -axis and that the vector potential is written in the symmetric gauge:

$$\mathbf{A} = \frac{1}{2} \mathbf{B} \times \mathbf{r} = \frac{B\rho}{2} \mathbf{e}_\varphi. \quad (2.55)$$

In Eq. (2.54) the plus and minus sign correspond to the spin up and spin down, respectively. Also, the Landé g -factor is replaced by the effective Landé g -factor g_{eff} , which takes into account the modifications of the g -factor by the peculiar electronic structure of the semiconductor, and is straightforwardly modeled by the perturbation theory.

Modelling the effects of the magnetic field oriented along the [001] direction on the hole energy spectra employs the substitution $\mathbf{p} \rightarrow \mathbf{\Pi}$ and takes into account the Zeeman term through

$$H_z = i\kappa \frac{\hbar^2}{m_0} [k_x, k_y] \mathcal{J}_z = \hbar\omega_c \mathcal{J}_z. \quad (2.56)$$

Here ω_c denotes cyclotron frequency, κ is the fourth Luttinger parameter [177], and \mathcal{J}_z is a diagonal matrix of the form:

$$\mathcal{J}_z = \text{diag}(j_{z1}, j_{z2}, j_{z3}, j_{z4}) = \text{diag}(+3/2, +1/2, -1/2, -3/2). \quad (2.57)$$

Finally, we note that s and m_s are not quantum numbers in the presence of the spin-orbit coupling, but rather j_z . However, as Eq. (2.57) indicates, the states of different j_z are differently affected by the magnetic field, which leads to the splitting of the hole energy states in the magnetic field as well.

2.7 Modelling strained quantum dots

As we explained in Chapter 1, most semiconductor combinations which make nanostructures are mutually lattice mismatched. In quantum dots, distribution of mechanical strain is nonuniform and anisotropic, which affects the energy levels in a nontrivial way. Strain is straightforwardly taken into account in the $\mathbf{k} \cdot \mathbf{p}$ theory [178]. However, before modelling its influence on the electron states in quantum dots, the strain distribution should be computed, which is done by either the continuum-mechanical model [179, 180]) or an

atomistic model, such as the Keating's valence force field model [181].

The strained quantum dots analyzed in this thesis have axially symmetric shapes, and are based on the (In,Ga)As/GaAs system. The strain appears due to the lattice mismatch between (In,Ga)As and GaAs, and is computed by the approach of Downes, which applied the Eshelby inclusion theory [182] under the approximation of isotropic elasticity [180, 183]. The component of the strain tensor ε_{ij} in this theory is expressed by

$$\varepsilon_{ij}(\mathbf{r}) = -\varepsilon_0 \Theta(\mathbf{r}) - \frac{\varepsilon_0}{4\pi} \frac{1+\nu}{1-\nu} \oint_{S'} \frac{(x_i - x'_i)}{|\mathbf{r} - \mathbf{r}'|^3} dS'_j. \quad (2.58)$$

Here ε_0 denotes the lattice mismatch between the dot and the matrix $\varepsilon_0 = (a_d - a_m)/a_m$, x_i is i -th component of the position vector \mathbf{r} , Θ is unity inside the dot and zero otherwise, and ν is the Poisson ratio which is taken to be equal to 1/3. The integration is done over the surface of the dot S' . It is straightforward to show that the hydrostatic strain is

$$\varepsilon_{hyd} = \sum_i \varepsilon_{ii} = \begin{cases} -\varepsilon_0 & \text{in the dot} \\ 0 & \text{in the matrix} \end{cases}. \quad (2.59)$$

The influence of the strain on the electron and hole energy spectra is modeled by the Pikus-Bir theory of invariants [178]. To form the strain dependent part of the Hamiltonian H_{st} the following substitution

$$k_i k_j \rightarrow \varepsilon_{ij} \quad (2.60)$$

should be done in the kinetic part of the multiband Luttinger-Kohn Hamiltonian H_k , whose form was given in Sec. 2.3. The total multiband Hamiltonian is then

$$H = H_{LK} + H_{st} + V(\mathbf{r})I, \quad (2.61)$$

where V is the confining potential which is assumed to arise solely from the valence-band offset between (In,Ga)As and GaAs.

The shear components of the strain tensor are much smaller than the normal strains (the diagonal components of the strain tensor), except in rather localized regions close to the dot boundary. Therefore, the shear strains could be neglected [123, 184], with-

out substantial loss of accuracy of the electronic structure calculation. Therefore, in our approach H_{st} depends on the diagonal components of the strain tensor, and furthermore the off-diagonal elements of H_{st} are all zero [123]. For such a case, it is convenient to introduce the effective potentials. In our model of the quantum dot states we adopted the 4-band $\mathbf{k} \cdot \mathbf{p}$ model to compute the hole states, and the single-band effective-mass theory is used to determine the electron states in the conduction band. Therefore, the effective potentials for the heavy holes, light holes, and electrons, V_{hh} , V_{lh} , and V_e are defined as [160, 184]

$$V_{hh}(\mathbf{r}) = a_v(\varepsilon_{xx} + \varepsilon_{yy} + \varepsilon_{zz}) + b(\varepsilon_{xx}/2 + \varepsilon_{yy}/2 - \varepsilon_{zz}) + V_{off,h}(\mathbf{r}), \quad (2.62a)$$

$$V_{lh}(\mathbf{r}) = a_v(\varepsilon_{xx} + \varepsilon_{yy} + \varepsilon_{zz}) - b(\varepsilon_{xx}/2 + \varepsilon_{yy}/2 - \varepsilon_{zz}) + V_{off,h}(\mathbf{r}), \quad (2.62b)$$

$$V_e(\mathbf{r}) = a_c(\varepsilon_{xx} + \varepsilon_{yy} + \varepsilon_{zz}) + V_{off,e}(\mathbf{r}). \quad (2.62c)$$

Here, a_c , a_v , and b denote the deformation potentials, and $V_{off,e}$ and $V_{off,h}$ are the confining potentials due to the offsets between the valence and the conduction bands, respectively. In the present work, the energies of the band extrema in the matrix far away from the dot boundary, where full strain relaxation is achieved, are taken as the reference energies for the effective potentials.

2.8 Spurious solutions in the MEFA

The electronic structure calculation of nanostructures using the MEFA and the $\mathbf{k} \cdot \mathbf{p}$ model might produce nonphysical states known as *spurious solutions*. They exhibit a few unusual properties, such as presence in the bandgap or highly-oscillatory behavior. Their properties and the origin have been extensively studied, and various schemes for their removal have been proposed [158, 161, 176, 185–189].

Use of inappropriate boundary conditions was usually associated with the appearance of spurious solutions. The theory which aimed to establish the appropriate boundary conditions in the MEFA applied to nanostructures was developed by M. Burt and B. Foreman [161, 176, 187, 190]. They considered how the envelope functions in the 6-band and 8-band models should be connected across an abrupt heterojunction. Because of inevitable

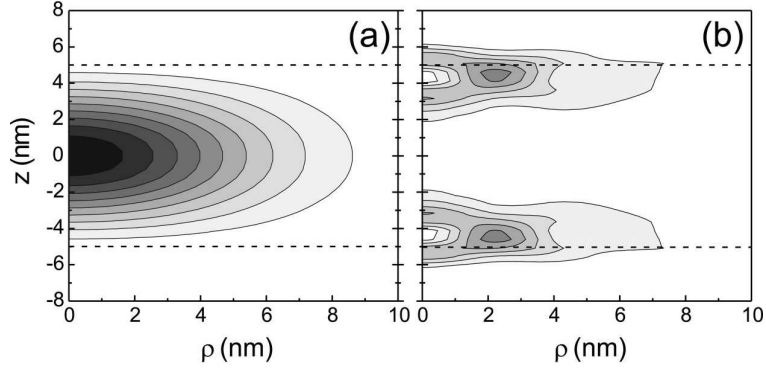


Figure 2.5: The probability density of the hole ground state in the parabolic InAs/GaAs quantum dot in the perpendicular magnetic field $\mathbf{B} = 40$ T calculated using (a) the Burt-Foreman 8-band model, and (b) the symmetrized 8-band model (from Ref. [158]).

differences between the zone-center Bloch-states u_{n0} in different materials, the ad-hoc symmetrization rules in Eq. (2.51) may fail to produce the accurate boundary conditions at heterojunctions. Burt and Foreman questioned those rules, and proposed a different operator ordering, which was extensively studied in Ref. [161].

In the Burt-Foreman theory different parameters, denoted by σ , π , and δ appear, and they take into account the influence of the s -like, p -like and d -like bands outside the basis set, respectively. The operator ordering has a peculiar form in the *Burt-Foreman* (BF) Hamiltonian [161]. However, when there is no compositional variation in the system, as in bulk semiconductor, those parameters become related to the Luttinger parameters. This theory was later extended by explicitly taking into account the mixing with the conduction band [190], and was found to efficiently remove spurious solutions, as Fig. 2.5 illustrates. The probability density of the ground hole state in the InAs/GaAs quantum dot obtained by the BF theory is shown Fig. 2.5(a). It has quite regular shape. On the other hand, when the ad hoc symmetrization rules are used, the spurious state, whose probability density is quite irregular, appears in the spectrum. Its probability density is shown in Fig. 2.5(b).

While it was demonstrated that the BF Hamiltonian is immune to spurious solutions appearance [158], the examples have been found where even the BF Hamiltonian fails to remove the spurious solutions from the electronic structure [191]. Thus, one may deduce that improper modelling of abrupt heterojunctions is not the only origin of the spurious states. The other cause of the spurious states appearance is the unphysical bowing of the bands calculated by $\mathbf{k} \cdot \mathbf{p}$ model [166, 189, 191]. It is a consequence of the inherent failure

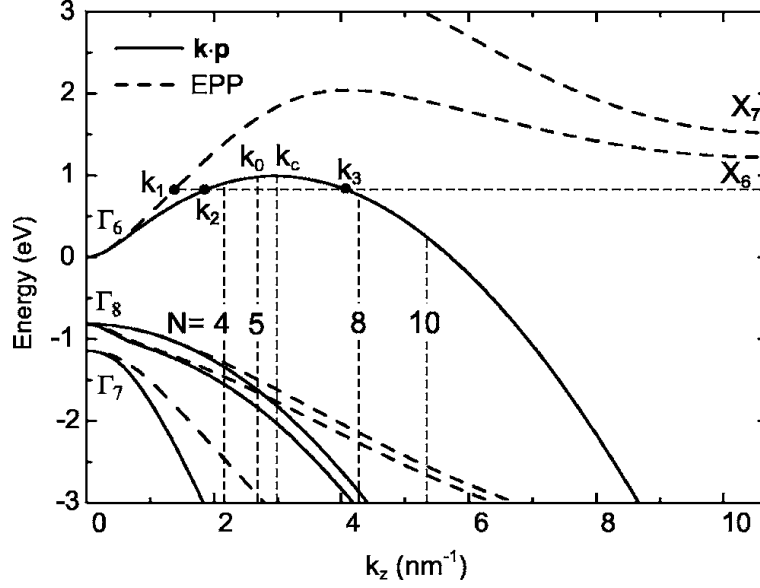


Figure 2.6: The dispersions of the electron and hole bands in (In,Ga)As along the [001] direction. Solid and dashed lines show the results of the eight-band $\mathbf{k} \cdot \mathbf{p}$ model and the empirical pseudopotential method, respectively (from Ref. [189]).

of the $\mathbf{k} \cdot \mathbf{p}$ theory to accurately model states in the whole Brillouin zone. Moreover, the conduction band dispersion relation in InAs computed by the 8-band theory exhibits non-physical bowing toward the band gap [189], as Fig. 2.6 shows. It differs from the results of the empirical pseudopotential method. Hence, when the 8-band model is employed to compute the subbands in the InAs/GaAs quantum wells, spurious solutions emerge in both the conduction band and the bandgap.

In order to control the spurious solutions appearance in the energy spectrum, the so-called *cut-off method* was proposed in Ref. [189]. It employed the expansion in a basis whose spectrum is restricted to the range from 0 to k_c where the conduction band dispersion has positive slope (see Fig. 2.6). The real-space numerical methods, such as the finite-difference and the finite-element methods, cannot be straightforwardly employed together with the cut-off method [166]. Rather, the bases of plane waves [159] or standing waves [133, 166, 189] could be used. A simpler way to remove the spurious solutions is to alter the value of the Kane parameter, which corrects the dispersion relations by removing the spurious penetration of the conduction or valence band dispersion relations into the band gap [190]. However, such a modification of the Kane parameter considerably affects the accuracy of the regular states calculation.

The additional cause of the spurious states is the loss of ellipticity of the Hamiltonian [192, 193]. Veprek et al. [192] showed that the Burt-Foreman ordering in the 4-band, 6-band, and 8-band models leads to near-elliptic envelope equations, whereas the symmetrized ordering leads to strong nonellipticity. The 8-band model is also found to suffer from the spurious solutions originating from the renormalization of the Luttinger parameters [169]. Veprek et al. derived criteria which should be satisfied by the band parameters, such as the momentum matrix elements and the Luttinger parameters, to preserve the ellipticity. Nonetheless, The most direct approach to eliminate them from the 8-band Hamiltonian is to decrease the Kane energy E_P [190, 192].

Chapter 3

The electronic structure of silicon quantum wells

In this Chapter, we study the electronic structure of silicon quantum wells by the 30-band $\mathbf{k} \cdot \mathbf{p}$ model [25]. We consider Si/SiO₂ quantum wells grown along the [001] direction. Because the conduction and valence-band offsets are quite large, the electrons and holes are mainly confined in the silicon layer. Therefore, an infinite potential well confinement (hard wall potential) was assumed, and basis of standing waves was used. The conduction-band states of this quantum well have recently been considered by the approximate effective two-band model [133]. The values of the parameters were taken from Ref. [25] (see the Appendix), where the dispersion relations of the bulk bands in the whole first Brillouin zone (FBZ) were fitted to the results of ab initio calculations. However, the symmetry between the FBZ and the second Brillouin zone (SBZ) was not established in this fitting procedure. Therefore, spurious solutions are found in the energy spectrum. We explore their origin, and moreover formulate a procedure which removes them from the energy spectrum of the analyzed quantum well. Also, the stability of some of the solutions with respect to variation of the order of the basis is discussed. Moreover, to explore in more detail how the specific boundary conditions affect the solutions, we supplement the analysis for the case of the finite band offset between Si and SiO₂. In all our results, the top of the silicon bulk valence band is taken as the zero of energy.

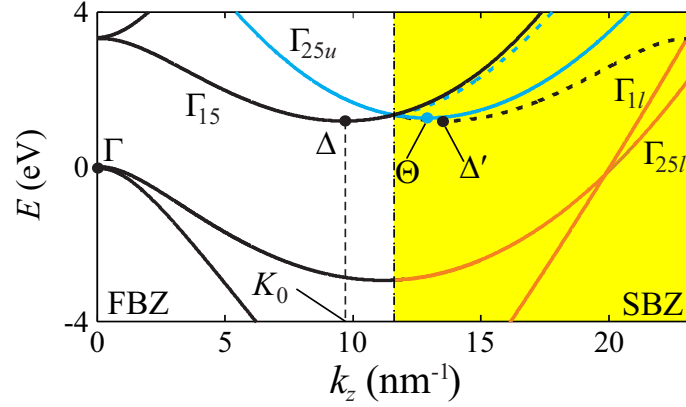


Figure 3.1: The bulk band structure of silicon along the [001] direction. The vertical dotted-dashed line is the boundary of the first Brillouin zone. The extra valley which arises from the Γ_{25u} band is denoted by Θ , and the dashed curves denote the energy bands with the proper symmetry.

3.1 The bulk band structure of silicon

Before presenting the results of our calculations for the modeled silicon quantum well, we briefly discuss the silicon bulk band structure, as computed by the 30-band $\mathbf{k} \cdot \mathbf{p}$ model given by Eq. (2.41). The dispersion relations of a few bands with energies close to the band gap in the whole FBZ and SBZ along the [001] direction are displayed in Fig. 3.1. The highest energy states in the valence band are localized close to the Γ point of the FBZ (the Γ valley), whereas the conduction band states have their energy minimum at $k_z = K_0$, which is close to the X point of the FBZ (the Δ valley). The parameters of the model were fitted such that they reproduce well the dispersion relations in the full FBZ [25]. However, such a parametrization fails to produce the correct symmetry of the bands with respect to the FBZ boundary, as demonstrated by the solid lines in Fig. 3.1. For k_z beyond the X point the dispersion relations of all bands should be mirror symmetric to the dispersion relations left of the X point, like the ones shown by the dashed lines in Fig. 3.1. More specifically, a valley labeled by Δ' in Fig. 3.1 should appear in the ground conduction band in the SBZ. However, this important detail is missing in the 30-band model. Rather, the energy of this band steeply increases with k_z in the SBZ, and instead of the Δ' valley there exists a valley of an upper conduction band, labeled by Θ in Fig. 3.1, which is just 80 meV above the Δ valley. Also, it is located close to the FBZ boundary,

therefore it can have an important contribution to low-energy conduction band states in the quantum well. Note that the symmetries of the two bands differ: the ground conduction band has mainly the Γ_{15} zone-center symmetry, whereas the upper conduction band has the combined $\Gamma_{25u} + \Gamma_{2l}$ symmetry.

In addition, due to the lack of the symmetry of the conduction bands, the valence-band dispersion relations enter the band gap for large wave vectors, which is also shown in Fig. 3.1. Consequently, for a given energy $E < 0$, there exists an additional wave vector outside the FBZ. It was demonstrated that for quantum wells based on direct band gap semiconductors and using the 8-band $\mathbf{k} \cdot \mathbf{p}$ Hamiltonian these high- k bulk states which are degenerate with the low- k bulk states produce spurious states in semiconductor quantum wells [189]. As we will see, the incorrect dispersions of the energy bands shown in Fig. 3.1 will have severe effects on the numerical calculations of the quantum well states.

3.2 The quantum well states

For the hard wall confinement potential, the quantum well states are obtained by solving the equation

$$H_{30}\Xi = E\Xi. \quad (3.1)$$

Here, H_{30} denotes the 30-band $\mathbf{k} \cdot \mathbf{p}$ Hamiltonian (see Eq. (2.41)), and Ξ is the 30-band envelope-function spinor

$$\Xi = \left[\chi_1(z), \chi_2(z), \dots, \chi_{30}(z) \right]. \quad (3.2)$$

$\chi_j(z)$ denotes an envelope function of the zone-center periodic part of the Bloch function $u_j(\mathbf{r})$ [25]. The full wavefunction of the electron in the quantum well reads

$$\eta_{k_x, k_y}(\mathbf{r}) = \exp[i(k_x x + k_y y)] \sum_{j=1}^{30} \chi_j(z) u_j(\mathbf{r}). \quad (3.3)$$

In order to satisfy the Dirichlet boundary conditions, a basis of standing waves is chosen [124, 165]. Furthermore, for the conduction band the range of wave vectors of the

basis states is conveniently centered at $k_z = K_0$ (see Fig. 3.1) [165]

$$\chi_j(z) = \exp(iK_0z) \sqrt{\frac{2}{W}} \sum_{m=1}^N c_m^{(j)} \sin(m\pi z/W). \quad (3.4)$$

Here, N denotes the order of the basis and W is the well (simulation box) width. We note that the conduction band of silicon has two minima along the [001] direction, which occur at K_0 and $-K_0$. This leads to a double degeneracy, which along with spin gives rise to four-fold degenerate states in the silicon quantum wells. A valley splitting phenomenon breaks this degeneracy [9, 133], but this is a small effect due to both inversion symmetry of the confining potential and the large separation between the equivalent Δ valleys at K_0 and $-K_0$ points. Therefore, it is discarded in our calculations.

The dominant component of the envelope function spinor $\chi_d = \chi_j$ is determined according to the criterion that it has the largest $C_j = \langle \chi_j | \chi_j \rangle$ out of 30 envelope functions which are the solutions of Eq. (3.1).

3.3 The origin of spurious states

The obtained spectra for quantum wells with thicknesses of $W = 2$ nm and $W = 5$ nm are shown in Figs. 3.2(a) and (b), respectively. To obtain these results, the order of the basis N in Eq. (3.4) is chosen such that the ground state energy is converged up to an accuracy of 1 meV. We found $N = 7$ satisfies the convergence criteria. However, this leads to the presence of basis states outside the FBZ and inside the SBZ. For the conduction-band states (cb 's) in the $W = 2$ nm wide quantum well, out of the 7 basis functions, just a single basis state belongs to the FBZ. It is a cumbersome detail related to the small separation of the Δ valley from the X point. Furthermore, the Γ_{15} states around the Δ point are expected to mostly contribute to the low energy conduction-band states in the quantum well. However, the extra Θ valley is close in energy to the Δ valley, hence some quantum-well states will be mainly $\Gamma_{25u} + \Gamma_{2l}$ like. Not all the states shown in Figs. 3.2(a) and (b) are physically relevant solutions, i.e. some spurious states are found in the energy spectrum. These states are denoted by dashed lines, and are classified into two types, as explained below.

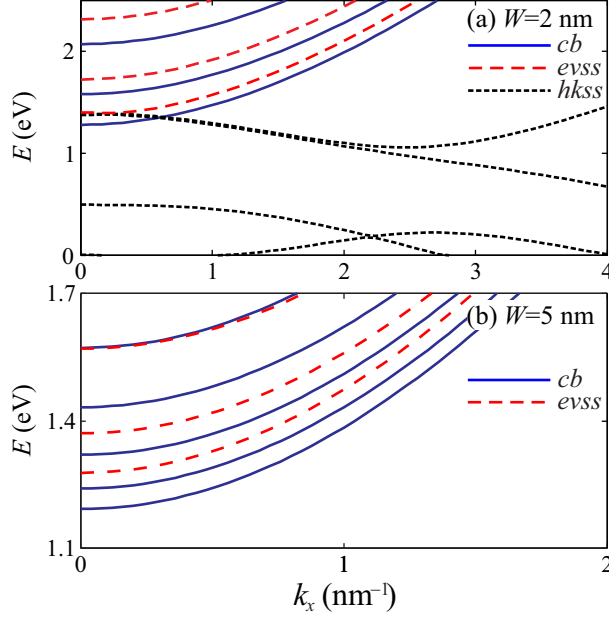


Figure 3.2: The dispersion relations of the subbands above the valence band top for the: (a) $W = 2$ nm, (b) $W = 5$ nm wide silicon quantum well. The solid lines denote the regular subbands, whereas the dashed lines denote the spurious solutions. The basis size is $N = 7$.

Next we look at the localization of the electron in a few states of the $W = 5$ nm wide quantum well for $k_x = k_y = 0$ as shown in Fig. 3.3. In order to find both types of spurious solutions in the energy spectrum, we increased the basis size to $N = 15$. The probability density of these states are displayed in the left panel (Figs. 3.3(a)-(c)), whereas the right panel (Figs. 3.3(d)-(f)) shows $\tilde{\chi}_d(z) = \chi_d(z) / \exp(iK_0z)$. The probability density of the cb ground state and the dominant envelope function shown in Figs. 3.3(a) and (d) resemble those of the ground state of the infinite rectangular quantum well according to the single-band model. It implies that the dominant contribution to the cb ground state arises from the bulk states whose wave vectors are around the K_0 point.

On the other hand, the spurious solution with an energy of 453 meV has highly oscillatory both the probability density and the dominant envelope function, as depicted in Figs. 3.3(b) and (e), respectively. The dominant envelope function is almost regularly periodic, with a period of 0.7 nm, therefore it is mainly composed of the bulk state with the wave vector $k_z = 2\pi / (0.7 \text{ nm}) + K_0 \approx 18 \text{ nm}^{-1}$. Such a high- k value is outside the FBZ, where the 30-band model was previously demonstrated to fail. Therefore, such states are named *high- k spurious solutions*, and are abbreviated by *hkss*'s (denoted by the short

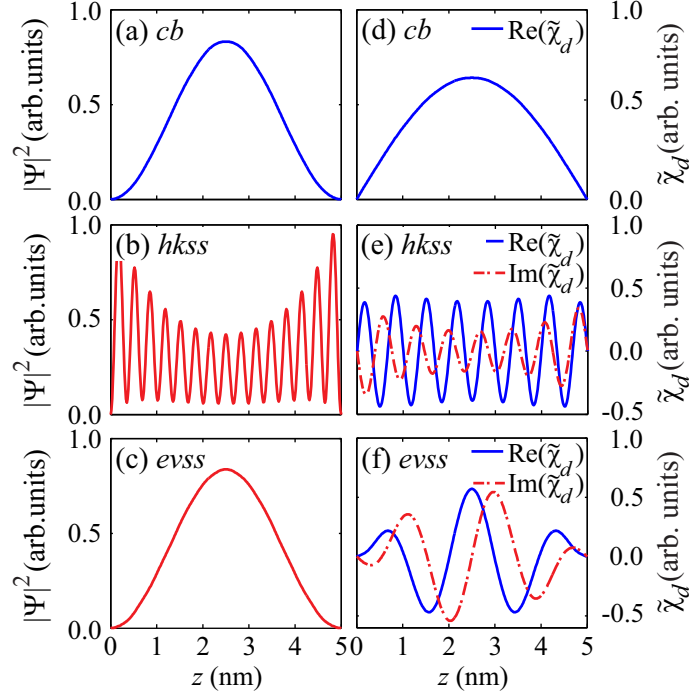


Figure 3.3: (Left panel) The probability density as function of z for a few states in the silicon quantum well of width $W = 5$ nm: (a) the conduction-band ground state (cb), with energy $E = 1193$ meV; (b) the high- k spurious solution ($hkss$) with energy $E = 453$ meV, (c) the extra-valley spurious solution ($evss$), whose energy equals $E = 1275$ meV. (Right panel) The dominant components of the envelope function spinors of the states shown in the left panel are divided by $\exp(iK_0z)$: (d) cb , (e) $hkss$, and (f) $evss$. The imaginary part in the cb state is 2 orders of magnitude smaller than the real part. The basis size is $N = 15$.

dashed lines in Fig. 3.2). They are found in both the conduction and valence bands.

Figs. 3.3(c) and (f) display the state, whose energy is 1275 meV, which looks in between the cb and $hkss$ states shown in Fig. 3.3. As a matter of fact, its probability density shown in Fig. 3.3(c) resembles the cb ground state shown in Figs. 3.3(a) and (d), and therefore could solely indicate that the state is a regular one. However, the dominant component of the envelope function spinor, shown in Fig. 3.3(f), is more oscillatory than $\tilde{\chi}_d$ displayed in Fig. 3.3(d). Yet, these oscillations are less regular and of the larger period than for the $hkss$ state (compare Figs. 3.3(e) and (f)). Nevertheless, they are composed of the wave vectors outside the FBZ ($k_z = 2\pi/(1.7 \text{ nm}) + K_0 \approx 13 \text{ nm}^{-1}$), and are mainly contributed by the bulk states of the Θ valley. Therefore, such states are spurious, but of another type, which is named extra-valley spurious solution ($evss$). They are denoted by the long dashed lines in Fig. 3.2, and are found in only the conduction band.

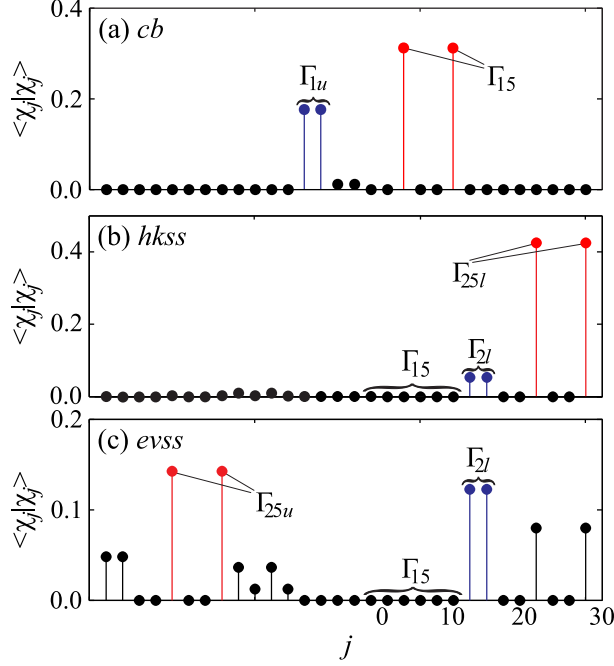


Figure 3.4: The envelope function spinor dominant component of the states shown in Fig. 3.3: (a) *cb*, (b) *hkss*, and (c) *evss*.

In order to illustrate further the origin of the states displayed in Fig. 3.3, we show in Fig. 3.4 the corresponding distributions of the probability over the different components of the envelope function spinor $\langle \chi_j | \chi_j \rangle$. Fig. 3.4(a) shows $\langle \chi_j | \chi_j \rangle$'s for the electron ground state and demonstrates that this state is mainly composed of the Γ_{15} zone-center states. However, it has a large contribution from the Γ_{1u} band [25]. This result is consistent with the approximate 2-band model proposed in Ref. [133]. On the other hand, the main contribution to the *hkss* of Fig. 3.3(b) comes from the Γ_{25l} states, as shown in Fig. 3.4(b), and the largest $\langle \chi_j | \chi_j \rangle$ in the *evss* displayed in Fig. 3.3(c) belongs to the Γ_{25u} and Γ_{2l} bands, as Fig. 3.4(c) shows. The latter two bands mainly form the Θ valley just outside the FBZ (see Fig. 3.1), which is an artefact in the SBZ, thus such states are classified as spurious.

3.4 The spurious solutions removal

We developed a scheme to automatically remove both types of spurious solutions. It is based on the following observations. In addition to contributions of different zone-center

states to quantum-well states, which were illustrated in Fig. 3.4, the absolute value of the expansion coefficients $|c_m^{(j)}|$ is found to be an important figure of merit for classifying quantum-well states as regular and spurious ones. We checked the distributions of $\langle \chi_j | \chi_j \rangle$ over j , and $|c_m^{(j)}|$ over both j and m , and were able to formulate the set of empirical rules for extracting a few (3 to 5) low-energy spurious solutions from the *conduction-band* spectrum of the quantum well. The regular states in the conduction band are found to mainly originate from the Γ_{15} band. We label the regular conduction-band states by the counter n . Furthermore, $\chi_{\Gamma_{15}}$ envelope functions were found to be mostly composed of the low m basis states. For example, the electron ground state for the range from $W = 2$ nm to $W = 20$ nm is found to be mainly composed of the $m = 1$ basis function. Furthermore, the m values of the expansion coefficients with the largest magnitude in the conduction-band states n and $n + 1$ are found to differ by not more than unity. Also, the quantum-well states whose dominant envelope function χ_d is due to bulk states different from Γ_{15} are found to be dominantly composed of the basis functions with wave vectors outside the FBZ. Therefore, they are spurious in origin, and may be of the *hkss* or *evss* type.

The proposed *modus operandi* is as follows. The calculation starts by choosing the value of the order of the computational basis N to achieve a reasonable energy accuracy, as previously explained. The Hamiltonian is then diagonalized and the envelope functions with the largest $\langle \chi_j | \chi_j \rangle$ are selected for all the computed states. The index of the dominant envelope function is labeled by j_{max} . Furthermore, for the determined j_{max} , the largest expansion coefficient $|c_m^{(j_{max})}|$ is found and is labeled by $m = m_{max}$. The m_{max} value will be compared with \tilde{m} , which is the reference value of m_{max} , and is set to unity when the procedure starts. The procedure for eliminating the spurious solutions from the spectrum of the conduction-band states reads:

1. Set the reference value of the maximal index of the dominant basis function to $\tilde{m} = 1$; set the number of the regular states to $n = 0$.
2. The composition of all the states from zero energy onward is determined; a state with the largest contribution of the Γ_{15} band is selected for further consideration;
3. For the selected state, $c_{m_{max}}^{(j_{max})}$ is determined.
4. If $m_{max} > \tilde{m}$ the state is classified as spurious.

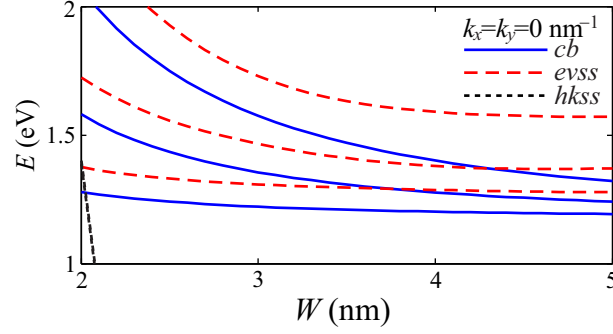


Figure 3.5: The dependence of the regular energy levels (solid lines), $evss$'s (long dashed lines) and $hkss$'s (short dashed lines) for $k_x = k_y = 0$ on the quantum-well width for $N = 7$ basis size.

5. If $m_{max} = \tilde{m}$, increase \tilde{m} by one, i.e. $\tilde{m} = \tilde{m} + 1$; such a state is classified as regular, thus $n = n + 1$.
6. If $m_{max} < \tilde{m}$, the state is classified as a regular state, and therefore $n = n + 1$.
7. Go back to step 2 to proceed with checking the other states.

Note that no regular state is misclassified by this procedure. In other words, we found that the states which do not have the dominant Γ_{15} component are dominated by standing waves with wave vectors outside the FBZ. However, the proposed procedure may be applied to remove only a few lowest energy spurious states, which is 3 to 5 for W ranging from 2 to 5 nm. Mixing between the Γ_{15} and $\Gamma_{25u} + \Gamma_{2l}$ zone-center states, which form the Δ and Θ valleys, respectively, becomes larger when the electron energy increases, and the explained algorithm cannot be adopted. Furthermore, the proposed algorithm cannot be applied to thin quantum wells, and $W = 2$ nm was found to be a practical lower limit. For quantum wells thinner than approximately 2 nm convergence of the electron energy to within 1 meV is not reachable.

Both the $hkss$'s and $evss$'s are found to exist in the range of W from 2 to 5 nm for chosen basis size. When W increases, the $evss$ energies cross the energies of the regular states, as shown in Fig. 3.5. Similar to Fig. 3.3, the $(k_x, k_y) = (0, 0)$ states are shown in this figure. The number of the regular states whose energies are lower than the lowest-energy $evss$ increases with W . Therefore, when W tends to infinity, which is the bulk silicon case, all the regular states will be below all $evss$'s. In the energy range displayed in Fig. 3.5

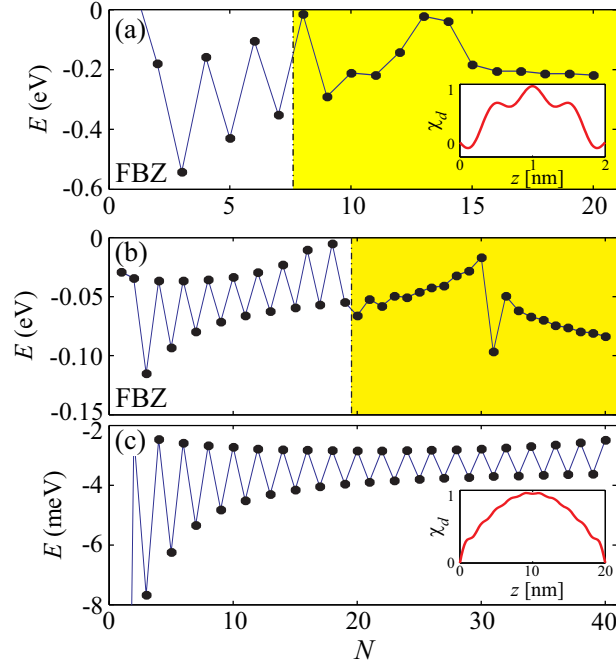


Figure 3.6: The hole ground state energy as function of the basis size N for: (a) $W = 2$ nm, (b) $W = 5$ nm, (c) and $W = 20$ nm. The yellow colour displays the area outside the FBZ. Insets show the dominant component of the hole ground state envelope function spinor.

only two $hkss$'s are above the ground conduction-band states for $W = 2$ nm, and their energies sharply decrease with W , such that already for $W = 2.1$ nm these $hkss$'s enter the band gap, where they can be easily recognized and removed from the energy spectrum.

As discussed, Fig. 3.2(a) shows the dispersion relations of the subbands which have energies close to the conduction-band bottom in the 2 nm wide well. Because of band folding the minimum of the conduction band is at $k_x = k_y = 0$. Some spurious solutions are evidently found in the bandgap, and all of them are of the high- k type, and are therefore easily removed. On the other hand, a few $evss$'s are found in the conduction band, whose dispersion relations appear to be similar to the dispersion relations of the regular states. It is because $evss$'s are formed out of the states of the Θ valley, which is similar to the real conduction band states which mainly arise from the states of the Δ valley. In other words, the bulk states of both the real states and the $evss$'s do not exhibit appreciable band mixing.

3.5 The hole states

Let us now consider the hole states. The presented procedure can also be adopted to remove the spurious solutions in the energy range of the valence-band, except that the real valence-band states are found to be mainly composed of the Γ_{25l} zone-center states. But, in addition to the spurious solutions, the hole states in the silicon quantum well suffer from an instability in the calculation with respect to the basis order, as Fig. 3.6 demonstrates. Notice that the hole ground state energy level oscillates with the size of the basis. The amplitude of the oscillations can be as large as 100 meV, and its value decreases when the well width increases, as Figs. 3.6(a), (b), and (c) show for $W = 2, 5,$ and 20 nm, respectively.

These zigzag shaped convergence can be explained as follows. First note that the diagonal elements of the 30-band Hamiltonian are equal to the kinetic energy term for a free electron. Therefore, without band mixing, the dispersion relations of all bands in silicon are concave. The curvature of the valence band alters sign through the band mixing. The analyzed silicon quantum well is symmetric, and for $k_x = k_y = 0$ the envelope functions are strictly classified with respect to inversion of the z coordinate as even or odd. The dominant component of the hole ground state is even, therefore it is composed of the $m = 1, 3, 5, \dots$ basis states. These basis states are dominantly coupled with the odd ($m = 2, 4, 6, \dots$) basis functions by the off-diagonal terms which are proportional to k_z . It is obvious from the form of the 30-band Hamiltonian given in Eq. (2.41) that the finite overlap between the even and odd envelope-function spinor components leads to a change of the sign of curvature of the subband dispersion relation.

To further illustrate the zigzag variation of the hole eigenstates observed in Fig. 3.6, we focus on a result obtained with a basis of size N and one with size $N + 1$, where N is an odd number. The extra basis function in the $N + 1$ basis is an odd function. Because the slope of this $(N + 1)$ th basis function is largest close to the boundary, where the oscillatory N th basis function reaches its maximum, the value of the matrix element between the two states can be large, and therefore can substantially modify the eigenenergy value. For odd N the basis is in fact not effective in establishing the appropriate curvature of the quantum-well subbands. Also, the dominant envelope function in the spinor of the ground

hole state has extra zeros close to the well boundary, as the inset in Fig. 3.6(a) shows for $N = 7$ and the $W = 2$ nm quantum well. However, if N is an even number, the dominant envelope function of the ground hole state becomes less oscillatory, and the extra zeros of the envelope function do not exist, as the inset in Fig. 3.6(c) demonstrate for $N = 20$ and the $W = 20$ nm wide quantum well.

The demonstrated instability of the valence-band solutions with the size of the basis is essentially a consequence of the inappropriate curvature of the hole states as modeled by the diagonal terms of the 30-band model. Such problems do not exist in the 6-band model, where the sign of curvature of the valence band dispersion relation is appropriate even if modeled by only the diagonal terms. The problem cannot be solved by increasing the size of the basis, i.e. by taking into account states outside the FBZ as shown in Figs. 3.6(a) and (b). In fact it arises from the need of the envelope function to drop exactly to zero at the boundary.

3.6 The case of the finite band offset

In order to explore how the assumption of the infinite barrier affects the stability of the hole states calculations, we extend our analysis to the case of a finite-depth Si/SiO₂ quantum well. The valence-band offset in Si/SiO₂ systems has been found to amount to 4.5 eV [194, 195]. Since SiO₂ surrounding Si layer is usually amorphous, no values for the parameters of the 30-band model could be extracted. Therefore, they are assumed to be equal to the parameters of silicon, except for the value of the band gap at the Γ point which equals 8.9 eV [194, 196]. In these calculations we assume that the Si well of width W is centrally positioned with respect to the simulation box, whose width is denoted by L . The expansion is the same as in Eq. (3.4), where W is replaced by L , and $K_0 = 0$. As an example, we assume that the Si well is $W = 5$ nm wide, and choose $k_x = 0$ nm⁻¹ and $k_y = 0$ nm⁻¹.

The obtained eight highest hole energy levels for $L = 15$ nm and $L = 10$ nm as function of the basis order N are shown in Figs. 3.7(a) and (b), respectively. Quite interestingly, the oscillations previously found for the case of the infinite quantum well do not take place when the valence-band offset is finite. For both values of W , the results improve

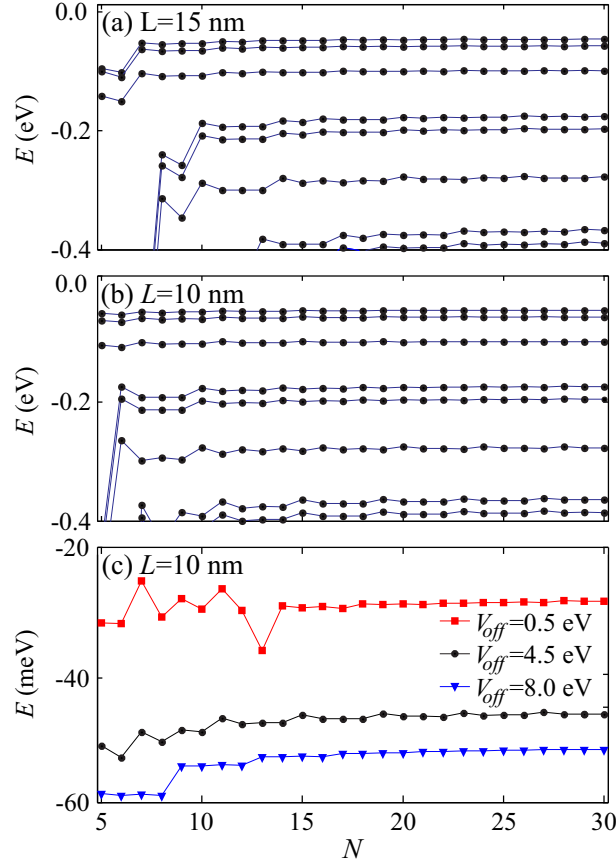


Figure 3.7: A few hole states in the $W = 5$ nm wide quantum well of finite depth as function of the basis size N for (a) $L = 15$ nm, and (b) $L = 10$ nm. (c) Convergence of the hole energy levels with N for three values of the valence-band offset.

by increasing N , and as expected, the smallest basis is needed to compute the ground state. Further, no big change is observed when the size of the simulation box decreases from $L = 15$ nm to $L = 10$ nm, except that a slightly larger basis is needed when the simulation box is wider. Therefore, allowing the envelope functions to exponentially decay stabilizes the energy level dependence on N . It confirms our previous claim that the steep descends of the envelope functions near the quantum well boundaries cause numerical instabilities with the hard-wall potential shown in Fig. 3.6. Furthermore, as Fig. 3.7(c) demonstrates, when N is sufficiently large ($N \geq 14$) we found that quite reliable results are produced irrespective of the value of the valence band offset. In this figure the ground state energies in two unrealistic cases, $V_{off} = 0.5$ eV and $V_{off} = 8$ eV, are shown, along with the ground state for $V_{off} = 4.5$ eV, which was previously shown in Fig. 3.7(b). This figure demonstrates that if envelope function is allowed to exponentially decay to

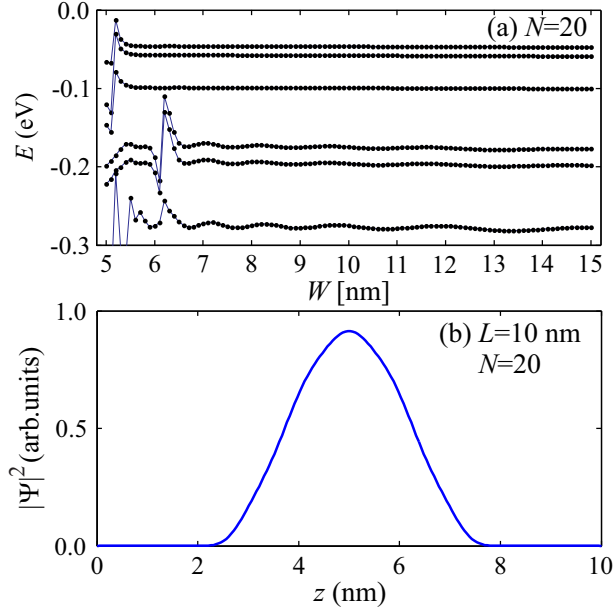


Figure 3.8: (a) The hole ground state energy in the $W = 5$ nm wide quantum well of finite depth as function of the box size for $N = 20$. (b) The probability density of the hole ground state for $L = 10$ nm and $N = 20$.

zero inside the barrier, computation of quantum well states becomes quite stable with respect to the number of basis functions. Even for a valence-band offset as large as 8 eV the convergence of the hole ground state energy level towards the numerically exact value is found to be quite steady and only $N = 13$ basis states are needed to produce the energy value with a negligible error.

The value of the valence-band offset $V_{off} = 4.5$ eV is large such that the envelope functions decay fast in the barrier. Hence, the energy of the hole ground state is almost constant for $L > 6$ nm, as Fig. 3.8(a) shows for $N = 20$. The energies of the other states depend similarly on L . However, some of them clearly exhibit oscillations. The reason is as follows. Since lower states of the valence band are more oscillatory, we need a broader k -interval than for the ground state to accurately describe them. With increasing box size (and fixed basis size N) we narrow the covered k -space (since $k \sim 1/L$), so these low states are not described accurately. Nevertheless, we need a wider box for these states than for the ground state. When the difference between W and L is not large, the confining potential is like in the infinite quantum well. Consequently, the results for the highest energy states become quite unstable when N varies, as Fig. 3.6 previously showed.

Fig. 3.8(a) indicates that if one is interested in computing only three highest energy states, even the choice $L = 6$ nm produces a good result. Varying width and depth of the quantum well might modify this finding, and could depend on the values of the material parameters. But Fig. 3.8(b) shows that the probability density of the hole ground state is quite confined inside the well (which ranges between $2.5 \text{ nm} \leq z \leq 7.5 \text{ nm}$). It accounts for why the energy of the ground state in Fig. 3.8(a) does not vary much for $L > 6$ nm. Moreover, we found that even for a small barrier width the highest energy states can be quite accurately computed, and the accuracy of the calculation of the lower energy states can be improved by increasing the basis order. Hence, thin silicon layers embedded between thick barriers can be accurately modeled by the employed 30-band theory, providing the width of the simulation box and the basis size is large enough. We note that for finite band offsets Richard et al. previously employed 40 basis functions in the 30 nm wide box to compute the hole states in the Ge/SiGe quantum well with 1 meV accuracy [165].

Chapter 4

Interband optical transitions in silicon quantum wells

In this Chapter, we model the interband optical transitions in Si/SiO₂ quantum wells which are grown in the [001] direction. The transition energies, the interband transition matrix elements (IBTM's) and the absorption spectra are computed as function of the quantum well width. The evolution from an indirect to a direct gap material when the width of the well decreases is investigated. As in previous section, we assume the hard-wall confinement, since the conduction and valence band offsets are both larger than 3 eV [194].

4.1 Theoretical model

The electron states are extracted from the 30-band model (see Eq. 2.41) using the standing-wave expansion (see Eq. 3.4). The wavevector is 30-component spinor given by Eq. 3.2. As stated, the basis for conduction-band computation is centered at K_0 , where K_0 is the location of the conduction band minimum (Δ valley) along the k_z direction in the first Brillouin zone, i.e. $\mathbf{K}_0 = (0, 0, K_0)$. The spurious solutions are removed by the algorithm explained in Section 3.

The hole states are calculated by means of the 6-band $\mathbf{k}\cdot\mathbf{p}$ theory (See Eq. (2.33)). Eigenvectors are six-component envelope-function spinors $\Xi^{(6)}$. Because the valence-band maximum is located at the Γ point, the envelope functions in the 6-band model are

expanded similar to Eq. (3.4) [124, 146], but with $K_0 \equiv 0$. Furthermore, for a calculation of the interband transition matrix elements it is convenient to represent the six-band spinor of the hole states in the thirty-band form

$$\Xi_h^{(30)} = \left[0, 0, \dots, \chi_1^{(6)}, \chi_2^{(6)}, \chi_3^{(6)}, \chi_4^{(6)}, \chi_5^{(6)}, \chi_6^{(6)} \right]. \quad (4.1)$$

Here, the positions of the hole envelope functions correspond to the order of the zone-center states as in Ref. [25].

The IBTM between the subband n_h in the valence band and the subband m_e in the conduction band reads

$$\begin{aligned} M_{n_h m_e}(k_x, k_y) &= \langle n_h, k_x, k_y | p_x | m_e, k_x, k_y \rangle \\ &= \hbar k_x \sum_{j=1}^{30} \langle \chi_{j, n_h} | \chi_{j, m_e} \rangle \\ &\quad + \sum_{j=1}^{30} \sum_{i \neq j} \langle \chi_j^{n_h} | \chi_i^{m_e} \rangle \langle u_j | p_x | u_i \rangle. \end{aligned} \quad (4.2)$$

Here, light is assumed to be polarized along the x -direction, and the dependence of the matrix elements on the in-plane wave number $k_{\parallel} = (k_x, k_y)$ is explicitly indicated. The absorption coefficient is given by [197]

$$\begin{aligned} \alpha(\hbar\omega) &= \frac{e}{n_r c \epsilon_0 W} \frac{1}{\hbar\omega} \sum_{n_h} \sum_{m_e} \int_{(k_x)} \int_{(k_y)} |M_{n_h m_e}(k_x, k_y)|^2 \\ &\quad \times \frac{\Gamma/2\pi}{\Delta E_{nm}^2 + (\Gamma/2)^2} dk_x dk_y, \end{aligned} \quad (4.3)$$

where $\Delta E_{nm} = E_{m_e} - E_{n_h}$ is the transition energy, n_r denotes the refractive index of silicon, and Γ is the full width at half maximum (FWHM) of the Lorentzian which describes the broadening of the energy levels.

4.2 Interband transition energies

The values of the band-structure parameters are taken from Ref. [25]. The refractive index and the broadening parameter are assumed to be equal to $n_r = 3.5$ [198] and $\Gamma = 5$ meV [34], respectively. The basis of order $N = 7$ is used when calculating both the conduction

and valence band states. For such a choice, the electron ground state is computed with an error less than 1 meV [166]. The optical absorption is obtained by taking into account all the transitions with $\Delta E_{nm} \leq 2.1$ eV, for quantum well width W varying in the range from 2 nm to 5 nm. For $W < 2$ nm the accuracy of 1 meV is difficult to attain [166]. The demonstrated indirect-to-direct band gap transition affects the exciton spectra if the quantum-well thickness is comparable to or less than the exciton Bohr radius, which is about 5 nm in silicon [55]. The top of the silicon valence band is taken as the zero of energy.

The energy spectrum of the conduction subbands along the [100] direction, shown in Figs. 4.1(a) and (b), for $W = 2$ nm and $W = 5$ nm respectively, clearly demonstrates that the energy minimum of the electron ground subband in the analyzed silicon quantum well is located at $\mathbf{k}_{\parallel} = (k_x, k_y) = 0$ (the Γ point of the 2D Brillouin zone). In bulk silicon, the six Δ valleys might be classified in pairs of Δ_x , Δ_y , and Δ_z valleys, which are located at $\mathbf{k} = (\pm K_0, 0, 0)$, $\mathbf{k} = (0, \pm K_0, 0)$, and $\mathbf{k} = (0, 0, \pm K_0)$, respectively, with $K_0 = 0.85 \frac{2\pi}{a_0}$, where a_0 is the lattice constant of bulk silicon. The quantum-well states can be expanded in the bulk Bloch states, and those with $k_x = k_y = 0$ nm⁻¹ are contributed by the bulk states of two Δ_z valleys. Hence, the Δ_z valleys effectively fold onto the Γ point of the 2D Brillouin zone [166]. Along with the spin degeneracy, the quantum states are four-fold degenerate. In reality there is also valley splitting [9], yet it is a small effect, and is therefore discarded in our model. On the other hand, the Δ_x or Δ_y valleys are separated in k space, and therefore their states are only double-spin degenerate. The energy minimum of the states originating from the Δ_x valleys is above the energy minimum of the states coming from the folded Δ_z valleys. When the well width increases, the energy difference between the two minima decreases, as can be inferred by comparing Figs. 4.1(a) and (b).

To explore in more detail the direct band gap demonstrated in Fig. 4.1, we display the interband transition energies between the valence and conduction band states at $\mathbf{k}_{\parallel} = 0$ as they vary with the well width in Fig. 4.2(a). We note that the heavy-hole band does not mix with either the light-hole and split-off bands at $k_x = k_y = 0$ nm⁻¹, therefore the hole states are classified as heavy-hole states, which are denoted by HH n (n is the quantum number of the subband) and mixed light-hole (LH) and split-off (SO) character. The latter subbands can be classified as (1) the *hole-XY* (HXY n) states, whose wave functions are

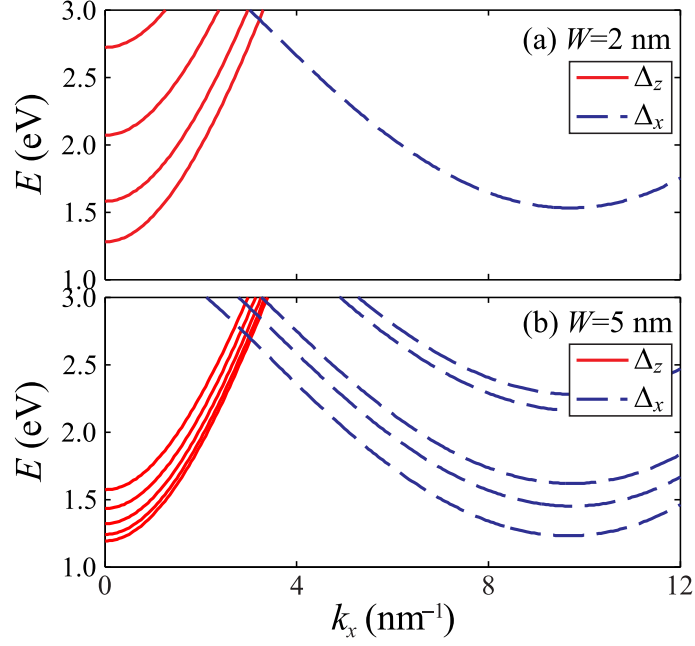


Figure 4.1: The dispersion diagrams of the conduction subbands in: (a) $W = 2$ nm, and (b) $W = 5$ nm wide silicon quantum well. The solid and dashed lines denote the subbands originating from the Δ_z and Δ_x valleys, respectively.

dominated by the $|X\rangle$ and $|Y\rangle$ zone-center states, and (2) the *hole-Z* (HZ n) states which are mainly composed of the $|Z\rangle$ zone-center functions. Hence, the interband transitions between the valence-band and the conduction-band (C) states are classified as the HH n -C m transitions, the HXY n -C m transitions, and the HZ n -C m transitions. The transition energies shown in Fig. 4.2 monotonously decrease with the quantum-well width, tending to the values in bulk silicon. For $W = 5$ nm the lowest energy of the HH1-C1 transition, which is the effective band gap, exceeds the silicon band gap by only 70 meV. But, when the well width is reduced to 2 nm, the effective band gap becomes 444 meV larger than the one of bulk silicon. The obtained $E_g(W)$ dependence qualitatively agrees with tight-binding calculations of Ref. [199].

We found that the lowest transition energy could be fitted by a power law

$$\Delta E_{min}^{(type)}(\tilde{W}) = a\tilde{W}^b + E_{Si}^{(type)}, \quad (4.4)$$

where a and b are fitting parameters, $\tilde{W} = W/u$, where $u = 1$ nm, and $E_{Si}^{(type)}$ is the value of the silicon band gap for the HH1-C1 and HXY1-C1 transitions ($E_{Si}^{(1,2)} = E_{gb}$, for $type =$

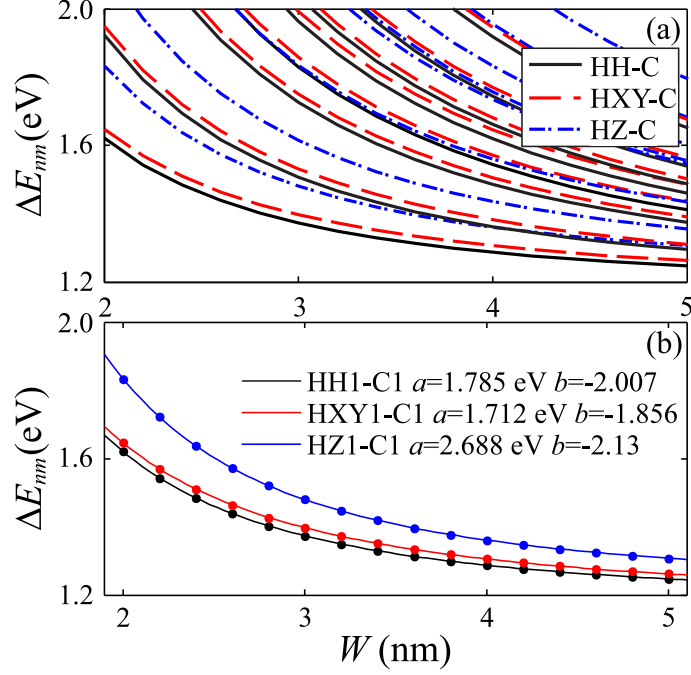


Figure 4.2: (a) Variation of the interband transition energies for $k_x = k_y = 0 \text{ nm}^{-1}$ with the quantum well width. The HH-C, HXY-C, and HZ-C transitions are denoted by solid, dashed, and dash-dot lines, respectively. (b) Fits of the computed data for the HH1-C1, HXY1-C1 and HZ1-C1 transitions with the power law function defined by Eq. (4.4).

1, 2), and equals $E_{Si} = E_{gb} + \Delta_{SO}$ for the HZ1-C1 transition ($type = 3$). For the values of $E_{gb} = 1.177$ eV and $\Delta_{SO} = 0.044$ eV taken from Ref. [25], we determine $a = 1.785$ eV and $b = -2.007$ for HH1-C1 transition. We compare the shape of the employed fitting curve in Eq. (4.4) with the result from single band effective mass theory

$$\begin{aligned}
 E_{minsb}^{(1)} &= \frac{\hbar^2 \pi^2}{2m_0 W^2} \left(\frac{1}{m_l} + (\gamma_1 - 2\gamma_2) \right) + E_g^{bulk} \\
 &= (1.776 \tilde{W}^{-2} + 1.177) \text{ eV}.
 \end{aligned} \tag{4.5}$$

Here, γ_1 and γ_2 denote the Luttinger parameters and m_l is the electron longitudinal effective mass [25]. The obtained values of the fitting parameters are surprisingly close to the values derived from the single-band model. It implies that a properly parameterized single-band approach could be used to model the lowest direct transition energy in Si/SiO₂ quantum wells. However, because of mixing between the LH and SO states, the fitting parameters for the energies of the HXY1-C1 and HZ1-C1 transitions displayed in Fig. 4.2(b) are poorly described by the single-band approach.

4.3 Interband transition matrix elements and interband absorption

As shown, Si quantum wells have a direct band gap. However, as Fig. 4.3 shows the optical transitions across this band gap become less active when the quantum well width increases. The IBTM's in the quantum well are subject to selection rules resulting from the specific symmetry of the zone-center periodic parts of the Bloch functions. We showed in Chapter 3 that the wave functions of the electron states in the conduction band are mostly composed of the $|Z\rangle$ and $|S\rangle$ zone-center periodic parts of the Bloch functions which belong to the Γ_{15} and Γ_{1u} bands, respectively. The hole states are composed of the $|X\rangle$, $|Y\rangle$ and $|Z\rangle$ zone-center periodic parts of the Bloch functions, which belong to the Γ_{25l} band. Because of such symmetry of the Bloch functions, the IBTM's are dominated by the terms proportional to $\langle Y_v | p_x | Z_c \rangle$ and $\langle X_v | p_x | S_c \rangle$, where the indices v and c denote the valence and conduction band, respectively. Figs. 4.3(a)-(c) show how the modulus squared of the IBTM's for HHn-Cm transitions at $k_x = k_y = 0 \text{ nm}^{-1}$ vary with the quantum well width. A similar oscillatory variation of the IBTM's with W was previously found from an effective two-band model in Ref. [133]. The oscillator strength as function of W calculated in Ref. [199] did also exhibit a non-monotonic behaviour.

In order to explain the oscillations shown in Fig. 4.3, we note that the IBTM's are dominated by the overlap integrals $\langle \chi_{Y_{vn}}^{(h)} | \chi_{Z_{cm}}^{(e)} \rangle$ between the envelope functions corresponding to $|Y_v\rangle$ and $|Z_c\rangle$ zone center states. If mixing between the envelope functions is discarded, $|\chi_{Y_{vn}}^{(h)}\rangle$ and $|\chi_{Z_{cm}}^{(e)}\rangle$ have the analytical forms: $\chi_{Y_{vn}}^{(h)} = \sqrt{2/W} \sin(n\pi z/W)$ and $\chi_{Z_{cm}}^{(e)} = \sqrt{2/W} \exp(iK_0 z) \sin(m\pi z/W)$. Within this approximation, the overlap integral between the n -th hole state and the m -th electron state becomes

$$\begin{aligned}
 I_{nm}(\mu) &= \langle \chi_{Y_{vn}}^{(h)} | \chi_{Z_{cm}}^{(e)} \rangle \\
 &= \frac{2}{W} \int_0^W \sin(n\pi z/W) \exp(iK_0 z) \sin(m\pi z/W) dz \\
 &= \begin{cases} \frac{4i\pi^2}{\pi\mu(\mu^2 - 4n^2)} (\exp(i\mu\pi) - 1); & n = m \\ \frac{4i\mu nm}{\pi(\mu^2 - (n-m)^2)(\mu^2 - (n+m)^2)} ((-1)^{n+m} \exp(i\mu\pi) - 1); & n \neq m \end{cases},
 \end{aligned} \tag{4.6}$$

where $\mu = K_0 W / \pi$. For $K_0 = 0$, the matrix elements are zero, i.e. the electron and hole states are orthogonal to each other, except for $n = m$, which is the well known selection rule for interband transitions in quantum wells made of direct gap semiconductors. On the other hand, for $K_0 \neq 0$, this selection rule is alleviated, allowing transitions between states of different n and m . However, when $K_0 \neq 0$, I_{nm} could be zero even for $n = m$. The latter situation appears when the terms in the parentheses of the right hand side of Eq. (4.6) are equal to zero. Thus, the following cases are resolved:

1. if $n = m$, zeroes are found for even numbers of $\mu_l = 2l$, where $l = 1, 2, \dots$, except for the case $\mu = 2n$ when $I_{nm} = -1/2$;
2. if n and m are of equal parity, zeroes in I_{nm} are found for even number of $\mu_l = 2l$, $l = 1, 2, \dots$, except for the case $\mu = n \pm m$ when $I_{nm} = \mp 1/2$;
3. if n and m are of opposite parity, zeroes in I_{nm} are found for odd numbers of $\mu_l = 2l - 1$, $l = 1, 2, \dots$, except for the case $\mu = n \pm m$ when $I_{nm} = \mp 1/2$.

The modulus squared of the IBTM for the HH1 – C1 transition and $|I_{11}|^2$ are compared in Fig. 4.3(a). The two curves almost coincide, with the most noticeable detail that the zeroes of $|I_{11}|^2$ and $|M_{11}|^2$ are close to each other. Therefore, the simple single-band approach offers an approximate and qualitatively correct view into the origin and location of the zeroes of the transition matrix elements.

The matrix elements of the higher energy optical transitions exhibit similar variation with W , as Fig. 4.3(b) shows for the HH1-C2, HH1-C3, HH2-C1 and HH2-C2 transitions, and Fig. 4.3(c) for the HH1-C4 and HH2-C3 transitions. Also, by comparing different scales for the IBTMs in Figs. 4.3(a), (b), and (c) we notice that the local maxima increase when the transition takes place between subbands with higher energies, i.e. when either n or m increases. This shows that the first transition in the well is never strong, so that the evolution from indirect to direct gap material is caused by higher energy transitions in the quantum well. For the transitions shown in Fig. 4.3(c), the maximal values of $|M_{nm}|^2$ are comparable to the values found for quantum wells based on direct semiconductors such as GaAs. The latter is approximated as $|M_{11}|^2 \approx |\langle S | p_x | X \rangle|^2 / 2 = |(m_0 P / \hbar)|^2 / 2 \approx 40 \text{ eV}^2 \text{ fs}^2 / \text{nm}^2$, where P is the Kane matrix element and the overlap integral is approximated by unity. For the analyzed quantum well, the wave functions for large n and m are formed

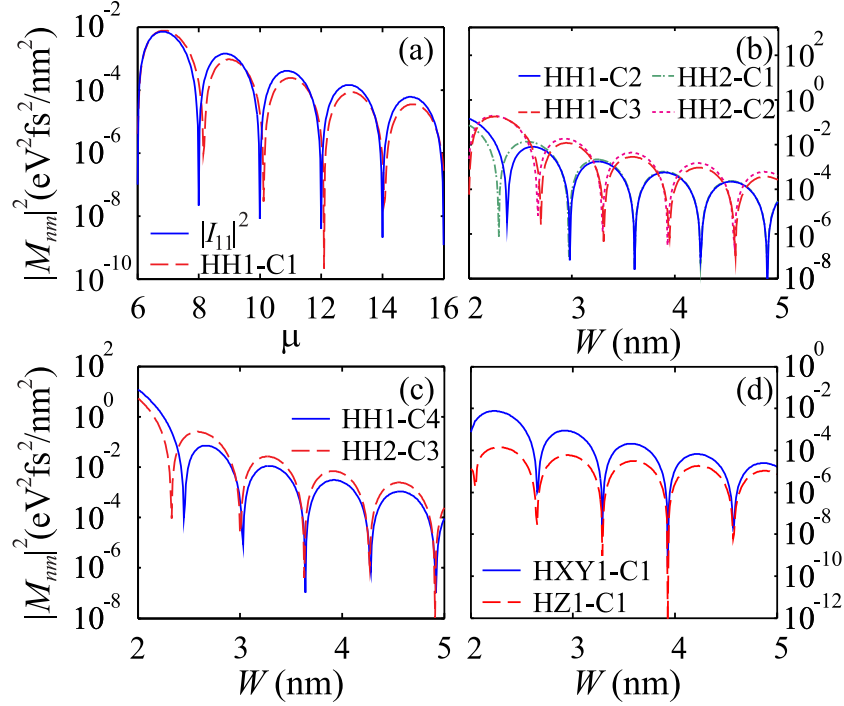


Figure 4.3: $|M_{nm}(0,0)|^2$ as function of W for: (a) the HH1-C1 transition (the approximating function $|I_{11}|^2$ multiplied by 10^{-10} is also shown), (b) the HH1-C2, HH1-C3, HH2-C1, and HH2-C2 transitions, (c) the HH1-C4 and HH2-C3 transitions, and (d) the HXY1-C1 and HZ1-C1 transitions.

out of bulk states which span a large range of the Brillouin zone, i.e. from the energy extrema in the valence and conduction bands, and therefore the overlap integrals increase with n and m .

The IBTM for the HXY1-C1 transition exhibits a similar variation with W , which is shown in Fig. 4.3(d), as $|M_{11}|^2$ shown in Fig. 4.3(a). It is a consequence of the similar compositions of the envelope function spinors of the HH1 and HXY1 states. On the other hand, the HZ states contain negligible contribution from the $|X\rangle$ and $|Y\rangle$ zone center states, therefore the matrix element squared of the HZ1-C1 transition, shown by the dashed curve in Fig. 4.3(d), is an order of magnitude smaller than the $|M_{nm}|^2$ for the HH1-C1 and HXY1-C1 transitions.

The maxima observed in Fig. 4.3(a) provide an indication how the value of the quantum well width should be selected to achieve maximum absorption. Therefore, we performed calculations of the interband absorption spectra for 2.2 nm, 2.9 nm, 3.6 nm, 4.2 nm, and 4.9 nm wide quantum wells. The absorption coefficients for these values of W

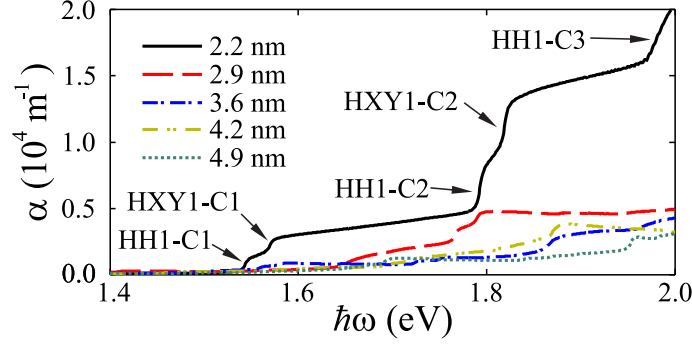


Figure 4.4: The absorption coefficient for 2.2 nm, 2.9 nm, 3.6 nm, 4.2 nm and 4.9 nm wide quantum wells. The transitions responsible for the shown steps are explicitly indicated.

are shown in Fig. 4.4. They show step-like features which correspond to the onset of the HH_n-C_m and HXY_n-C_m transitions at k_{\parallel} . As could be inferred from Fig. 4.3, a decrease of the quantum well width leads to an increase of the absorption coefficient. The optical absorption decreases by an order of magnitude when the well width increases from $W = 2.2$ nm to just $W = 4.9$ nm. Also, for certain values of the quantum well width, the absorption is significantly reduced. Such “dark spots” indicate that the analyzed silicon quantum wells should be properly designed to achieve maximum quantum efficiency in practical applications such as photonic detectors and emitters. However, also note that the obtained absorption coefficients are at least an order of magnitude smaller than for a similar direct gap material as GaAs, even for the thinnest well.

Finally, we compare our results with the available experimental data of Refs. [55] and [61], which provided evidence for a direct band gap in thin Si quantum wells embedded in SiO_2 . This evidence was provided for very thin wells of thickness less than 2 nm. However, results for the well thicknesses of 2.2 nm and 2.4 nm were also provided, for which the photoluminescence intensity was found to show a peak at 1.44 eV and 1.38 eV, respectively. We compare this with the lowest transition energies from our model which amounts to 1.54 eV for the 2.2 nm Si well and 1.48 eV for the 2.4 nm Si well. The difference of approximately 0.1 eV is a consequence of the imposed approximation of confinement by infinite barriers and the fact that we disregarded excitonic effects which will decrease the transition energy.

Chapter 5

The 30-band model of the GaAs/(Al,Ga)As quantum wells

The GaAs/(Al,Ga)As system is composed of wide band-gap semiconductors. Therefore, the common approach to model the electronic structure of GaAs/(Al,Ga)As quantum wells is to employ the single-band model for the conduction-band states and the 6-band Luttinger-Kohn model for the valence-band states. Because the inverse effective mass is multiplied by $k_{\parallel}^2 = k_x^2 + k_y^2$ in Eq. (2.9), the single-band model delivers isotropic quantum-well subbands. This isotropy is in fact a consequence of the *s*-like character of conduction-band states in bulk semiconductor. On the other hand, the zone-center states in the valence-band are *p*-like, which gives rise to a pronounced anisotropy of the heavy and light-hole bands, and is described by the 6-band Luttinger-Kohn model.

In both the single-band model and the 6-band Luttinger-Kohn model, the dispersion relations are spin degenerate. However, this degeneracy is not exact due to the lack of centrosymmetry in zinc-blende crystals, which leads to the breaking of the spin-degeneracy of the bulk states known as the *Dresselhaus effect* [200]. Hence, neither the single-band nor the 6-band model predict the Dresselhaus effect (see Chapter 2). Furthermore, the subband dispersion relations in the conduction bands of bulk semiconductors are parabolic for k much smaller than the reciprocal lattice constant. But at large k , the dispersion relations become non-parabolic [201, 202]. Due to the large mixing between the heavy-hole and light-hole subbands, the nonparabolicity of the valence subbands is even larger.

On the other hand, the symmetry of zinc-blende crystal is fully taken into account in

the 30-band model [128, 143]. Therefore, the energy splitting due to the absence of the inversion symmetry in bulk crystals, which represents the Dresselhaus effect, is reproduced by the 30-band calculations. Furthermore, because the 30-band model is a full-zone approach, it may successfully model the nonparabolicity of the conduction band. And similar to the 6-band model, the 30-band model takes into account the anisotropy of the valence band. However, the dispersion relations of the heavy and light-hole bands determined by the 6-band and 30-band models are expected to exhibit certain mutual differences, especially at large hole wave vector. Also, the 30-band model shows that the isotropy of the conduction band states is not exact (see Eq. (2.41)) and is able to predict much better the valence-band anisotropy than the 6-band model. The comparison of the 6-band LK model with higher-order $\mathbf{k} \cdot \mathbf{p}$ models has been investigated in Refs. [146] and [147] for quantum wells and quantum wires, respectively.

The single-band model provides a way for quite fast calculations of quantum-well subbands. Also, the isotropic character of the computed dispersion relations of the subbands saves time for subsequent calculations of the optical and transport properties of quantum wells. Furthermore, the single-band and 6-band models could be adopted when quantum wells are wider than approximately 2 nm, since the envelope-function approximation requires that the envelope function is slowly varying on the scale of the unit cell. On the other hand, the 30-band model does not have such a restriction.

In this Chapter we consider the symmetric GaAs/Al_{0.3}Ga_{0.7}As quantum wells, and compare different $\mathbf{k} \cdot \mathbf{p}$ models. The electron states are computed using both the single-band effective mass Schrödinger equation and the 30-band Hamiltonian (Eqs. (2.9) and (2.41)). The hole states are determined by the 6-band Luttinger-Kohn model (Eq. (2.33)) and the 30-band Hamiltonian. In all the calculations position dependence of the bulk band structure parameters is taken into account by adopting the symmetrization rules given by Eq. (2.51).

As in previous chapters, the electrons and holes are assumed to be confined along the z direction. In each of the three models the z -dependent parts of the envelope functions are expanded in standing waves

$$\psi_i(z) = \sum_{j=1}^N c_j^i \sqrt{\frac{2}{L}} \sin(j\pi z/L), \quad (5.1)$$

where N is the basis size and L is the simulation box width. The contribution of the zone-center state of the Γ band to the quantum-well state is quantified by the *band contribution parameter*, defined by

$$D_{\Gamma} = \sum_{i \in \Gamma} \langle \psi_i | \psi_i \rangle. \quad (5.2)$$

The values of the parameters of the 30-band model in GaAs and AlAs are taken from Refs. [128] and [143], respectively, and the values of the parameters for $\text{Al}_{0.3}\text{Ga}_{0.7}\text{As}$ are obtained by the linear interpolation of the data for GaAs and AlAs. The parameters of the single-band and 6-band models are obtained from the parameters of the 30-band model using the perturbation theory [128, 143]. The effective masses are $m_{\text{GaAs}}^* = 0.067m_0$ and $m_{\text{AlAs}}^* = 0.15m_0$, and the Luttinger parameters are $\gamma_1^{\text{GaAs}} = 7.18$, $\gamma_2^{\text{GaAs}} = 2.23$, $\gamma_3^{\text{GaAs}} = 2.99$, $\gamma_1^{\text{AlAs}} = 3.76$, $\gamma_2^{\text{AlAs}} = 0.82$, and $\gamma_3^{\text{AlAs}} = 1.42$.

According to Ref. [139], the valence-band offset (VBO) of the GaAs/ $\text{Al}_{0.3}\text{Ga}_{0.7}\text{As}$ system equals $V_{off}^v = -0.159$ eV. All the calculations employed the basis of $N = 30$ standing waves. The quantum well width W is varied in the range from 2 nm to 20 nm, and the dispersion relations are determined for the electron and hole wave vectors from 0 to 1 nm^{-1} , which is the range mostly determining the transport and optical properties of semiconductor quantum wells. Moreover, in the foregoing discussion we will implement a view that the envelope functions of the quantum well states are formed out of the bulk solutions of various k_z .

5.1 The electron states

5.1.1 The subband dispersion relations

The energy minima of the conduction subbands in the analyzed quantum well are located at $\mathbf{k}_{\parallel} = (k_x, k_y) = 0$. For $n = 1, 2, 3, 4$ we found that the energies of the subbands bottoms vary with quantum well width as Fig. 5.1(a) shows. From this figure it is obvious that the accuracy of the single-band calculations is the best for $n = 1$. As a matter of fact, we found that the values of E_{10} computed by the single-band and the 30-band models differ by 2 meV for $W = 2$ nm, whereas this difference decreases to approximately 0.1 meV when W equals 20 nm. The demonstrated better agreement between the two models

for low n and large W could be explained by slow variation of the envelope functions which are composed of the low k_z bulk solutions, and are quite well reproduced by the single-band calculations. When n increases, the subband envelope functions become more oscillatory, and are therefore contributed by the bulk solutions of larger k_z [166]. The latter are, however, less accurately determined by the single-band theory, and therefore the calculations become less accurate.

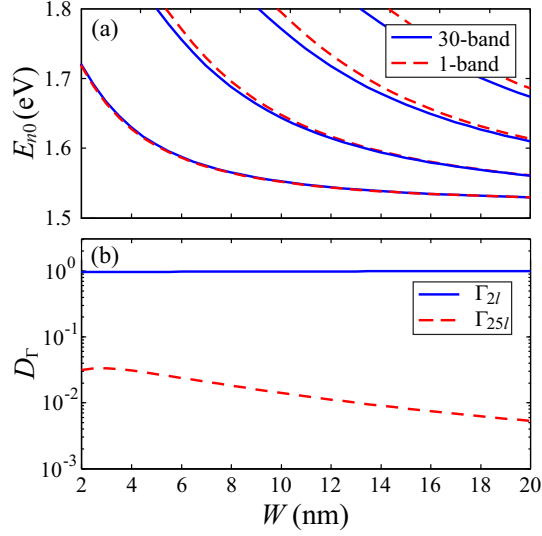


Figure 5.1: (a) The energy minima of the conduction subbands in the GaAs/(Al,Ga)As quantum well as function of the well width. The solid and dashed lines denote the results of the 30-band and the single-band calculations, respectively. (b) Variation of two largest band contribution parameters D_Γ for the ground electron state with well width.

To elucidate with more details the observed agreement between the single-band and the 30-band theory, in Fig. 5.1(b) we show how a few largest band contribution parameters for the $n = 1$ subband at $k_{\parallel} = 0$ vary with quantum well width. The $n = 1$ quantum well state is almost fully contributed by the Γ_{2l} zone-center functions, which have the s symmetry. Their contribution varies from $D_{2l} = 0.966$ for $W = 3$ nm, which is a local minimum, to $D_{2l} = 0.995$ for $W = 20$ nm, therefore it is almost constant with W . The other zone-center states contribute much less to the $n = 1$ subband, and the largest D_Γ arises from the Γ_{25l} zone-center states, which are p symmetric, and mostly contribute to the valence-band states. It therefore implies that the conduction band is mostly mixed with the valence bands in the $n = 1$ conduction subband, which explains why the 8-band model is a successful approach to improve the results of the single-band theory. The

contribution of the Γ_{25l} state is however small, and ranges from $D_{25l} = 0.033$ for $W = 3$ nm, which is a local maximum, to $D_{25l} = 0.005$ for $W = 20$ nm. The contribution of all the other bands in the 30-band model is found to be negligible, being in total smaller than 0.001. Furthermore, Fig. 5.1(b) shows that the contributions of the other bands decrease with W , therefore the single-band approach is better adopted for wider GaAs/(Al,Ga)As quantum wells.

To compare the models more closely, we show in Fig. 5.2(a) and (b) the dispersion relations of the conduction subbands in the $W = 2$ nm and $W = 10$ nm wide GaAs/(Al,Ga)As quantum wells, respectively. For $W = 2$ nm, there exists one subband in the quantum well, whereas two subbands are found for $W = 10$ nm. The difference between the energies computed by the two models obviously increases with k_{\parallel} , and the curvature of the dispersion relations computed by the single-band model is larger. This is a manifestation of the non-parabolicity which is taken into account in the 30-band model, and is present in the energy spectra of both the $W = 2$ nm and $W = 10$ nm wide quantum wells. Nevertheless, the cases $W = 2$ nm and $W = 10$ nm differ by sign of the difference between the energy minima: for $W = 2$ nm we found that E_{10} computed by the single-band model is smaller than E_{10} obtained by means of the 30-band calculations (see inset in 5.2(a)), whereas the opposite is found for $W = 10$ nm. In both the single-band and 30-band calculations, the $k_{\parallel} = 0$ state is double degenerate, whereas this degeneracy is broken for $k_{\parallel} \neq 0$ states due to the lack of bulk inversion symmetry [167]. The splitting which is obtained in the 30-band calculations is not larger than 0.5 meV. However, when k_{\parallel} is of the order 1 nm^{-1} the difference between the $n = 1$ energy levels computed by the two methods can be as large as 100 meV. Furthermore, the $n = 1$ subband dispersion relations determined by the two methods have quite similar curvatures, which is the manifestation of dominant localization of the electrons in the well for both cases shown in Fig. 5.2.

The subband dispersion relations obtained by the 30-band model are anisotropic, which is demonstrated by the different dispersion diagrams along the [10] and [11] directions. These are directions along which the dispersion relations exhibit the largest difference. The anisotropy of the subband is therefore quantified by $\Delta E_{[10]-[11]}(k_{\parallel}) = E_{[10]}(k_{\parallel}) - E_{[11]}(k_{\parallel})$. It is found to increase with k_{\parallel} , from zero at $k_{\parallel} = 0$ to about 25 meV at $k_{\parallel} = 1 \text{ nm}^{-1}$. The dispersion relation along the [10] direction is found to be shifted up-

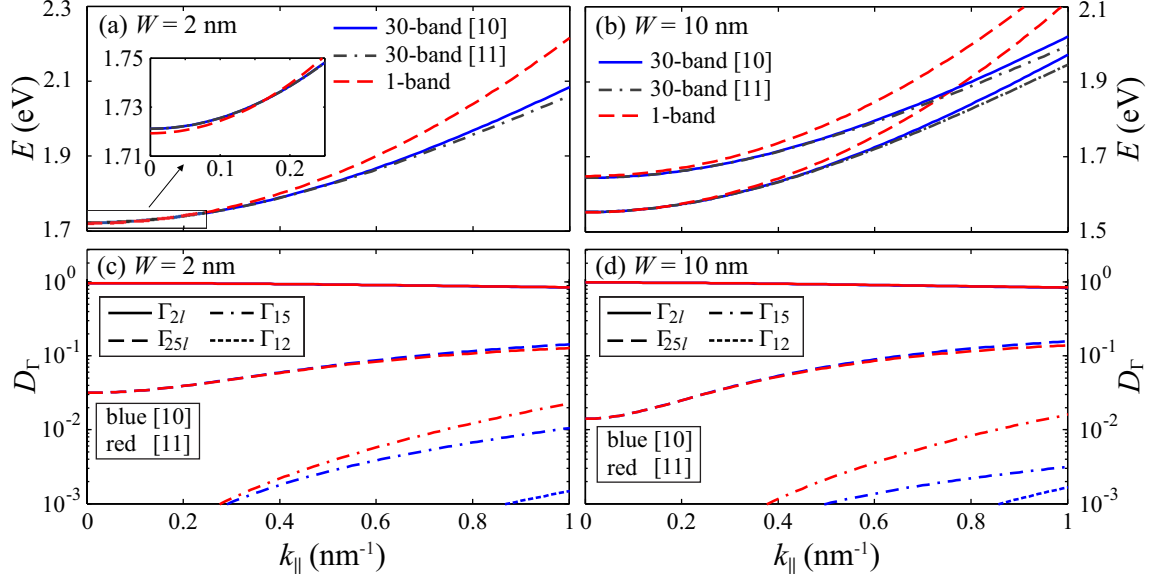


Figure 5.2: (Upper panel) The dispersion diagrams of the ground conduction subband in the GaAs/(Al,Ga)As quantum wells for (a) $W = 2$ nm and (b) $W = 10$ nm. Inset in (a) shows a detail in the range $k_{\parallel} \ll 1$ nm $^{-1}$. (Lower panel) Variations of four largest band contribution parameters with k_{\parallel} for: (c) $W = 2$ nm and $W = 10$ nm.

wards with respect to the dispersion relation along the [11] direction. It indicates that the effective masses of the conduction-band quantum well states are slightly larger along the [11] direction than along the [10] direction, which is qualitatively similar to the anisotropy of the heavy-hole and light-hole states in bulk semiconductors [150]. The anisotropy is a manifestation of the band mixing between the s -like and other Bloch states.

To demonstrate how the band mixing varies with k_{\parallel} , we plot in Figs. 5.2(c) and (d) the dependence of the band contribution parameters on k_{\parallel} for $W = 2$ nm and $W = 10$ nm, respectively. Also, variations of the band contribution parameters for the $n = 1$ subband along the [10] and [11] directions are displayed by blue and red lines in Figs. 5.2(c) and (d), respectively. For $W = 2$ nm, the Γ_{2l} (s -like) is the dominant band for both the [10] and [11] directions, and its contribution is identical for both directions, but it decreases from $D_{2l} = 0.968$ to $D_{2l} = 0.849$ when k_{\parallel} increases from 0 to 1 nm $^{-1}$. The contribution of the Γ_{25l} (p -like) zone-center states is rather large, and amounts to $D_{25l} = 0.143$ and $D_{25l} = 0.1277$ at $k_{\parallel} = 1$ nm $^{-1}$ for the dispersion relations along the [10] and [11] direction, respectively. A smaller contribution to the wave function of the conduction subband state arises from the Γ_{15} (p -like) zone-center states, as dash-dotted lines show in Fig. 5.2.

Similar to the contribution of the Γ_{25l} zone-center states, it increases with k_{\parallel} . The contribution of the d -like Bloch functions, displayed by short-dashed lines in Fig. 5.2 is smaller than 10^{-3} .

Moreover, because the contributions of the p -like zone-center states Γ_{25l} and Γ_{15} are non-zero, the dispersions of the subbands are anisotropic and the computed energies differ from the results of the single-band model. The contributions of different bands to the quantum well states for $W = 10$ nm are of similar magnitude to the case $W = 2$ nm, as could be deduced from comparison of Figs. 5.2(c) and (d). The variations of different D_{Γ} 's with k_{\parallel} plotted in Fig. 5.2(d) are qualitatively similar to the ones displayed in Fig. 5.2(c), except that the smaller contribution of the p -like and d -like states is found in the wider quantum well.

5.1.2 The Dresselhaus spin-orbit splitting

Since the 30-band model applied to GaAs and AlAs takes into account bulk-inversion asymmetry (BIA), there should emerge effects of spin-orbit interaction in the conduction subbands of GaAs/(Al,Ga)As quantum wells. The main such effect is the breaking of the double degeneracy of the conduction-band states, which could be modeled by the effective 2-band model proposed by Zawadzki and Pfeffer [203]

$$H_2 = \begin{bmatrix} H_A + H_B & K \\ K^+ & H_A - H_B \end{bmatrix}, \quad (5.3)$$

where

$$H_A = -\frac{\hbar^2}{2} \left[\frac{d}{dz} \frac{1}{m^*(z)} \frac{d}{dz} \right] + \frac{\hbar^2 k_{\parallel}^2}{2m^*(z)} + V(z), \quad (5.4)$$

$$H_B = i(k_x^2 - k_y^2) \left(\gamma \frac{d}{dz} + \frac{1}{2} \frac{d\gamma(z)}{dz} \right), \quad (5.5)$$

$$K = -i\sqrt{2}k_x k_y k_z \gamma(z) - \sqrt{2}k_+ \frac{d}{dz} \frac{1}{m^*(z)} \frac{d}{dz}. \quad (5.6)$$

Here, γ denotes the Dresselhaus SO coupling parameter, whose value can be extracted from the results of the 30-band calculations. By adopting the third-order perturbation

theory, the following expression for $\gamma(z)$ is derived in Ref. [203]

$$\begin{aligned} \gamma(z) = & \frac{4S_0P_0Q_0}{3} \left[\frac{1}{(E_{\Gamma_{2l}} + \Delta_{\Gamma_{25l}})(E_{\Gamma_{15}} - E_{\Gamma_{2l}})} - \frac{1}{(E_{\Gamma_{2l}})(E_{\Gamma_{15}} - E_{\Gamma_{2l}} - \Delta_{\Gamma_{15}})} \right] \\ & - \frac{4Q_0P_0^2\Delta_{\Gamma_{15},\Gamma_{25l}}}{9} \frac{1}{(E_{\Gamma_{2l}})(E_{\Gamma_{2l}} + \Delta_{\Gamma_{25l}})} \left[\frac{2}{E_{\Gamma_{15}} - E_{\Gamma_{2l}} - \Delta_{\Gamma_{15}}} + \frac{1}{E_{\Gamma_{15}} - E_{\Gamma_{2l}}} \right] \\ & - \frac{4Q_0S_0^2\Delta_{\Gamma_{15},\Gamma_{25l}}}{9} \frac{1}{(E_{\Gamma_{15}} - E_{\Gamma_{2l}} - \Delta_{\Gamma_{15}})(E_{\Gamma_{15}} - E_{\Gamma_{2l}})} \left[\frac{2}{E_{\Gamma_{2l}} + \Delta_{\Gamma_{25l}}} + \frac{1}{E_{\Gamma_{2l}}} \right]. \end{aligned} \quad (5.7)$$

Furthermore, Ref. [203] claimed that the linear-momentum matrix element Q_0 , which couples the Γ_{15} and Γ_{25l} states, is responsible for the Dresselhaus effect in the conduction band. However, we found that $Q_0 \neq 0$ in centrosymmetric crystals, silicon for example. Hence, Q_0 could not be responsible for the Dresselhaus spin splitting, which is exactly equal to zero in centrosymmetric semiconductors. Also, by careful inspection of the 30-band Hamiltonian it becomes obvious that the terms proportional to S_0 , which couples the Γ_{2l} and Γ_{15} states, and the spin-orbit parameter $\Delta_{\Gamma_{15},\Gamma_{25l}}$ are nonzero in the absence of the inversion symmetry. In other words, $S_0 \neq 0$ and $\Delta_{\Gamma_{15},\Gamma_{25l}} \neq 0$ are consequences of the Dresselhaus effect in the conduction band.

We calculate the BIA-induced splitting ΔE in the conduction band using the 30-band model and the 2-band model (Eqs. (5.3) and (5.7)) for both thin ($W = 2$ nm) and thick ($W = 10$ nm) quantum wells, where \mathbf{k}_{\parallel} is oriented along the [10] or [11] directions (see Fig. 5.3). Along with the results of the 30-band and 2-band models, which are shown by solid blue lines and dashed red lines, respectively, we determine the BIA-induced splitting by the 2-band model but for the γ value proposed in Ref. [154], which is displayed by dash-dotted gray lines in Fig. 5.3. The BIA coupling parameter γ has the values for GaAs and AlAs [154]

$$\gamma_{\text{GaAs}} = 2.445 \cdot 10^{-2} \text{ eVnm}^3, \quad \gamma_{\text{AlAs}} = 1.155 \cdot 10^{-2} \text{ eVnm}^3. \quad (5.8)$$

Upper panel in this figure displays the results for the $W = 2$ nm wide quantum well, and the results for $W = 10$ nm are shown in lower panel. For both values of W , it becomes obvious that the 2-band calculations using the different values of the γ parameter agree

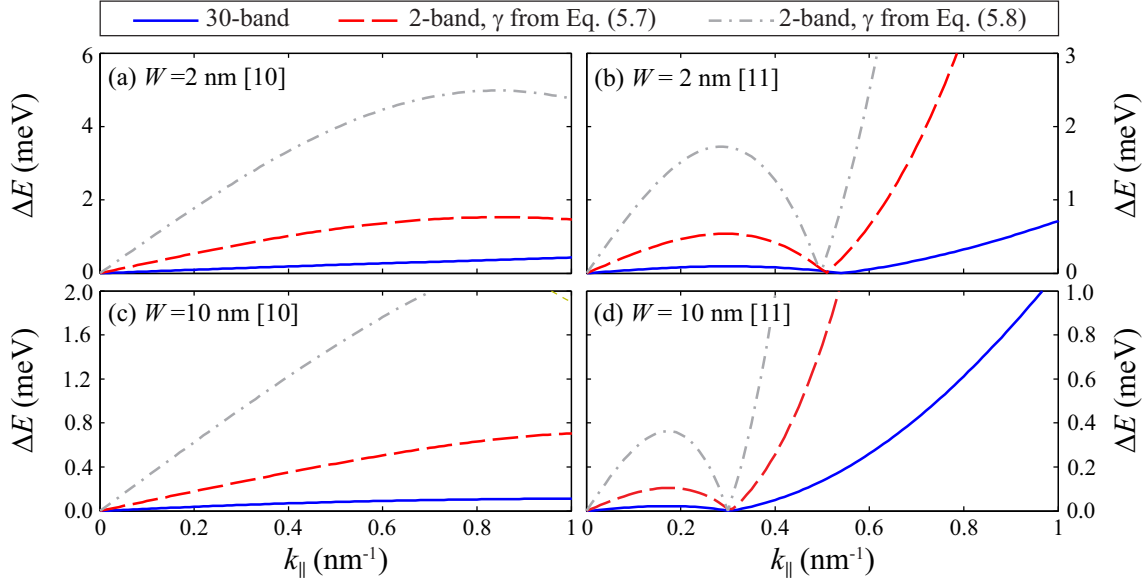


Figure 5.3: The Dresselhaus spin-orbit splitting of the ground electron state in the GaAs/(Al,Ga)As quantum well as a function of k_{\parallel} for: (a) $W = 2$ nm and the [10] direction, (b) $W = 2$ nm and the [11] direction, (c) $W = 10$ nm and the [10] direction, and (d) $W = 10$ nm and the [11] direction. Solid blue lines denote the results of the 30-band model, whereas the results obtained by the 2-band model for the Dresselhaus parameter γ computed by the third-order perturbation theory [203] and taken from Ref. [154] are displayed by dashed red and dash-dotted gray lines, respectively.

qualitatively well. However, there is a considerable quantitative difference between the energy splittings for the two values of the γ parameter. And the larger energy splitting is obviously computed for the γ parameter value taken from Ref. [154].

The results obtained for γ taken from Ref. [154] substantially overestimate the energy splitting computed by the 2-band model and the 30-band model (see Fig. 5.3). It is the situation for both quantum-well widths and both directions in the quantum-well plane. But the differences between the 2-band and 30-band models appear even at qualitative levels, especially along the [10] direction. Here, ΔE obtained from the 30-band model is a monotonically increasing function of k_{\parallel} , at least in the selected range of k_{\parallel} . On the other hand, the dispersion relations along the [10] direction determined by the 2-band model for the two values of γ exhibit the local maxima at $k_{\parallel} \approx 0.8 \text{ nm}^{-1}$. The similar maxima occurs in the energy splitting dependence on k_{\parallel} along the [11] direction. However, here ΔE variations with k_{\parallel} determined by the 2-band calculations have the zero at $k_{\parallel} \approx 0.5 \text{ nm}^{-1}$. The zero is also found by the 30-band calculations, but at $k_{\parallel} \approx 0.54 \text{ nm}^{-1}$. The

zeroes of ΔE as function of k_{\parallel} indicate that the energy states of the same quantum number n cross when k_{\parallel} increases [204].

Figs. 5.3(c) and (d) depict the BIA-induced energy splitting of the ground state in the 10 nm wide quantum well along the [10] and [11] direction, respectively. This splitting along both directions is considerably smaller than for the 2 nm wide quantum well. But, similar to the latter, the 2-band model yields larger energy splitting than the 30-band model. However, as Fig. 5.3(d) shows, the crossing of the spin-split states along the [11] direction determined by both 2-band and 30-band models takes place at the same value $k_{\parallel} \approx 0.3 \text{ nm}^{-1}$. We conclude that the 2-band model overestimates the Dresselhaus spin-orbit splitting irrespective of quantum-well width. And this discrepancy between the models does not alter when the orientation of the in-plane wave vector varies.

5.2 The hole states

The hole states are computed by both the 6-band model and the 30-band model, and the results are compared in Fig. 5.4(a), where the energies of a few highest-energy valence subbands at $k_{\parallel} = 0$ are displayed as function of the quantum well width. The $k_{\parallel} = 0$ states which are determined by the 6-band model can be classified as the heavy-hole states, the light-hole states, and the split-off states [168], and are denoted by $\text{HH}n$, $\text{LH}n$, and $\text{SO}n$, respectively. The energies of the $\text{SO}n$ states are much lower than the energies of the $\text{HH}n$ and $\text{LH}n$ states, due to the large spin-orbit split-off energy in both GaAs and (Al,Ga)As, which is of the order of a few hundreds of meV. This is the range of less practical interest, and therefore will not be considered.

The $k_{\parallel} = 0$ conduction subbands determined by the two models differ negligibly from each other, which is demonstrated by almost coinciding diagrams shown in Fig. 5.4(a). The agreement is much better than the one between the single-band and the 30-band calculations shown in Fig. 5.2(a). For the $\text{HH}1$ subband we found that the difference between the values obtained by the two calculations amounts to $\Delta E = 0.86 \text{ meV}$ for the $W = 2 \text{ nm}$ wide quantum well, and that it decreases with W . For the $\text{LH}1$ states this difference is $\Delta E = 1.8 \text{ meV}$ when $W = 2 \text{ nm}$, and the energies of the other states determined by the two methods differ by just few meV (see Fig. 5.4(a)). Similar to the conduction-band

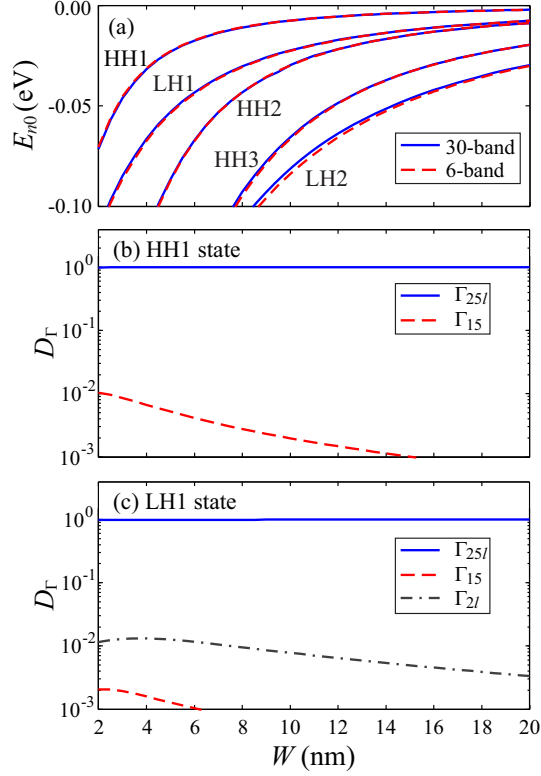


Figure 5.4: (a) Variations of the valence subbands energy extrema with quantum-well width. (b) The dependence of two largest band contribution parameters in the HH1 state on W . (c) The dependence of three largest band contribution parameters in the LH1 state on W .

states, the decrease of ΔE with W is a consequence of narrowing the range of the wave vectors of the bulk states which contribute to the quantum well states. When W is large, the envelope functions are formed out of the bulk solutions which have small k_z -values. As a consequence, the band mixing decreases, which is demonstrated in Figs. 5.4(b) and (c), where the variations of the band contribution parameters in the HH1 and LH1 states are displayed. The contribution of the Γ_{25l} (p -like) bands in the HH1 state equals 0.990 when $W=2$ nm, and increases to 0.999 when $W=20$ nm. Therefore, the mixing between the p -like states with the states of the other symmetry is even smaller than for the conduction subbands. For the LH1 subband at $k_{\parallel} = 0$, the D_{25l} amounts to 0.986 when $W = 2$ nm and reaches 0.996 for the $W = 20$ nm wide quantum well. We thus conclude that the 6-band model and the 30-band model of the valence-band states agree very well, at least for $k_{\parallel} = 0$.

In order to examine the obtained agreement between the two models more closely,

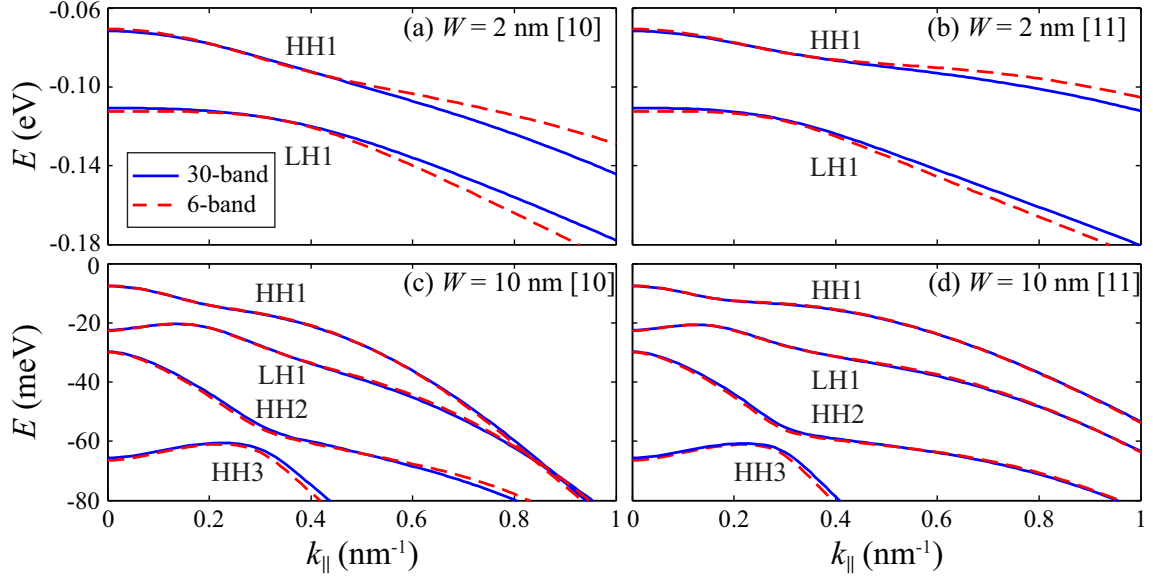


Figure 5.5: The dispersion diagrams of the valence subbands in the GaAs/(Al,Ga)As quantum well for: (a) $W = 2$ nm and the [10] direction, (b) $W = 2$ nm and the [11] direction, (c) $W = 10$ nm and the [10] direction, and (d) $W = 10$ nm and the [11] direction.

the dispersion relations of the subbands in the thin ($W = 2$ nm) and the thick ($W = 10$ nm) GaAs/(Al,Ga)As quantum well along the [10] and [11] directions, are shown in Figs. 5.5(a) and (b), respectively. When $k_{\parallel} \neq 0$ the subbands split due to the Dresselhaus effect, yet we found ΔE is not larger than 0.2 meV in the whole explored range of k_{\parallel} . Plotting the dispersion relations of both states which are split by the Dresselhaus term would blur the diagrams in Figs. 5.5(a) and (b), therefore we plot only the dispersions of the subbands whose energies are higher than their spin-split counterparts. For $k_{\parallel} < 0.4$ nm $^{-1}$ the dispersions along both the [10] and [11] directions determined by the 30-band and 6-band models are almost coinciding. The HH1-LH1 anticrossing at around $k_{\parallel} = 0.3$ nm $^{-1}$ is obviously present in both Figs. 5.5(a) and (b). When k_{\parallel} increases beyond 0.4 nm $^{-1}$, the difference between the HH1 energies computed by the 30-band and 6-band calculations increases, and reaches 15.4 meV and 7.1 meV at $k_{\parallel} = 1$ nm $^{-1}$ for the [10] and the [11] direction, respectively. The deviation of the LH1 energy determined by the 6-band model from the result of the 30-band calculation is similar to the case of the HH band, except that it has the opposite sign with respect to the HH1 state.

As could be inferred from comparison of the single-band and the 30-band calculations of the conduction subbands, the agreement between the two models is better in

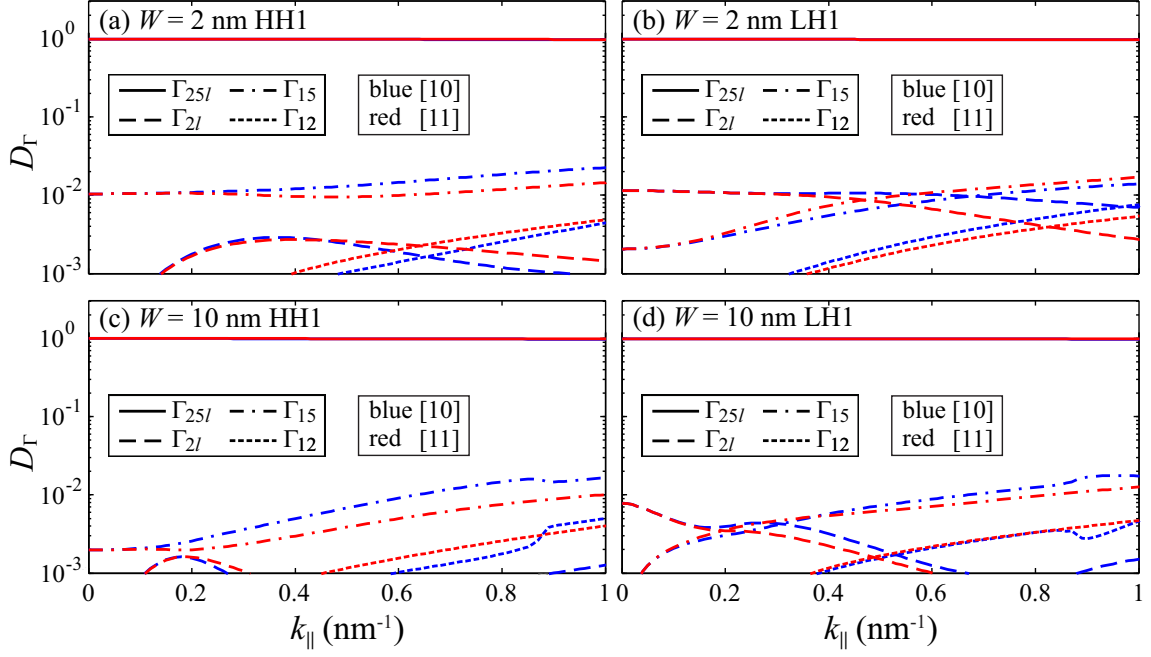


Figure 5.6: The band contribution parameters of the HH1 and the LH1 states in the GaAs/(Al,Ga)As quantum well as function of k_{\parallel} for: (a) $W = 2$ nm and the [10] direction, (b) $W = 2$ nm and the [11] direction, (c) $W = 10$ nm and the [10] direction, and (d) $W = 10$ nm and the [11] direction.

wider quantum wells. It is indeed shown in Figs. 5.5(c) and (d) where the hole dispersion relations in the $W = 10$ nm wide quantum well along the [10] and [11] directions are displayed, respectively. In this quantum well, however, there are two more subbands, denoted by HH1 and LH1, which exhibit an anticrossing near $k_{\parallel} = 0.3 \text{ nm}^{-1}$. The difference between the energy levels computed by the two methods is slightly larger than for the HH1 and LH1 subbands. Nonetheless, we found that the 6-band modelling of the valence-band states in quantum wells is quite accurate approach, such that its results does not differ much from those of the more complex 30-band modelling.

The variation of the composition of the HH1 states in the $W = 2$ nm wide well with k_{\parallel} is shown in Fig. 5.6(a). As could be inferred from Fig. 5.6(a) the HH1 state is almost completely composed of the D_{25l} zone-center functions. Furthermore, the band contribution parameter of the D_{25l} band decreases from 0.990 for $k_{\parallel} = 0 \text{ nm}^{-1}$ to 0.970 for $k_{\parallel} = 1 \text{ nm}^{-1}$ in both the [10] and [11] directions. The contribution of the p -like Γ_{15} conduction band to the HH1 state increases with k_{\parallel} , and for $k_{\parallel} = 1 \text{ nm}^{-1}$ it becomes as large as 0.023 and 0.015 for the [10] and the [11] direction, respectively. The contribution of the

other zone-center states is smaller than 0.01 for k_{\parallel} in the range from 0 to 1 nm^{-1} . Also, the contribution of the Γ_{25l} band to the LH1 state, whose variation with k_{\parallel} is shown in Fig. 5.6(b), is slightly smaller than the contribution of the same band in the HH1 state. It implies that the contribution of the other states is larger, and is a result of the band mixing, which is exactly taken into account in the 30-band theory and treated as a perturbation in the 6-band model. Therefore, the LH1 subbands computed by the 6-band model exhibit larger discrepancy from the 30-band model than the HH1 subbands (see Figs. 5.5(a) and (b)). In Fig. 5.6 we also see that the contribution of the Γ_{25l} band is larger in the [11] direction than in the [10] direction, thus the agreement between the energies of the valence subbands computed by the 6-band and 30-band models is better for the [11] direction than for the [10] direction. Figs. 5.6(c) and (d) respectively show the compositions of the HH1 and LH1 subbands in the $W = 10 \text{ nm}$ wide quantum well. By comparing Figs. 5.6(a) and (b) with 5.6(c) and (d), we see that the contributions of the bands other than the Γ_{25l} is smaller for $W = 10 \text{ nm}$. It explains why the 6-band and 30-band models agree better for thicker quantum wells, as Fig. 5.5 shows.

A subtle detail in Fig. 5.6(c) is the abrupt variation of the contributions of the Γ_{15} and Γ_{12} bands near $k_{\parallel} = 0.88 \text{ nm}^{-1}$ which is caused by the crossing between the HH1-LH1 subbands (see Fig. 5.5(c)). If the diagonal approximation of the LK Hamiltonian is adopted, the in-plane effective mass of the heavy holes is smaller than the effective mass of the light holes, and the opposite occurs along the [001] direction.¹ It therefore leads to the crossing between the HH and LH states, which is usually reverted to the anticrossing due to R and S elements (see Eqs. (2.37) and 2.38)) in the full-zone $\mathbf{k} \cdot \mathbf{p}$ model. As a matter of fact, a few anticrossings between the valence-band states are found in Fig. 5.5. However, increase of the off-diagonal terms with k_{\parallel} ($\sim k_{\parallel}$) is slower than the diagonal terms variation with k_{\parallel} ($\sim k_{\parallel}^2$), therefore the crossing in the $W = 10 \text{ nm}$ wide quantum well takes place at $k_{\parallel} = 0.88 \text{ nm}^{-1}$.

¹The diagonal approximation does not properly obey the symmetry of *bulk* semiconductors, and therefore gives inconsistent results with the full-zone $\mathbf{k} \cdot \mathbf{p}$ theory. Nevertheless, because confinement in quantum well makes the z direction different from the x and y directions, it might be employed to qualitatively account for the observed energy spectra in the quantum wells.

Chapter 6

Electron and hole states in ringlike quantum dots grown by droplet epitaxy

In this Chapter, a quantum dot of ringlike shape is considered (see Fig. 6.1(a)). Ringlike quantum dot consists of a disk surrounded by a ring, and its dimensions are defined in Fig. 6.1(a). R_1 denotes the radius of the disk, t is the thickness of the disk, R_2 is the outer radius of the ring, $W = R_2 - R_1$ is the width of the ring, and h is its height. The shape of such structure resembles the shape of fabricated droplet-epitaxy rings, and as indicated by recent measurements, have the inner radius R_1 of about 40 nm, the inner layer is about $t = 2$ nm high, the outer radius equals $R_2 = 100$ nm, and the ring height is $h = 5$ nm [108]. These dimensions are also taken in our calculations. Use of even smaller structures is advantageous for nanoelectronic and photonic applications, thus we will briefly compare the GaAs/(Al,Ga)As RQDs of the mentioned size with the RQDs made of the same materials but having dimensions typical for SK rings.

Varying dimensions of the disk with respect to those of the ring in the RQD would inevitably lead to changes in the spatial localization of the electron and hole. We explore a few ways to increase the disk volume: 1) radius of the disk R_1 is varied for constant outer radius of the ring R_2 , 2) radius of the disk R_1 is increased for constant width of the ring W , and 3) thickness of the disk t is varied for constant ring height h . The electronic structure of the conduction band is computed by means of the single-band effective mass equation, while the 4-band Luttinger-Kohn model (see Eq. (2.40)) is used to determine the valence-band states [145, 150, 184, 205].

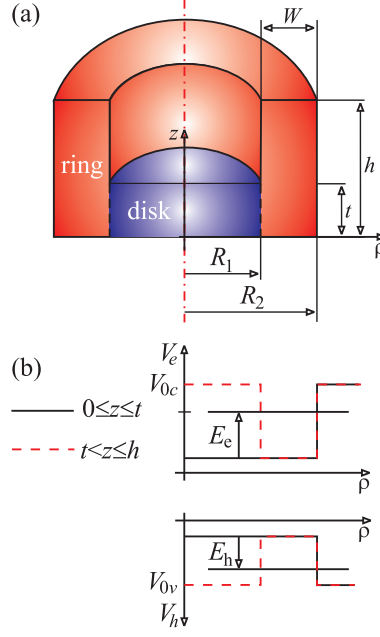


Figure 6.1: (a) The cross section and the characteristic dimensions of the RQD. The disk (blue colour) of the radius R_1 and thickness t , is located inside the ring (red colour) of outer radius R_2 and height h . (b) Variation of the conduction and valence band edges along the ρ direction at height $0 \leq z \leq t$ (solid line) and $t < z \leq h$ (dashed line).

6.1 The theoretical model

For simplicity, all the parameters of the band structure are assumed to be position-independent and to correspond to the material of the dot. Such an approximation is justified by the fact that both the electron and hole are mainly localized inside the dot, and that only a small part of the wavefunction leaks into the (Al,Ga)As matrix. This is a result of the relatively large potential offsets in both bands. The single-band effective-mass equation for the conduction band states has the form

$$H_e \psi_e = -\frac{\hbar^2}{2m} \nabla^2 \psi_e + V_e(\mathbf{r}) \psi_e = E_e \psi_e. \quad (6.1)$$

Here m denotes the effective mass of the electron in the conduction band, $V_e(\mathbf{r}) = V_e(\rho, z)$ is the confining potential, which is zero inside the quantum dot and equal to the conduction band offset V_{0c} in the semiconductor matrix.

The z projection of the orbital momentum L_z is a good quantum number for the axially symmetric confining potential, $L_z = l\hbar$. By taking into account axial symmetry of the

confining potential, the effective-mass equation becomes:

$$\begin{aligned}
& -\frac{\hbar^2}{2m} \frac{\partial^2 \psi_e}{\partial \rho^2} - \frac{\hbar^2}{2m} \frac{1}{\rho} \frac{\partial \psi_e}{\partial \rho} + \frac{\hbar^2}{2m} \frac{l^2}{\rho^2} \psi_e \\
& - \frac{\hbar^2}{2m} \frac{\partial^2 \psi}{\partial z^2} + V_e(\rho, z) \psi_e = E_e \psi_e,
\end{aligned} \tag{6.2}$$

where

$$\Psi_e(\varphi, \rho, z) = \frac{1}{\sqrt{2\pi}} \psi_e(\rho, z) e^{il\varphi}. \tag{6.3}$$

We classify the conduction-band states according to the orbital quantum number l , and denote them by nl , where n is the principal quantum number.

The hole states are extracted from the multiband effective-mass model:

$$H_h \underline{\Psi}_h = E_h \underline{\Psi}_h, \tag{6.4}$$

where $\underline{\Psi}_h$ denotes the Luttinger 4-band spinor, and H_h is the 4-band Luttinger-Kohn Hamiltonian consisting of the kinetic part $H_{LK}^{4 \times 4}$ (see Eq. (2.40)) and the potential matrix $V_h I_{4 \times 4}$ (see Fig. 6.1(b)) [145]:

$$H_h = H_{LK}^{4 \times 4} + V_h I_{4 \times 4}. \tag{6.5}$$

As shown in Fig. 6.1(b), the energy axis points from the valence band top downwards. The axial approximation is adopted in our approach, therefore the matrix element S of the LK Hamiltonian is simplified to:

$$S \approx -\sqrt{3} \frac{\gamma_2 + \gamma_3}{2} k_-^2. \tag{6.6}$$

Use of the axial approximation relies on a small difference between the Luttinger parameters γ_2 and γ_3 in GaAs (see Eq. (2.38)). Because of the axial symmetry, the z -projection of the total angular momentum $F_z = L_z + J_z$, commutes with the Hamiltonian. Here L_z denotes z -projection of orbital momentum corresponding to the envelope function, while J_z is z -projection of the angular momentum corresponding to the zone-center Bloch function and spin, and is given in Section 2.3.2. Therefore, f_z , is a good quantum number for hole

states, where $f_z \hbar$ is eigenvalue of the operator F_z . Since $F_z = L_z + J_z$, we conclude that $f_z = l + j_z$, where $l \hbar$ is an eigenvalue of L_z operator. In 4-band LK Hamiltonian j_z can take values $\pm 3/2$ and $\pm 1/2$ [150]. The H_h operator acts on the Luttinger 4-band spinor, which contains the envelope functions of the heavy and light holes,

$$\underline{\Psi}_h = \left[\Psi_1, \Psi_2, \Psi_3, \Psi_4 \right]^T. \quad (6.7)$$

Here, the envelope functions Ψ_1 and Ψ_4 ($j_z = \pm 3/2$) correspond to the heavy holes, while Ψ_2 and Ψ_3 ($j_z = \pm 1/2$) are the light-hole envelope functions. Each envelope function in the multiband spinor has the form

$$\Psi_i(\phi, \rho, z) = \frac{1}{\sqrt{2\pi}} \psi_i(\rho, z) e^{il_i \phi}, \quad (6.8)$$

where $l_i = f_z - j_z$ is the orbital momentum of the i -th component of the Luttinger spinor. For a given f_z , four orbital momenta l_i correspond to the spinor. As an example, the set of orbital momenta $\left[0, 1, 2, 3 \right]^T$ is associated with the $f_z = 3/2$ state. The hole states are labeled by $n|L|_f$, where L is the orbital momentum with the lowest magnitude in the set, i.e. $|L| = \min(|l_i|)$. Therefore, the ground $f_z = \pm 3/2$ state is denoted by $1S_{\pm 3/2}$, and the $+f_z$ states are degenerate with $-f_z$ states. The eigenstates in both the conduction and the valence bands are computed by expanding each $\psi_i(\rho, z)$ in products of the ρ -dependent Bessel functions of the first order J_l and the z -dependent sin/cos functions [184]

$$\begin{aligned} \psi_i(\rho, z) = & \sqrt{\frac{2}{H}} \sum_{n_\rho=1}^{N_\rho} A_{n_\rho l_k} J_{l_k} \left(\mu_{n_\rho l_k} \frac{\rho}{R} \right) \\ & \times \left[\sum_{n_z=1}^{N_z} a_{n_z k} \cos \left((2n_z - 1) \pi \frac{z}{H} \right) \right. \\ & \left. + \sum_{n_z=1}^{N_z} b_{n_z k} \sin \left(2n_z \pi \frac{z}{H} \right) \right]. \end{aligned}$$

Here, R and H denote the radius and the height of the simulation box, respectively, $A_{n_\rho l_k}$ is the normalization factor of the Bessel functions, $a_{n_z k}$ and $b_{n_z k}$ are the expansion coefficients, and $\mu_{n_\rho l_k}$ is the n_ρ -th zero of the Bessel function of l_k -th order.

In order to assess the spatial localization of the electrons and holes, we compute the

probabilities to find a particle in the disk,

$$p_d = \int_{V_d} \sum_{i=1}^{N_m} |\psi_i|^2 dV \quad (6.9)$$

and the ring,

$$p_r = \int_{V_r} \sum_{i=1}^{N_m} |\psi_i|^2 dV. \quad (6.10)$$

Here V_d and V_r denote the volumes of the disk and the ring, respectively, and N_m is the order of the Hamiltonian matrix: $N_m = 1$ for the conduction band, and $N_m = 4$ for the valence bands. Furthermore, the particle probability density

$$D(\rho, z) = \sum_{i=1}^{N_m} |\psi_i(\rho, z)|^2 \quad (6.11)$$

is computed.

6.2 Numerical results and discussion

We consider RQD made of GaAs and surrounded by $\text{Al}_{0.3}\text{Ga}_{0.7}\text{As}$. The dimensions of the dot are varied around the nominal values: $R_1 = 40$ nm, $R_2 = 100$ nm, $t = 2$ nm, and $h = 5$ nm [115]. The Luttinger parameters, the conduction-band electron effective mass, and the offsets in the two bands are taken from Ref. [139].

Three ways to increase the size of the disk are studied:

1. radius of the disk R_1 is varied while outer radius of the ring R_2 is kept at nominal value, $R_2 = 100$ nm;
2. radius of the disk R_1 is varied while width of the ring W is taken constant: $W = 60$ nm;
3. thickness of the disk t is varied for constant height of the ring, $h = 5$ nm.

In all these cases the volume of the disk is increased with respect to the volume of the ring, and therefore the energy states of the electron and the hole should change. Variation of

the energy levels with t will be compared with the electronic structure of smaller RQDs, whose radii $R_1 = 8$ nm, and $R_2 = 15$ nm are typical for SK RQDs [108].

6.2.1 $R_2 = \text{const}$, R_1 varies

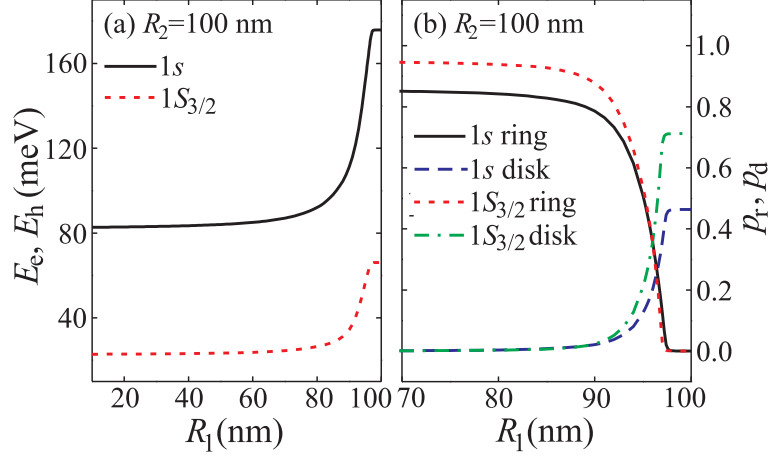


Figure 6.2: (a) The energies of the $1s$ and $1S_{3/2}$ states as they vary with R_1 for fixed $R_2 = 100$ nm. (b) Variation of the probabilities of localization inside the ring and disk with R_1 for $R_2 = 100$ nm.

We first explore how the energy levels and the spatial localizations of the electron and hole vary with R_1 in the range from 10 to 100 nm for fixed $R_2 = 100$ nm, and the constant thickness of the disk and height of the ring, $t = 2$ nm and $h = 5$ nm, respectively. When R_1 increases from 10 to 100 nm, the ratio V_r/V_d decreases from about 250 to 0. Increase of the disk radius reduces the space for the electron and the hole in the ring, therefore the eigenenergies increase, which is shown in Fig. 6.2(a). The eigenenergies shown in Fig. 6.2(a) increase slightly for $10 \text{ nm} \leq R_1 \leq 80$ nm. At $R_1 = 80$ nm, the volumes of the ring and the disk become comparable, which is followed by a large increase of the electron and hole energies when $R_1 > 80$ nm. The energies of both the $1p$ and $1S_{\pm 1/2}$ states differ by less than 1 meV from the energies of $1s$ and $1S_{\pm 3/2}$ states shown in Fig. 6.2(a). This might be ascribed to the large ring width. Even though the energies start to increase when R_1 exceeds 80 nm, the probabilities of localization in the rings and the disk do not change appreciably before R_1 exceeds 90 nm, as displayed in Fig. 6.2(b). p_r and p_d vary oppositely with R_1 , leading to crossings in both the electron and hole states at approximately 96 nm, when V_d is already about 5 times larger than V_r . One may notice

that p_r for the hole is larger than p_r for the electron in Fig. 6.2(b), which can be ascribed to the larger effective mass of the hole.

6.2.2 $W = \text{const}, R_1$ varies

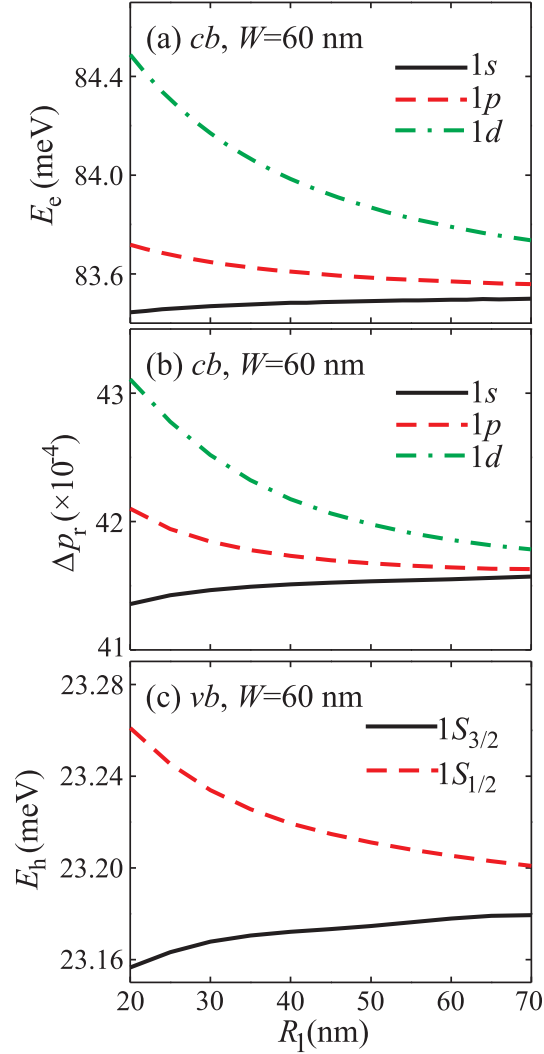


Figure 6.3: (a) The dependence of the electron energy levels on R_1 for fixed $W = 60$ nm. (b) The deviation of the probability of localization in the ring p_r from the value of 0.85 ($\Delta p_r = p_r - 0.85$) as it varies with R_1 . (c) Variation of the hole energy levels with R_1 for constant $W = 60$ nm.

Further, we consider how the electron and hole states vary when the ring width is kept constant, $W = 60$ nm, and the inner radius of the disk R_1 increases from 20 to 70 nm. Although the volume of the disk increases when R_1 increases, it stays always smaller than the volume of the ring. The energies of the $1p$, and $1d$ levels decrease when R_1

increases, whereas the ground $1s$ energy level increases, as shown in Fig. 6.3(a). The $1S_{\pm 3/2}$ and $1S_{\pm 1/2}$ hole energy levels show similar dependence on R_1 , as displayed in Fig. 6.3(b). Increase of the disk volume allows more space for the electron inside the disk, but the electron and hole in the ground states are mainly localized inside the ring. Interestingly, the energies of the ground electron and hole states increase slightly when R_1 increases. Such a situation might be considered within the adiabatic approximation ($E_e = E_{ez} + E_{ep}$), which is justified by the smaller height than the lateral size of the RQD. Furthermore, we approximate the ρ -dependent confining potential by the infinite barriers in the matrix. It is straightforward to derive the equation for the ρ -dependent part of the electron energy $J_l(kR_1)Y_l(kR_2) - J_l(kR_2)Y_l(kR_1) = 0$, where J_l and Y_l are the Bessel functions of the first and second kind, respectively, and $k = \sqrt{2mE_{ep}/\hbar^2}$. According to the solution of this equation, the energy of the electron ground state increases by $\Delta E_{1s} = E_{ep,1s}(R_1 = 70\text{nm}) - E_{ep,1s}(R_1 = 20\text{nm}) = 52.2\mu\text{eV}$ when R_1 increases from 20 to 70 nm. This agrees well with the result of our numerical calculations, where we found a value $\Delta E_{1s} = 54.2\mu\text{eV}$. Such a good agreement between the approximate and exact treatments indicate both that the radial confinement is dominant in the analyzed structure and that the electrons are mainly localized inside the ring. It also served as a successful test of the calculations by our model.

The probability to find the electron in the ring p_r decreases with R_1 , but only slightly, as shown by the plot of $\Delta p_r = p_r - 0.85$ in Fig. 6.3(b). Even though the volume ratio V_r/V_d decreases from 37 to 6, which is a factor of about 6, the probability p_r decreases negligibly from the values 0.85. The $1S_{\pm 3/2}$ and $1S_{\pm 1/2}$ hole energy levels displayed in Fig. 6.3(c) show similar dependence on R_1 to the electron energy levels. The hole localization changes similarly to the electron localization displayed in Fig. 6.3(b), and is negligibly reduced from the value of 0.95 when R_1 increases from 20 to 70 nm.

6.2.3 $h = \text{const}, t$ varies

The last case studied here regards fixing the radial dimensions ($R_1 = 40$ nm and $R_2 = 100$ nm) and $h = 5$ nm, and varying the thickness of the disk. The electron energy levels as they vary with t are shown in Fig. 6.4(a), respectively. Energies of the $1s$, $1p$, and $1d$ states obviously decrease with t , which is due to an increase of the dot's volume.

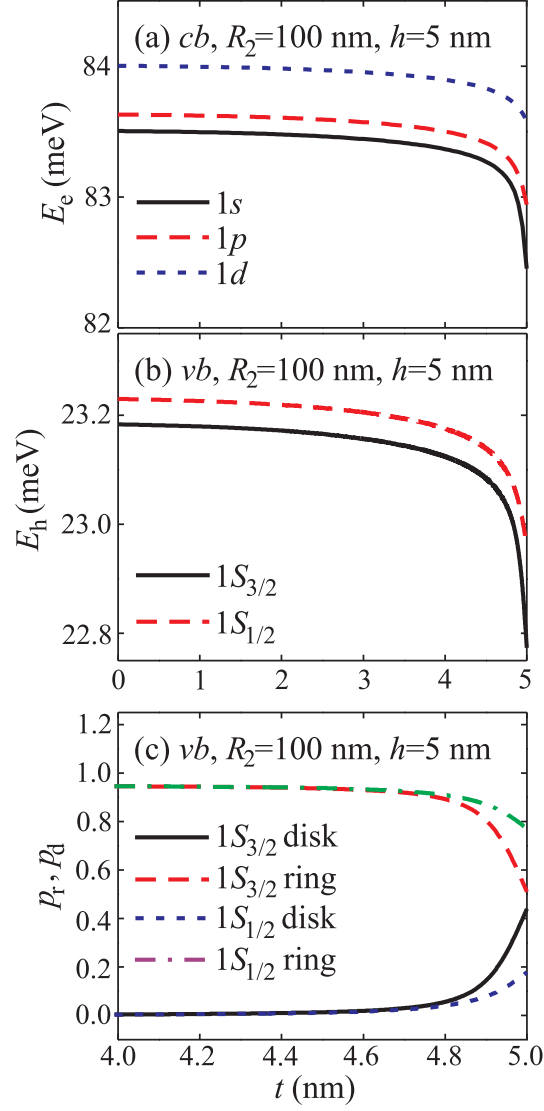


Figure 6.4: Variations of: (a) the conduction-band and (b) the valence-band energy levels with t in the ring of the inner radius $R_1 = 40$ nm, the outer radius $R_2 = 100$ nm, and the height $h = 5$ nm. (c) The probabilities of localization of the holes inside the ring p_r and inside the disk p_d as they vary with t .

The hole states, shown in Fig. 6.4(b) are similarly affected by varying t . In both cases displayed in Figs. 6.4(a) and (b), the energies are almost constant when t varies in the range $t < 0.8h$. Also, the wavefunctions negligibly leak from the ring into the disk, as illustrated by the diagram of the p_r dependence on t for the hole states in Fig. 6.4(c). When $t = h$, p_r 's for the $1S_{3/2}$ and $1S_{1/2}$ hole states become comparable, and sum up to almost unity due to a negligible leakage of the wavefunction into the (Al,Ga)As matrix. When $t = 4.5$ nm, which is 90% of the ring height, the ground hole state is almost completely

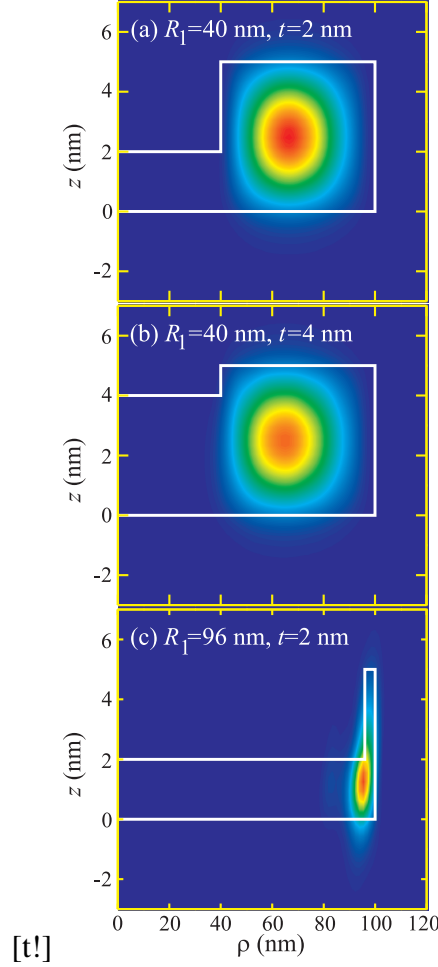


Figure 6.5: Contour plots of the probability density of the hole states in the RQD of outer radius $R_2 = 100$ and height $h = 5$ nm for: (a) $R_1 = 40$ nm and $t = 2$ nm, (b) $R_1 = 40$ nm and $t = 4$ nm, and (c) $R_1 = 96$ nm and $t = 2$ nm.

localized inside the ring. Therefore, even though the layer inside the ring is present, it negligibly affects the hole localization. Only when the thickness of the layer inside the ring opening reaches the height of the ring, it starts to be important. The demonstrated dominant localization of the holes in the rim of the ringlike GaAs/(Al,Ga)As structures is advantageous for the appearance of topological effects in them. Because the average thickness of the disk in the fabricated non-ideal ring DE rings is about half of the disk height [115] the electron and hole states are mainly localized in the ring, and therefore the Aharonov-Bohm oscillations of the electron and hole states and possibly exciton, should appear there.

In order to illustrate spatial localization of the holes when the disk height varies, we

plot in Figs. 6.5(a) and (b) the probability densities of the $1S_{\pm 3/2}$ states for $t = 2$ nm and $t = 4$ nm thick disks, respectively. Because the ring is wide in both these cases, both Figs. 6.5(a) and (b) demonstrate that no appreciable relocation of the hole wave function from the ring to the disk takes place when t increases. However, when R_1 approaches R_2 , the hole wavefunctions become squeezed in the ring and the probability density starts to be shifted to the disk, as Fig. 6.5(c) shows for the radius of the disk $R_1 = 96$ nm.

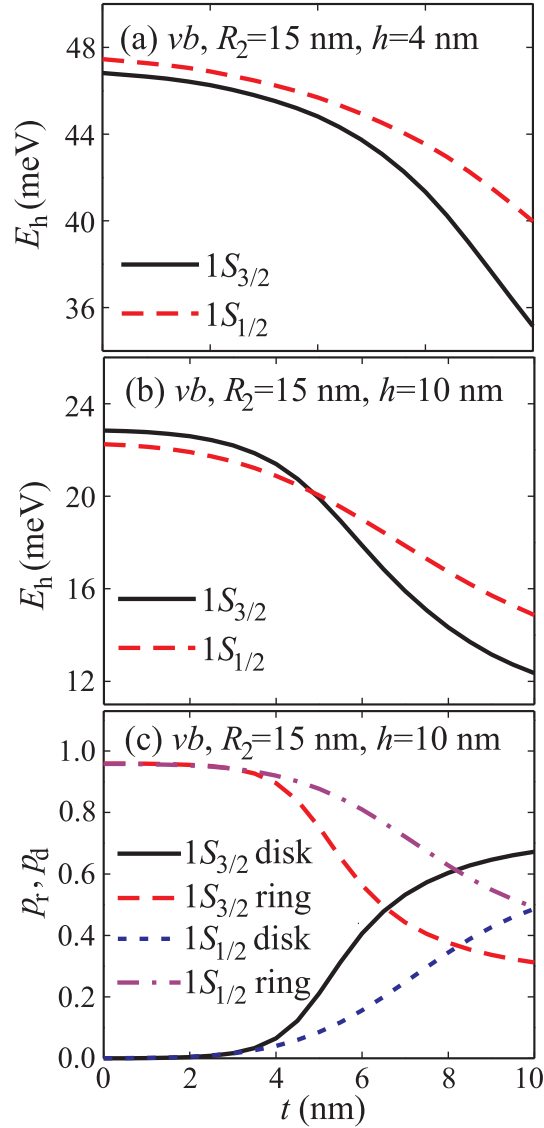


Figure 6.6: Variations of the hole energy levels with t in the: (a) $h = 4$ nm and (b) $h = 10$ nm high RQD. (c) p_r and p_d in the $h = 10$ nm high RQD. The lateral dimensions are $R_1 = 8$ nm and $R_2 = 15$ nm.

In order to demonstrate that the electronic structure depends on the lateral size of the ring, we show in Fig. 6.6(a) the hole energies in the ring with inner radius $R_1 = 8$ nm, outer radius $R_2 = 15$ nm, and height $h = 4$ nm. These dimensions are typical for SK rings [108]. Similarly to what was previously found for larger rings, the $1S_{3/2}$ state is the hole ground state irrespective of the disk thickness, and the energy levels change within a larger range (compare Figs. 6.4(b) and 6.6(a)). However, when the disk height increases to the value $h = 10$ nm, the $1S_{1/2}$ becomes the ground hole state in the fully-opened ($t = 0$) ring, as shown in Fig. 6.6(b). Change of the angular momentum of the ground state is a consequence of the comparable height to the width of the ring. Therefore variation of h is able to produce large modifications of the electronic structure of the RQD. Still, at approximately $t = h/2$ the ground state changes symmetry from $1S_{1/2}$ state to the $1S_{3/2}$, which can be inferred from in Fig. 6.6(b). The reversal of the hole angular momentum arises from the larger space offered to the $l = 0$ envelope functions around the center of the dot. Hence, the $1S_{\pm 3/2}$ state, which contains the dominant $l = 0$ component of the heavy holes, becomes the ground hole state for $t > h/2$. Also, the wavefunctions are mainly localized in the ring for only $t < h/2$, as illustrated by the diagram of the p_r dependence on t in Fig. 6.6(c), whereas the dependence of p_r on t in larger rings shown in Fig. 6.6(c) is much steeper and the holes are mostly confined inside the ring for $t < 0.9h$.

The zone center matrix elements, which contribute to the matrix elements for the interband optical transitions, are generally different for the heavy and light holes. Therefore, the $1S_{\pm 3/2}$ and $1S_{\pm 1/2}$ states respond differently to light of a given polarization. But when the two have equal energies, which we find for $t \approx 5$ nm in the $h = 10$ nm high dot, there exists a finite probability to occupy both of them, and therefore the optical transitions should be less sensitive to polarization of incoming light, which might be advantageous for photonic applications [206]. Also, the variations of dimension can strongly affect Aharonov-Bohm oscillations, therefore in the next Chapter we consider the RQD in a magnetic field.

Chapter 7

Ringlike quantum dots in a magnetic field

Both the SK and DE techniques lead to the formation of non-ideal nanorings, whose shape can be approximated nanodot composed of a disk, and the ring surrounding it (See Fig. 6.1(a)). The lateral dimensions of the (In,Ga)As/GaAs nanorings, R_1 and R_2 , are typically a few nanometer, whereas the width ($W = R_2 - R_1$) of the GaAs/(Al,Ga)As nanorings formed by the droplet epitaxy can be up to a few hundreds of nm [105, 107].

Even though both the SK and DE created ringlike structures lacking the full opening, both these structures are found to exhibit Aharonov-Bohm (AB) oscillations when an external magnetic field threads the ring [12, 207]. The AB effect is due to the magnetic field induced change of the phase of the wave function, and in circular rings it manifests itself by transitions between states of different orbital momenta. These transitions, and therefore the AB effect are absent in singly connected quantum dots [208]. It implies that the electronic structure of a RQD shown in Fig. 6.1 in a magnetic field changes from ringlike to disk-like with increasing thickness of the disk inside the ring.

Because of band mixing, the valence-band states in quantum rings could be affected by the presence of strain in a more intricate manner than the conduction-band states. For the case of type-II SK-grown quantum dots and quantum-dot molecules, in Refs. [160, 184] it was shown that varying the thickness of the dot affects the strain distribution, and in turn the band mixing. Electron, hole and exciton states in (In,Ga)As/GaAs RQD of realistic geometry has been considered in Ref. [123]. The interplay between band mixing and

strain causes different variations of the electron and hole states with the magnetic field. In addition to the electron and hole states, other important effects that originate from the AB effect, such as persistent currents and orbital magnetism [12, 108] could also be affected by the presence of the disk inside the RQD.

Let us briefly note that in addition to the electron and hole energy levels, the exciton energy levels should also be affected by increasing thickness of the disk in the RQD. The exciton ground state energy exhibits oscillations with the magnetic field, which is called the *excitonic Aharonov-Bohm effect* [209–211]. This effect has been sought in 3D quantum rings for some time [212], whereas it only recently has been observed in (In,Ga)As/GaAs quantum rings [15, 213]. The theory revealed that the presence of strain is an important ingredient for the appearance of excitonic AB oscillations in type-I quantum rings [107, 123].

In this Chapter, we compute and analyze the influence of magnetic field on the electron and hole states in a ring containing disk inside the opening, whose geometry and characteristic dimensions are displayed in Fig. 6.1(a). Previously different analytical functions were adopted to model the shape of the fabricated rings. For the SK-grown rings, Fomin et al. [105] used a function which takes into account both the extension of the ring material in the opening and the deviation from axial symmetry in the xy plane [105]. In Refs. [214] and [123] quantum rings of more realistic shape have been described. Still, the existence of the AB effect is related to topology rather than exact shape of the structure. Furthermore, in the geometrical model presented here, the effects of the inner layer on the electronic structure are expressed through a single parameter, the disk thickness t .

The effects of strain on the electronic structure are explored by: (1) comparing the electron and the hole energy levels in the (In,Ga)As/GaAs RQD and (2) comparing the hole states in the strained SK-fabricated (In,Ga)As/GaAs RQD with those in the unstrained DE-formed GaAs/(Al,Ga)As. The effects due to varying the disk thickness on the angular momentum transitions and mixing between the hole states are particularly explored. Even though the DE-formed GaAs/(Al,Ga)As RQDs are in general larger, for comparative purposes, we assume here that their dimensions are equal to those of the (In,Ga)As/GaAs dots. We also analyze how the presence of the disk in the RQD affects the magnetization due to the single particle states [14]. The influence of the geometry of

the structure on the electron and hole energy levels is briefly discussed. Finally, we note that our calculations do not aim to analyze any particular sample of currently fabricated quantum rings. Nevertheless, the present model could provide a qualitative description of the electronic structure of experimental quantum rings where the layer is present inside the ring opening.

7.1 Theoretical models

Here, we compute the electronic structure of strained (In,Ga)As/GaAs and unstrained GaAs/(Al,Ga)As RQDs (see Fig. 6.1). Strain distribution in the (In,Ga)As/ GaAs RQD is determined from the model of isotropic strain described in Section 2.7. Since perpendicular magnetic field is present, the symmetric gauge, given by Eq. (2.55). The electron states are computed using the single-band Schrödinger equation for the case of the present magnetic field (see Eq. (2.54)), while the hole states are computed using the 4-band LK Hamiltonian given by Eq. (6.5) under the axial approximation. Also, the Zeeman term (see Eq. (2.56)) is added to the LK Hamiltonian (6.5). In the case of strained RQD, the potential part in both single-band and LK Hamiltonian is modified according to Eq. (2.62). Magnetic field is included in the kinetic part of the Hamiltonian using the substitution $\mathbf{k} \rightarrow -i\nabla + e\mathbf{A}/\hbar$. Since the magnetic field along the z -axis does not break axial symmetry, the z -projection of the total angular momentum $F_z = L_z + J_z$ commutes with the Hamiltonian, as in the case of zero magnetic field considered in Chapter 6. Therefore, f_z remains to be a good quantum number.

We assumed that the Luttinger parameters and the electron effective mass are position independent, and that their values equal to the values for the the material of the quantum dot, since the hole and the electron are mainly localized there. Note that strain is taken into account in the diagonal matrix elements of the Hamiltonian. The off-diagonal matrix elements depend on the shear strain tensor components and the difference $\epsilon_{xx} - \epsilon_{yy}$ [215]. For the case of quantum disks the shear strain-tensor components were found to be localized in the small regions close to the dot boundary [184]. Similarly, the difference between ϵ_{xx} and ϵ_{yy} is small in the axial geometry. Hence, the off-diagonal matrix elements could be neglected, which along with the axial approximation of the kinetic part of

the Hamiltonian makes the model axially symmetric [123, 184].

Inclusion of the magnetic field in the LK model of the valence band states in two vertically coupled quantum disks has been analyzed in Ref. [216]. The results from the LK Hamiltonian (see Sections 2.3.2 and 2.6) were compared with those of a model which contains magnetic terms in only the main diagonal [104, 217]. The latter model was constructed by employing substitution $\mathbf{p} \rightarrow \mathbf{p} + e\mathbf{A}$ in the Schrödinger equation prior the envelope function approximation, which was not the case in the Luttinger-Kohn model. Therefore, the off-diagonal terms due to magnetic field are removed in the Hamiltonian of Ref. [217]. Quite interestingly, even though the latter model is an approximate approach, it leads to splitting of the energy levels in the magnetic field which is qualitatively similar to the experimental data [216]. Therefore, such comparison indicated that the off-diagonal magnetic terms in the original Luttinger-Kohn model are too large when applied to a quantum ring. Similar to the quantum dots previously analyzed by the approximate Hamiltonian, the removal of the off-diagonal elements due to magnetic field in the multiband model of the quantum dot is expected to reduce the general (increasing or decreasing) trend of the hole ground state variation with the magnetic field. However, the magnetic off-diagonal terms could not have a large influence on the positions of the angular momentum transitions between the hole states of different total orbital momenta, as Ref. [104] demonstrated for the case of the quantum ring. Moreover, the model of Ref. [217] relies on an *ad hoc* approach, whereas the LK model of the hole states in a magnetic field is a consistent procedure, which successfully explained the valence-band states of various semiconductors and their nanostructures in a magnetic field. Its restrictions are basically related to the size of the system and the influence of the interface. Furthermore, the hole states in a nanostructure should tend towards the bulk states when the size of the system increases. In the approximate theory of Ref. [217] this could be difficult to achieve, because mixing due to magnetic field with states outside the basis set is not taken into account.

The LK Hamiltonian acts on the Luttinger spinor $\underline{\Psi}_h$ given by Eq. (6.7). Envelope functions in both LK and single-band model are expanded according to Eq. (6.8). The hole states are labelled by $n|L|_{f_z}$, where n denotes the principal quantum number, and L denotes the minimum value of l_k in the Luttinger spinor (see Eq. (6.7)), i.e. $L = \min(|l_k|)$,

where $k \in 1, 2, 3, 4$.

In order to compare the electronic structure of the analyzed 3D ring with the one of the 1D ring, we compute a few characteristics of the electron and hole states in the analyzed RQDs. First, we note that the orbital momentum transitions in the 1D rings correspond to the magnetic flux $\Phi = (i - 1/2)\Phi_0$ ($\Phi_0 = h/e$ is the flux quantum; $i = 1, 2, 3, \dots$) through the ring [12]. Therefore, we define the effective radius of the equivalent 1D ring,

$$R_{eff,i} = \sqrt{(i - 1/2)\Phi_0 / (\pi B_i)}, \quad i = 1, 2, 3, \dots \quad (7.1)$$

where B_i is the magnetic field of the i -th angular momentum transition in the analyzed RQD. Second, the probability density of the hole in the ground state is computed as using Eq. (6.11). Third, the magnetization due to the single electron and the single hole is computed as

$$M = \mp \frac{\partial E_1}{\partial B}. \quad (7.2)$$

Here, E_1 is the ground state energy, the upper sign is for the electron, and the lower sign for the hole.

For convenience, the energy of the electron ground state is denoted by $E_{(1)}^X$, where X labels the RQD: $X = \text{GaAs}$ for the GaAs/(Al,Ga)As RQD, and $X = \text{InGaAs}$ for the (In,Ga)As/GaAs RQD.

7.2 Numerical results and discussion

We consider RQDs composed of: (1) GaAs/Al_{0.3}Ga_{0.7}As and (2) In_{0.5}Ga_{0.5}As /GaAs. The compositions of (Al,Ga)As and (In,Ga)As are taken close to the experimental values [108, 115]. Furthermore, both dots are chosen to have equal dimensions: height $h = 5$ nm, the inner radius $R_1 = 8$ nm, and the outer radius $R_2 = 15$ nm. These dimensions correspond to the experimental (In,Ga)As RQDs, whereas the GaAs RQDs are typically larger and their shape differs from the (In,Ga)As RQDs [108, 115, 213]. Nevertheless, our aim is to estimate how strain affects the electron and hole states in the dot, and to resolve these effects from the effects of varying size when the disk thickness varies. The Luttinger parameters, the band-offsets, the deformation potentials, and the effective masses are all

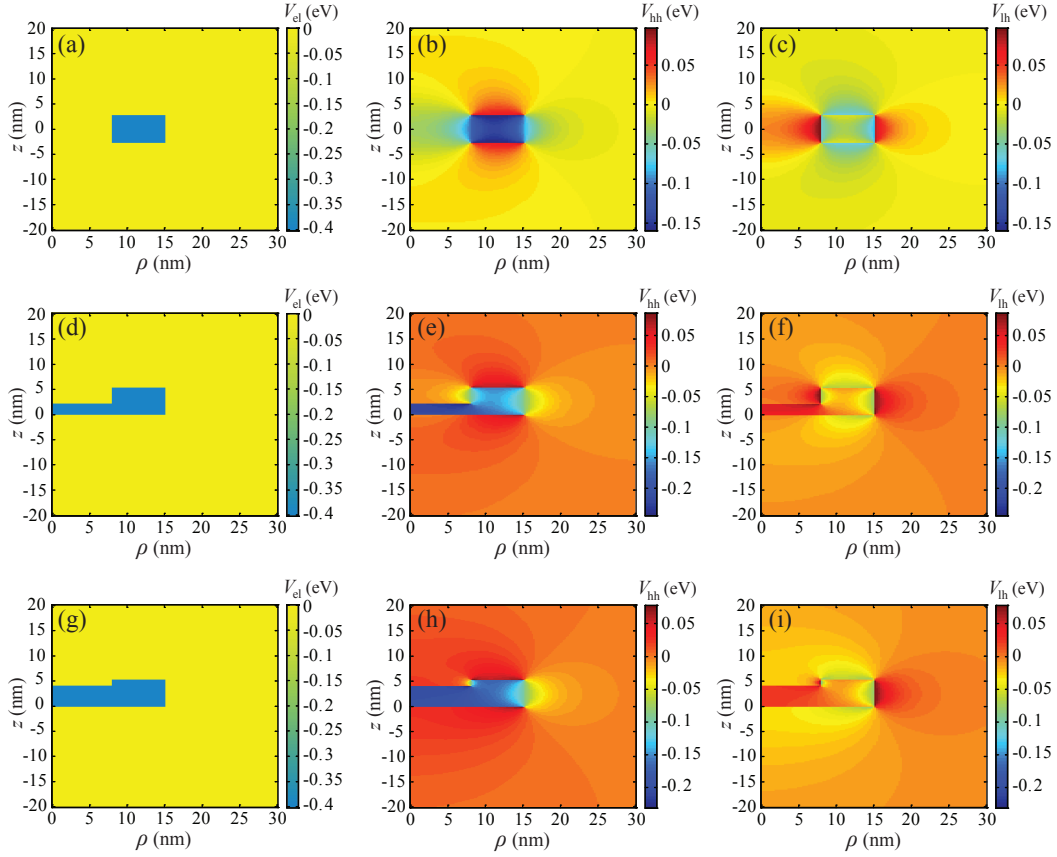


Figure 7.1: The effective potentials for the single particle states in the (In,Ga)As/GaAs RQDs as they vary with the disk thickness. (Upper panel) The case of a fully-opened quantum ring ($t = 0$): (a) V_{el} , (b) V_{hh} , and (c) V_{lh} . (Middle panel) The quantum dot with a $t = 2$ nm thick disk: (d) V_{el} , (e) V_{hh} , and (f) V_{lh} . (Lower panel) The quantum dot with a $t = 4$ nm thick disk: (g) V_{el} , (h) V_{hh} , and (i) V_{lh} .

taken from Ref [139]. The effective Landé g -factor is taken to be equal $g_{eff} = -0.44$, and the κ Luttinger parameter equals $\kappa = 1.72$ [177]. Those values correspond to GaAs, but in the (In,Ga)As RQDs the measured Zeeman splitting is much smaller than what is expected from the bulk values of g_{eff} and κ . The values estimated from such measurements are in fact closer to the experimental values for the GaAs matrix [218], therefore we adopt the same g_{eff} and κ in both analyzed quantum dots.

7.2.1 The effective potentials

Contour plots of the effective potentials in the conduction, heavy-hole, and light-hole bands in the (In,Ga)As/GaAs RQD are displayed in Fig. 7.1. The upper panel in Fig. 7.1

(Figs. 7.1(a)-(c)) displays the effective potentials in the quantum ring ($t = 0$), the middle panel (Figs. 7.1(d)-(f)) shows the effective potentials in the RQD with a $t = 2$ nm thick disk, and the lower panel (Figs. 7.1(g)-(i)) shows the effective potentials for $t = 4$ nm. The effective potentials in the conduction band V_{el} depend on the hydrostatic strain, and are therefore step-like in all three cases displayed in Fig. 7.1 (see Figs. 7.1(a), (d), and (g)). Increase of the disk thickness does not affect the hydrostatic strain, thus the conduction-band states in the (In,Ga)As/GaAs and the GaAs/(Al,Ga)As dots are similarly affected by the presence of the disk inside the ring opening.

Because of both the hydrostatic and tetrahedral deformations of the structure, the effective potentials for the heavy and light holes are different. For the case of the quantum ring ($t = 0$), the effective potential well for the heavy hole inside the dot is deeper than the effective potential well for the light hole, as Figs. 7.1(b) and (c) show. Furthermore, the shallow confining potential wells for the heavy hole extend laterally, whereas a similar confining potential for the light hole extends vertically above and below the ring. However, because of the shallower effective potential well inside the ring, the light hole is less confined than the heavy hole.

For the case of a finite t , a superposition of strain fields inside the disk and around the ring produces a deeper effective potential well for the heavy hole inside the disk than in the ring (see Figs. 7.1(e) and (h)). Therefore, strain favors confinement of the heavy hole in the disk. When t increases from 2 nm to 4 nm, no large changes in V_{hh} is observed (compare Figs. 7.1(e) and (h)). On the other hand, the effective potential barrier for the light hole in the RQD increases, except close to the outer boundary of the dot, as Figs. 7.1(f) and (i) show. When t/h approaches unity, the regions of confining V_{lh} above and below the ring extend towards the dot center, which establishes the confinement of the light hole in the matrix around the dot boundary, like for a disk [123, 160, 184].

7.2.2 The conduction-band states

The energy levels in the conduction band of the GaAs/(Al,Ga)As RQD with a $t = 0$ nm, 2 nm, and 4 nm thick disk are shown in Figs. 7.2(a), (b), and (c), respectively. The orbital momentum of the electron ground state is explicitly shown, and the points where the different l states cross in the electron ground state are connected by thin dashed lines in

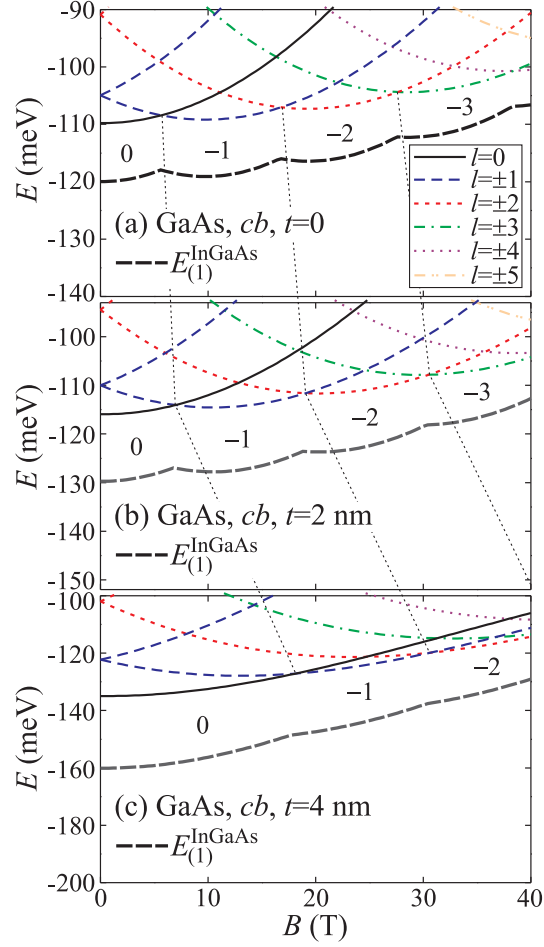


Figure 7.2: The lowest energy spin-up electron energy levels for orbital momenta $|l_e| \leq 5$ in the GaAs RQD as function of the magnetic field, for: (a) $t = 0$, (b) $t = 2$ nm, and (c) $t = 4$ nm. The orbital momentum of the ground cb state is explicitly denoted in each diagram, and the crossings of the different l states are joined by the thin dashed lines. The thick dashed line is the energy of the electron ground state in the (In,Ga)As/GaAs dot.

the different diagrams. For comparison, variations of the energy of the electron ground state in the (In,Ga)As/GaAs RQD $E_{(1)}^{\text{InGaAs}}$ with the magnetic field are shown by the thick dashed lines. For convenience, the values of $E_{(1)}^{\text{InGaAs}}$ in Fig. 7.2 are increased by 75 meV. For all three values of the disk thickness, both $E_{(1)}^{\text{GaAs}}$ and $E_{(1)}^{\text{InGaAs}}$ vary oscillatory with the magnetic field due to the orbital momentum transitions. The crossings between different l states in the ring (see Fig. 7.2(a)) are almost periodic with the magnetic field, like in 1D rings, where the orbital momentum transitions, are odd multipliers of half of the flux quantum divided by the area of the ring [12]. From the value of the magnetic field of the first and the second orbital momentum transition in the analyzed quantum ring, $B_1 = 5.6$

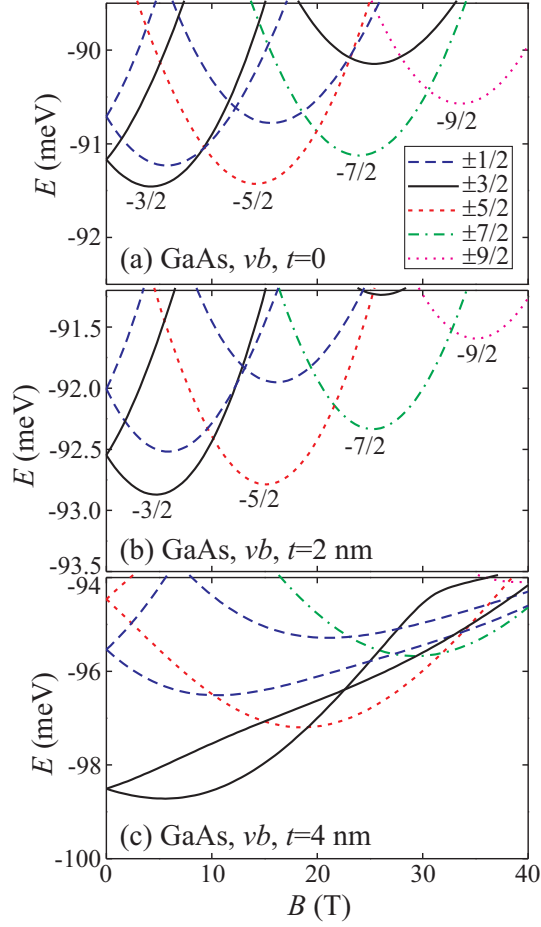


Figure 7.3: The energy levels in the valence band of the GaAs/(Al,Ga)As RQD for: (a) the $t = 0$, (b) the $t = 2$ nm, and (c) $t = 4$ nm thick disk. The z -projection of the total angular momentum is explicitly denoted in the figures.

T and $B_2 = 16.8$ T, the radii of the equivalent 1D rings amount to $R_{eff,1} = R_{eff,2} = \sqrt{\Phi_0/2\pi B_1} = 10.8$ nm, which is close to the average ring radius $(R_1 + R_2)/2 = 11.5$ nm.

When the disk thickness increases, the orbital momentum transitions shift towards larger values, as the thin dashed lines joining the orbital momentum transitions in the three diagrams indicate in Fig. 7.2. These shifts are almost constant, which is demonstrated by nearly parallel thin dashed lines. For $t = 2$ nm, which is 40% of the ring height, the orbital momentum transitions shift negligibly from the $t = 0$ case (compare Figs. 7.2(a) and (b)). But, when t increases to 4 nm (80% of the ring height), the orbital momentum transitions shift by about 13 T (compare Figs. 7.2(a) and (c)). Moreover, increasing the confinement inside the disk favors the low $|l|$ states, therefore $R_{eff,1}$, which is determined from the crossing between the $l = 0$ and $l = -1$ electron energy levels, become much

smaller than $R_{eff,k}$ for $k > 1$. The ground energy level in the (In,Ga)As/GaAs dot varies with B similarly to the GaAs/(Al,Ga)As quantum dot, as the thick dashed lines depict in Fig. 7.2. Hence, a modification of the material parameters do not produce any qualitative change of the obtained energy spectra in the conduction band.

7.2.3 The valence-band states

The zero magnetic field hole ground state in the GaAs/(Al,Ga)As RQD is found to be in the total angular momentum state $f_z = -3/2$ irrespective of the value of t , as is clear from Figs. 7.3(a), (b), and (c) for $t = 0$, $t = 2$ nm, and $t = 4$ nm, respectively. The $f_z = -3/2$ state is dominated by the heavy hole envelope function with $l = 0$. When B increases, the states of different f_z cross in the ground states, but because of the band mixing B_1 is shifted with respect to B_1 for the electron ground state (compare Figs. 7.2(a) and 7.3(a)). However, the other angular momentum transitions that occur in the ground state are separated by almost fixed intervals of B . Such a similarity to the conduction-band states could be ascribed to arise from similar effective potentials for the electrons, heavy and light holes. The angular momentum transitions are associated with the change of the orbital momenta of all the components of the Luttinger spinor by -1. Furthermore, similar to the conduction band, the angular momentum transitions between the valence-band states do not shift much when t increases from 0 to 2 nm, as shown in Figs. 4(a) and (b). But when t increases to 4 nm, those shifts become considerable (see Fig. 7.3(c)).

The variations of the hole states with magnetic field in the (In,Ga)As/GaAs ring (the $t = 0$ case) shown in Fig. 7.4(a) are similar to the ones presented in Ref. [104]. Also, they are similar to the orbital momentum transitions in the conduction band (see Fig. 7.2). However, they are arranged differently than the angular momentum transitions in the GaAs/(Al,Ga)As ring, which was shown in Fig. 7.3. It indicates that mixing is reduced in the (In,Ga)As/GaAs quantum rings, which indeed occurs due to different effective potentials of the heavy and light holes in a strained system. Furthermore, because of the large difference between the Luttinger parameters, the hole ground energy levels in the two systems exhibit opposite trends with B (compare Figs. 7.3(a) and 7.4(a)). For non-zero value of t , strain favors confinement of the heavy hole in the disk, as is apparent from Figs. 7.4(b) and (c) for $t = 2$ nm and $t = 4$ nm, respectively. The deeper effective potential

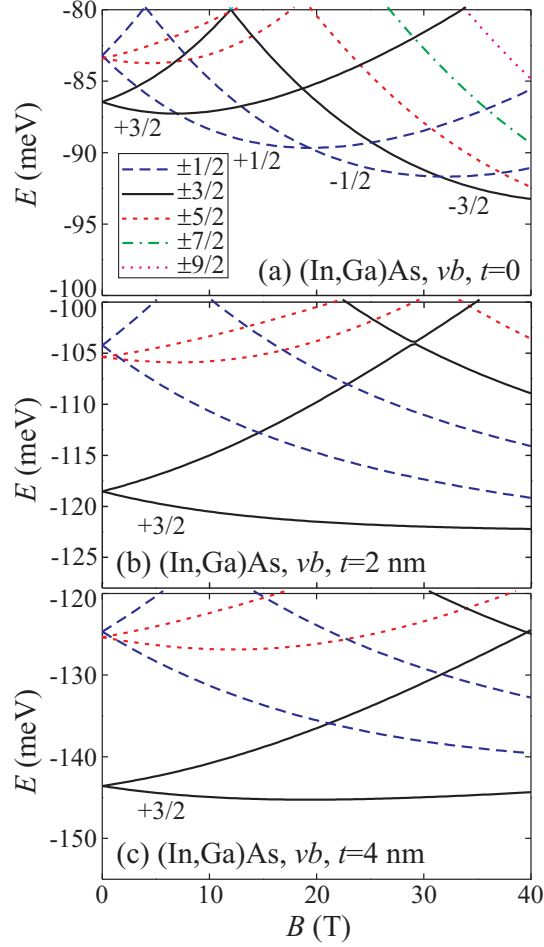


Figure 7.4: The same as Fig. 7.3, but now for the (In,Ga)As/GaAs RQD.

well in the disk as compared to the ring causes the heavy-hole states to be mainly localized in the disk, which favors the low $|l|$ states. As a consequence, the $1S_{+3/2}$ state, which has the $l = 0$ heavy hole component, is the hole ground state in the whole investigated range of B , i.e. from 0 to 40 T. On the other hand, since the effective potential barrier for the light holes is erected inside the disk, the $1S_{1/2}$ state, having the $l = 0$ light-hole component, occupies the ring.

In order to illustrate how strain influences the hole localization, we show in Fig. 7.5 the probability density of holes (D_h) in the ground state for $B = 0$. The left panel in this figure (Figs. 7.5(a)-(c)) shows D_h in the GaAs/(Al,Ga)As ring, and the right panel (Figs. 7.5(d)-(f)) displays D_h in the (In,Ga)As/GaAs ring. For $t = 0$, the hole is mainly localized inside the ring. But in the (In,Ga)As/GaAs RQD, which contains the inner layer D_h extends more to the ring center, which is a consequence of the confining effective

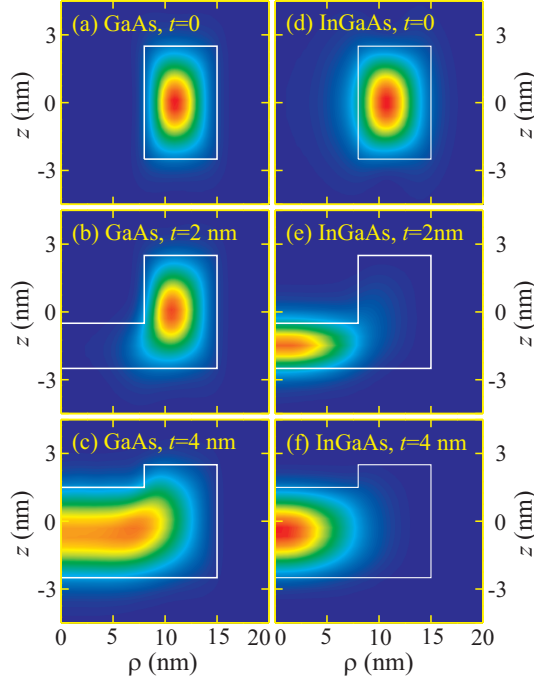


Figure 7.5: (Left panel) The probability density of the single hole D_h in the GaAs/(Al,Ga)As RQD for: (a) $t = 0$, (b) $t = 2$ nm, and (c) $t = 4$ nm. (Right panel) D_h in the (In,Ga)As/GaAs dot for a few values of the disk thickness: (d) $t = 0$, (e) $t = 2$ nm, and (f) $t = 4$ nm.

potential for the heavy holes in the ring opening. The presence of the thin disk in the GaAs/(Al,Ga)As RQD does not considerably affect D_h , as shown in Fig. 7.5(b) for $t = 2$ nm. On the other hand, V_{hh} in the (In,Ga)As/GaAs RQD confines the hole more inside the disk, which is responsible for the extension of D_h towards the dot center, as shown in Fig. 7.5(e) for $t = 2$ nm. For $t = 4$ nm, D_h in both RQDs becomes localized inside the disk, as Figs. 7.5(c) and (f) show for the GaAs/(Al,Ga)As and the (In,Ga)As/GaAs RQD, respectively. However, because of strain, the hole in the (In,Ga)As/GaAs RQD is practically completely localized around the center of the disk, which leads to the absence of the angular momentum transitions in Fig. 7.4(c).

7.2.4 Comparisons between the conduction and valence band states

The similarity between the GaAs/(Al,Ga)As and (In,Ga)As/GaAs systems is due to their equal topology and the similar confining potentials for the electron. Therefore, we show in Fig. 7.6(a) the dependence of B_i ($i = 1, 2, 3$) with t/h for both systems. As inferred

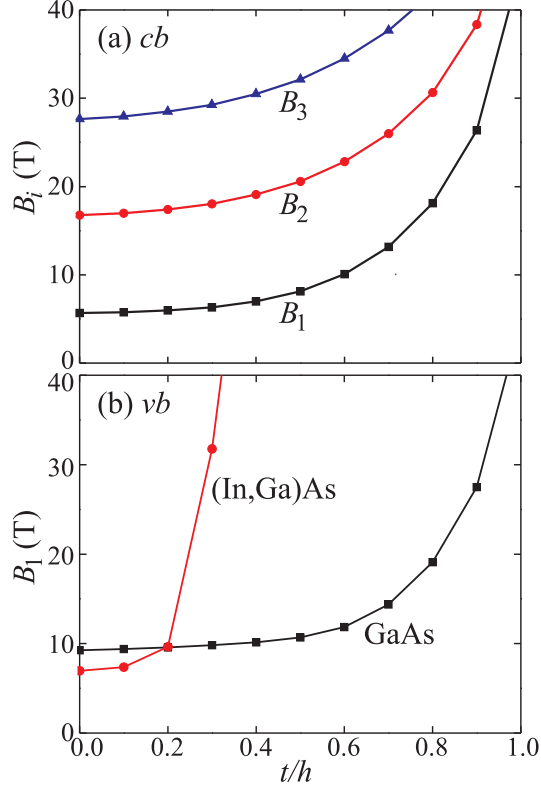


Figure 7.6: (a) The values of the magnetic field B_1 , B_2 , and B_3 , where the first three transitions between the orbital momenta of the spin-up electron states take place in the conduction band of the RQD as function of the ratio between the disk thickness and the ring height t/h . The curves correspond to both the GaAs/(Al,Ga)As, and the (In,Ga)As/GaAs RQDs. (b) The values of the magnetic field B_1 for the valence-band states as function of t/h .

from Fig. 7.2, B_i 's are almost constant for $t/h \leq 0.4$, i.e. for $t \leq 2$ nm, but increases rapidly when t/h exceeds 0.4. One may notice that B_1 is about 3 times larger at $t/h = 0.8$ ($t = 4$ nm) than B_1 for the quantum ring ($t = 0$). Besides, all curves in Fig. 7.6(a) are almost parallel for $t/h < 0.6$, which could also have been inferred from Fig. 7.2 by the nearly parallel thin dashed lines. For $t = h$, when the system becomes a quantum disk, no angular momentum transitions exist for a single electron. Thus, all three curves in Fig. 7.6(a) tend to infinity when t/h approaches unity.

Because an increase of t leads to both a decrease of the effective potential well for the heavy hole and an increase of the effective potential barrier for the light hole in the disk, the energy difference between the $1S_{+3/2}$ and $1S_{+1/2}$ in the strained (In,Ga)As ring at $B = 0$ increases, as Fig. 7.4 shows. Consequently, the first angular momentum transition

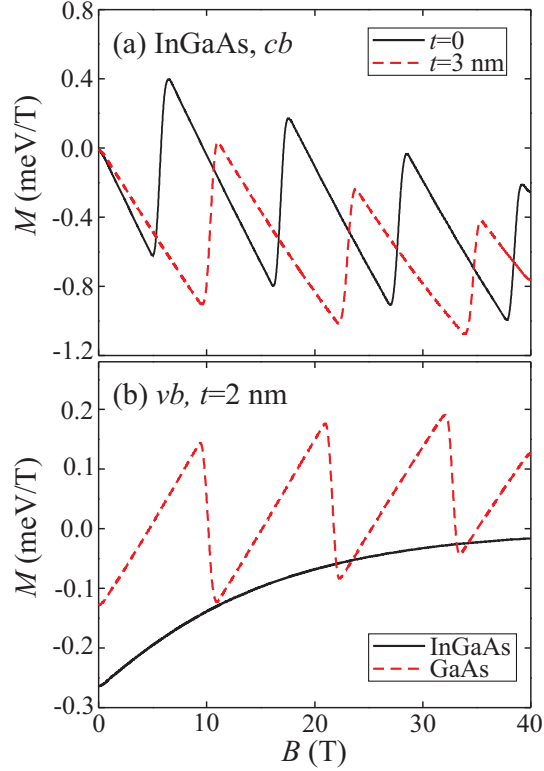


Figure 7.7: (a) The magnetization of a single electron in the (In,Ga)As/GaAs RQD for $t = 0$ (solid black line) and $t = 3$ nm (dashed red line). (b) The magnetization of a single hole in the (In,Ga)As/GaAs (solid black line) and the GaAs/(Al,Ga)As RQD (dashed red line) for $t = 2$ nm.

between the hole states, shift to much larger values of B than those between the electron states, as Fig. 7.6(b) displays. Furthermore, B_1 for the hole in the (In,Ga)As ring increases to a much larger value than B_1 for the GaAs ring, when t/h increases, as Fig. 7.6(b) shows.

For $t = 2$ nm, Figs. 7.2(b) and 7.2(b) demonstrate that the electron states are affected by the magnetic field as they are confined in the ring, whereas the dependence of the hole ground energy level is characteristic of singly connected disks. Therefore, the electron and the hole are spatially separated like in the case of a type-II singly connected quantum dot, which is a favorable situation for the appearance of excitonic AB oscillations [219]. In such small structures, such as the quantum dot considered here, the exciton is in the strong confinement regime [220], therefore, the AB oscillations of the exciton should be governed by those of the single particle states.

The peculiar variation of the energy levels with the disk thickness in the strained (In,Ga)As/GaAs RQD affects the magnetization of the single electron, as Fig. 7.7(a) dis-

plays for $t = 0$ and $t = 3$ nm. Due to shifts of the orbital momentum transition, the first abrupt step in the M vs B dependence for $t = 3$ nm takes place at about 10 T, which is larger by about 4 T from the value for $t = 0$. The dependence of magnetization of the single hole in both systems for $t = 2$ nm is shown in Fig. 7.7(b). Because of the smooth variation of $E_{(1)}^{\text{InGaAs}}$, no oscillations of the hole magnetization are found in the case of the (In,Ga)As/GaAs RQD, whereas almost periodic oscillations occur for the GaAs/(Al,Ga)As RQD. The smooth dependence of M on B in the (In,Ga)As/GaAs RQD containing a single hole illustrates the previously corroborated fact that the presence of even a thin layer inside the ring opening considerably modifies the electronic structure of the quantum ring.

7.2.5 Influence of the geometry

In order to explore how the geometry affects the electron and hole states in the RQD, we extend our calculations to the strained quantum disks having a bulge of a triangular cross section on its periphery, as shown in Fig. 7.8(a). Because of the peculiar shape of the rim, we call such a quantum dot a Λ -dot, and the previous quantum dot of rectangular cross section could be called the Π -dot. The characteristic dimensions of the Λ -dot R_1 , R_2 , t , and h have similar meaning as for the Π -dot, whereas R_p denotes the position of the rim vertex (see Fig. 7.8(a)). The shape of this Λ -dot approaches closely the shape of the experimental quantum rings [108], except that the Λ -dot is axially symmetric, whereas this is not the case for the strained (In,Ga)As/GaAs quantum rings explored in Refs. [105, 108]. Furthermore, these quantum rings exhibits substantial compositional mixing between the dot and the matrix. Hence, the boundary of the experimental quantum rings could not be exactly specified. However, we disregard this effect, and assumed fixed composition of $x = 0.5$ in the $\text{In}_x\text{Ga}_{1-x}\text{As}$ alloy inside the quantum dot, and that the matrix is composed of GaAs [105]. From the available cross section in Refs. [105, 108] we extracted the following values of the Λ -dot dimensions: $R_1=7$ nm, $R_2=15$ nm, $R_p =12$ nm, $t = 2$ nm, and $h = 4$ nm. The shape of the experimental quantum rings is anisotropic in the xy plane, which in addition to the disk presence, is able to shift the angular momentum transitions in the electron and hole ground energy levels with magnetic field [105, 108]. In order to treat the in-plane anisotropy in the RQD, a 3D model should be employed [123].

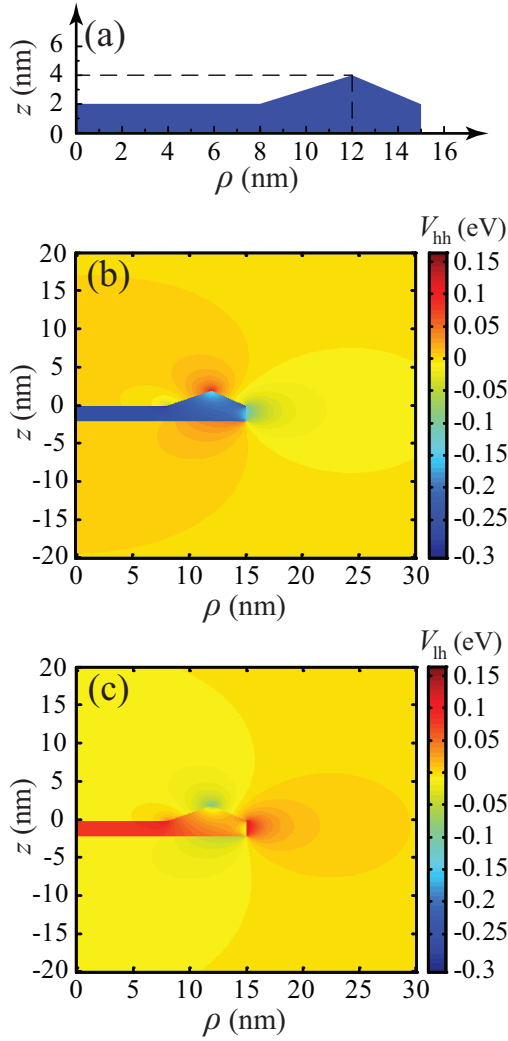


Figure 7.8: The case of the quantum disk having the bulge of the triangular cross section on the radial periphery (the Λ -dot): (a) the shape and the characteristic dimensions, (b) V_{hh} , and (c) V_{lh} .

The effective potential in the heavy-hole band of the Λ -dot is displayed in Fig. 7.8(b). Similar to the Π -dot, the effective potential well for the heavy hole is deeper inside the disk than in the rim. Furthermore, inside the rim the depth of the potential well decreases from the base to the rim vertex. The effective potential in the light-hole band is such that, similar to the Π -dot, the barrier is erected inside the disk, which is displayed in Fig. 7.8(c). This barrier is higher in the Λ -dot than in the Π -dot, therefore, it would lead to a smaller contribution of the light-hole states to the hole wave function, and in turn, to reduced mixing between the heavy-hole and light-hole bands. We note that the effective potential in the conduction band, which is not shown in Fig. 7.8, is qualitatively similar to the one

in the Π -dot (see Fig. 7.1).

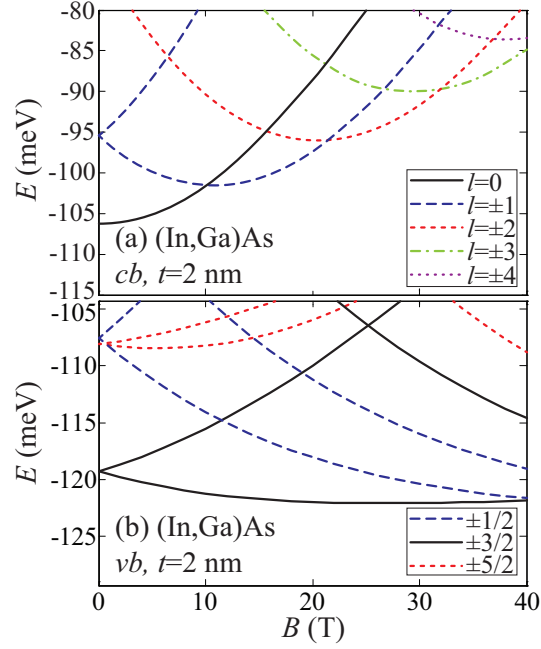


Figure 7.9: The variations of the electron (a) and the hole (b) energy levels with magnetic field in the Λ -dot.

The electron and hole energy levels in the Λ -dot are shown in Figs. 7.9(a) and (b), respectively. For the electron ground state in Fig. 7.9(a) we determine $B_1 = 10$ T, whereas $B_1 = 5.6$ T was previously extracted from the electron ground energy level variation with B in Fig. 7.2(a). The difference between the two values could be explained to arise from smaller volume of the rim in the Λ -dot. Nevertheless, B_1 for the electron ground state in the Λ -dot is smaller than 14 T which was the value of B_1 measured in Ref. [108]. The larger value of B_1 determined in the experiment is a consequence of the in-plane anisotropy of the quantum rings explored in Ref. [108], which is not taken into account in our model. The hole ground energy level variations in the Λ - and Π -dots exhibit similar behavior when B varies, i.e. they are both continuous in the range $[0, 40\text{T}]$ (see Fig. 7.4(b)). The small difference between the two could be explained by the deeper effective potential well for the heavy hole in the rim and increased barrier for the light hole inside the disk, as Figs. 7.8(a) and (b) demonstrate. The potential barrier for the light holes leads to a decrease of the light-hole component in the hole ground state envelope functions. Yet, the changes of the hole energy spectra due to the modified geometry are

not large, which implies that geometry of the axially symmetric quantum dots is not of a detrimental influence on the appearance and period of the Aharonov-Bohm oscillations in the electron and hole ground state energy levels.

Finally, we note that our calculations indicate that in strained RQD there exists a range of t where the hole is confined similar like in a disk and the electron like in a ring. Such a localization is advantageous for the appearance of the excitonic AB oscillations. However, in order to realize such a situation, one should control the thickness of the inner layer during the growth process of strained self-assembled quantum rings. The compositional intermixing and the considerable anisotropy of the shape in the xy plane is often present in the currently fabricated quantum rings [105, 108]. Previous measurements indicated that the orbital momentum transitions between the electron states are preserved even in the presence of anisotropy [108], even though they are shifted by a large amount from the $t = 0$ case. More recently, oscillations in the exciton ground state energy of nearly axially symmetric (In,Ga)As/GaAs quantum rings were measured [213]. Nonetheless, even these rings contained a layer inside the opening.

Chapter 8

Conclusion

In this thesis the electronic structure of Si/SiO₂ quantum wells, GaAs/AlGaAs quantum wells, GaAs/AlGaAs and InGaAs/GaAs ringlike quantum dots are studied using the $\mathbf{k} \cdot \mathbf{p}$ theory. In Chapter 1 we presented various fabrication techniques which are employed to produce the mentioned nanostructures, and the band structure of Si and III-V compounds is briefly discussed.

Chapter 2 presents fundamentals of the $\mathbf{k} \cdot \mathbf{p}$ theory. Here, derivations of the single-band effective-mass model, the Dresselhaus-Kip-Kittel model, and the Luttinger-Kohn models were presented. The 30-band Hamiltonian, which is able to accurately model bulk band structure in the whole Brillouin zone, was then explained. Also, it was demonstrated that external potentials which exist from band offset variation, mechanical strain, and magnetic field are easy to implement in multiband $\mathbf{k} \cdot \mathbf{p}$ models. The conceptual framework of the multiband envelope function approximation is demonstrated to suffer from presence of spurious solutions in the energy spectra. All analyzed nanostructures are assumed to be grown along the [001] direction, and to have realistic dimensions. In Chapter 3 we used a basis consisting of standing waves within the 30-band $\mathbf{k} \cdot \mathbf{p}$ model to solve the electronic structure of Si/SiO₂ quantum well grown in the [001] direction. For the assumed infinite potential steps at the well boundaries, we found that numerous spurious solutions are present in the computed electron and hole spectra. These spurious states are classified into two categories: the high- k states which arise from the contribution of the states outside the first Brillouin zone, and the extra-valley spurious states which arise from the spurious valley outside the first Brillouin zone. The missing symmetry of the

conduction band in bulk silicon as modeled by the 30-band $\mathbf{k} \cdot \mathbf{p}$ Hamiltonian is found to be the cause of the extra-valley spurious states in the conduction band. Furthermore, we devised procedure which is able to remove the low-energy spurious states from both the conduction and valence-band energy spectra. The latter is found to exhibit instabilities due to a peculiar band mixing and the specific boundary conditions, when the order of the employed basis varies. This failure of the 30-band $\mathbf{k} \cdot \mathbf{p}$ model might heuristically be accounted for by a large difference of the electron confinement in the hard-wall silicon quantum well and the silicon bulk. However, if the hard-wall confinement is made softer the deficiencies in the 30-band $\mathbf{k} \cdot \mathbf{p}$ approach are found to disappear for the adequately chosen size of the simulation box and the basis order. Further, the choice of the numerical method is not relevant for the demonstrated instability of the hole states, i.e. we found that it also exists if the finite-difference or finite-element methods are adopted to solve the 30-band eigenvalue problem.

According to the results we showed in Chapter 3, in Chapter 4 we modeled the interband optical absorption in Si/SiO₂ quantum wells of width comparable to the excitonic Bohr radius in Si. We determined the influence of quantum confinement on the interband optical absorption. Interband optical absorption in Si/SiO₂ quantum wells, as modeled by the multiband $\mathbf{k} \cdot \mathbf{p}$ theory shows a strong dependence on the quantum well width. The interband matrix elements are found to exhibit an oscillatory variation with the quantum well width. The effective band gap in the quantum well is found to be well described by a W^{-2} dependence. The conditions under which the interband transition matrix element vanish are found from a set of simple rules. Moreover, our results indicate that the quantum well width can be used as a design parameter to enlarge the interband absorption in narrow Si/SiO₂ quantum wells.

In Chapter 5 we showed how the 30-band $\mathbf{k} \cdot \mathbf{p}$ is applied to compute the electronic structure of GaAs/(Al,Ga)As quantum wells. This model is compared with the single-band approach of the conduction band states, and the 6-band Luttinger-Kohn model of the valence-band states. The employed low order $\mathbf{k} \cdot \mathbf{p}$ models are found to agree well with the 30-band approach if quantum wells are wider than 10 nm, and for the in-plane wave vector smaller than 0.1 nm⁻¹. Furthermore, best agreement between the models was demonstrated in the electron and hole ground subbands. Such behavior could indeed

be inferred knowing that the states close to the Γ point could be well determined by the perturbation theory applied to the zone-center states. Hence, the theory works best for description of narrow regions around $k_{\parallel} = 0$, and for wide quantum wells, when mixing with distant bands is small. This mixing was found to be largest between the Γ_{25l} , Γ_{2l} and Γ_{15} zone center states, which are explicitly taken in the 14-band model. Thus, our calculations indicate that the 14-band $\mathbf{k} \cdot \mathbf{p}$ theory would accurately determine the electron and hole states in GaAs/(Al,Ga)As quantum wells. Moreover, the Dresselhaus spin-orbit splitting was computed, and it was found to have the similar functional dependence on the well width and the in-plane number as the result obtained by the perturbative 2-band model. Nonetheless, it was demonstrated that the 2-band approach considerably overestimates the Dresselhaus spin splitting extracted from the 30-band theory.

The electron and hole states in ringlike quantum rings were shown and analyzed in Chapter 6. Here, the GaAs/(Al,Ga)As system, which could be obtained by the droplet epitaxy, and the strained (In,Ga)As/GaAs quantum dots fabricated by the Stranski-Krastanov method, are both considered. The dot is assumed to have shape similar to a cup, therefore it is effectively a composite structure of a ring and a disk inside the ring opening. Also, the dimensions of the structure taken in the calculations are similar to those of the fabricated structures. For constant outer radius of the ring ($R_2 = 100$ nm) the calculations show that only rather narrow rings ($W < 5$ nm) exhibit localizations of the electron and the hole inside the disk. For constant width of the ring, and varying the radius of the disk, the ground states of the electron and the hole are found to slightly increase in energy. Furthermore, when the height of the disk increases, the electron and hole energy levels do not appreciably change. Only when the disk height exceeds approximately 90% of the ring height, the probability to find the electron in the disk exceeds the probability to find the electron in the ring. But in rings of smaller lateral size and larger height, a crossing of the hole states with the disk height is found. Our calculations indicate that the presence of a layer inside the opening of the GaAs/(Al,Ga)As rings fabricated by droplet epitaxy is not detrimental to their electronic structure. Also, the electronic structure and the related optical properties of the ringlike quantum dot could be efficiently engineered by varying its dimensions.

In Chapter 7 the electronic structure of the unstrained GaAs/(Al,Ga)As and the strained

(In,Ga)As/GaAs ringlike quantum dots in perpendicular magnetic field is investigated. Our calculations show that the angular momentum transitions shift when the disk thickness increases. Because of strain, the hole is preferentially localized inside the disk of the (In,Ga)As/GaAs ringlike quantum dot, which leads to a large shift of the angular momentum transitions when the disk thickness exceeds already one fifth of ring height. On the other hand, the angular momentum shifts in the valence band of the unstrained GaAs/(Al,Ga)As quantum dots are small even for the disk as thick as half the ring height. Similar behavior of the conduction band states is found in both analyzed systems. Therefore, by increasing the disk thickness in the strained quantum dot, the electron ground energy may stay oscillatory (like in the quantum ring), whereas the hole ground energy level becomes a monotonic function of the magnetic field (like in a singly connected quantum dot). Such variations are associated with the dominant localization of the hole inside the disk, and the electron in the ring. Therefore, strain could lead to a spatial separation of the electron and the hole, thereby increasing the polarization of the exciton, which is beneficial for the appearance of the excitonic Aharonov-Bohm effect. Furthermore, the detailed geometry of the quantum dot is found to have a small effect on the magnetic field dependence of the hole energy levels.

References

- [1] G. E. Moore, “Cramming more components onto integrated circuits,” *Electronics* **38**, 114–117 (1965).
- [2] D. A. Broido and L. J. Sham, “Effective masses of holes at GaAs-AlGaAs heterojunctions,” *Phys. Rev. B* **31**, 888–892 (1985).
- [3] E. G. Barbagiovanni, D. J. Lockwood, P. J. Simpson, and L. V. Goncharova, “Quantum confinement in Si and Ge nanostructures: Theory and experiment,” *Appl. Phys. Rev.* **1**, 011 302 (47 p.) (2014).
- [4] C. Yang, C. Barrelet, F. Capasso, and C. Lieber, “Single p-type/intrinsic/n-type silicon nanowires as nanoscale avalanche photodetectors,” *Nano Lett.* **6**, 2929–2934 (2006).
- [5] R. Rölver, B. Berghoff, D. L. Bätzner, B. Spangenberg, and H. Kurz, “Lateral Si/SiO₂ quantum well solar cells,” *Appl. Phys. Lett.* **92**, 212 108 (3 p.) (2008).
- [6] H. Liu, T. Wang, Q. Jiang, R. Hogg, F. Tutu, F. Pozzi, and A. Seeds, “Long-wavelength InAs/GaAs quantum-dot laser diode monolithically grown on Ge substrate,” *Nature Photon.* **5**, 416–419 (2011).
- [7] J. P. Colinge, C. W. Lee, A. Afzalian, N. D. Akhavan, R. Yan, I. Ferain, P. Razavi, B. O’Neill, A. Blake, M. White, A. M. Kelleher, B. McCarthy, and R. Murphy, “Nanowire transistors without junctions,” *Nat. Nanotechnol.* **5**, 225–229 (2010).
- [8] R. Baets, “Photonics: An ultra-small silicon laser,” *Nature (London)* **498**, 447–448 (2013).

- [9] T. Ando, A. B. Fowler, and F. Stern, “Electronic properties of two-dimensional systems,” *Rev. Mod. Phys.* **54**, 437–672 (1982).
- [10] A. G. U. Perera, W. Z. Shen, S. G. Matsik, H. C. Liu, M. Buchanan, and W. J. Schaff, “GaAs/AlGaAs quantum well photodetectors with a cutoff wavelength at 28 μm ,” *Appl. Phys. Lett.* **72**, 1596–1598 (1998).
- [11] C. Sirtori, H. Page, C. Becker, and V. Ortiz, “GaAs-AlGaAs quantum cascade lasers: physics, technology, and prospects,” *IEEE J. Quantum Elect.* **38**, 547–558 (2002).
- [12] S. Viefers, P. Koskinen, P. S. Deo, and M. Manninen, “Quantum rings for beginners: Energy spectra and persistent currents,” *Physica E* **21**, 1–35 (2004).
- [13] M. Bayer, M. Korkusinski, P. Hawrylak, T. Gutbrod, M. Michel, and A. Forchel, “Optical detection of the Aharonov-Bohm effect on a charged particle in a nanoscale quantum ring,” *Phys. Rev. Lett.* **90**, 186 801 (4 p.) (2003).
- [14] J. Climente, J. Planelles, and J. Movilla, “Magnetization of nanoscopic quantum rings and dots,” *Phys. Rev. B* **70**, 081 301(R) (4 p.) (2004).
- [15] F. Ding, B. Li, N. Akopian, U. Perinetti, A. Govorov, F. M. Peeters, C. C. B. Bufon, C. Deneke, S. Kiravittaya, Y. Chen, A. Rastelli, O. Schmidt, and V. Zwiller, “Gate controlled Aharonov-Bohm oscillations from single neutral excitons in quantum rings,” *Phys. Rev. B* **82**, 075 309 (8 p.) (2010).
- [16] S. S. Li and J. B. Xia, “Electronic states of InAs/GaAs quantum ring,” *J. Appl. Phys.* **89**, 3434–3437 (2001).
- [17] L. J. Lauhon, M. S. Gudixsen, D. Wang, and C. M. Lieber, “Epitaxial core-shell and core-multishell nanowire heterostructures,” *Nature (London)* **420**, 57–61 (2002).
- [18] J. Xiang, W. Lu, Y. Hu, Y. Wu, H. Yan, and C. M. Lieber, “Ge/Si nanowire heterostructures as high-performance field-effect transistors,” *Nature (London)* **441**, 489–493 (2006).

- [19] B. Tian, X. Zheng, T. J. Kempa, Y. Fang, N. Yu, G. Yu, J. Huang, and C. M. Lieber, “Coaxial silicon nanowires as solar cells and nanoelectronic power sources,” *Nature (London)* **449**, 885–890 (2007).
- [20] E. F. Steigmeier, R. Morf, D. Grützmacher, H. Auderset, B. Delley, , and R. Wes-sicken, “Light emission from a silicon quantum well,” *Appl. Phys. Lett.* **69**, 4165–4167 (1996).
- [21] P. Boucaud, M. E. Kurdi, and J. M. Hartmann, “Photoluminescence of a tensilely strained silicon quantum well on a relaxed SiGe buffer layer,” *Appl. Phys. Lett.* **85**, 46–48 (2004).
- [22] R. Rölver, B. Berghoff, D. Bätzner, B. Spangenberg, H. Kurz, B. Stegemann, and M. Schmidt, “Si/SiO₂ quantum wells for all silicon tandem solar cells: conductivity and photocurrent measurements,” *Thin Solid Films* **516**, 6763–6766 (2008).
- [23] B. Berghoff, S. Suckow, R. Rölver, B. Spangenberg, H. Kurz, A. Sologubenko, and J. Mayer, “Quantum wells based on Si/SiO_x stacks for nanostructured absorbers,” *Sol. Energ. Mat. Sol. C* **94**, 1893–1896 (2010).
- [24] Y. Takahashi, Y. Inui, M. Chihara, T. Asano, R. Terawaki, and S. Noda, “A micrometre-scale Raman silicon laser with a microwatt threshold,” *Nature (London)* **498**, 470–474 (2013).
- [25] D. Rideau, M. Feraille, L. Ciampolini, M. Minondo, C. Tavernier, H. Jaouen, and A. Ghetti, “Strained Si, Ge, and alloys modeled with a first-principles-optimized full-zone method,” *Phys. Rev. B* **74**, 195 208 (20 p.) (2006).
- [26] S. Lei and S. Nihtianov, “Comparative Study of Silicon-Based Ultraviolet Photodetectors,” *IEEE Sensors J.* **12**, 2453–2459 (2013).
- [27] M. Casalino, M. Iodice, L. Sirleto, I. Rendina, and G. Coppola, “Asymmetric MSM sub-bandgap all-silicon photodetector with low dark current,” *Opt. Express* **21**, 28 072–28 082 (2013).
- [28] Z. H. Lu, D. J. Lockwood, and J. M. Baribeau, “Quantum confinement and light emission in SiO₂/Si superlattices,” *Nature (London)* **378**, 258–260 (1995).

- [29] S. Saito, Y. Suwa, H. Arimoto, N. Sakuma, D. Hisamoto, H. Uchiyama, J. Yamamoto, T. Sakamizu, T. Mine, S. Kimura, T. Sugawara, and M. Aoki, “Stimulated emission of near-infrared radiation by current injection into silicon (100) quantum well,” *Appl. Phys. Lett.* **95**, 241 101 (3 p.) (2009).
- [30] A. W. Fang, H. Park, O. Cohen, R. Jones, M. J. Paniccia, , and J. E. Bowers, “Electrically pumped hybrid AlGaInAs-silicon evanescent laser,” *Opt. Express* **14**, 9203–9210 (2006).
- [31] A. Y. Liu, C. Zhang, J. Norman, A. Snyder, D. Lubyshev, J. M. Fastenau, A. W. K. Liu, A. C. Gossard, and J. E. Bowers, “High performance continuous wave 1.3 μm quantum dot lasers on silicon,” *Appl. Phys. Lett.* **104**, 041 104 (4 p.) (2014).
- [32] Y. H. Kuo, Y. K. Lee, Y. Ge, S. Ren, T. Kamins, D. A. B. Miller, and J. S. Harris, “Strong quantum-confined Stark effect in germanium quantum-well structures on silicon,” *Nature (London)* **437**, 1334–1336 (2005).
- [33] J. Kim and D. Ahn, “Effect of indirect interband absorption in Ge/SiGe quantum wells,” *J. Appl. Phys.* **110**, 083 119 (10 p.) (2011).
- [34] E. H. Edwards, L. Lever, E. T. Fei, T. I. Kamins, Z. Ikonić, J. S. Harris, R. W. Kelsall, and D. A. B. Miller, “Low-voltage broad-band electroabsorption from thin Ge/SiGe quantum wells epitaxially grown on silicon,” *Opt. Express* **21**, 867–876 (2013).
- [35] C. K. Chan, H. Peng, G. Liu, K. McIlwrath, X. F. Zhang, R. A. Huggins, and Y. Cui, “High-performance lithium battery anodes using silicon nanowires,” *Nat. Nanotechnol.* **3**, 31–35 (2008).
- [36] A. C. H. Rowe, “Silicon nanowires feel the pinch,” *Nat. Nanotechnol.* **3**, 311–312 (2008).
- [37] F. A. Zwanenburg, A. S. Dzurak, A. Morello, M. Y. Simmons, L. C. L. Hollenberg, G. Klimeck, S. Rogge, S. N. Coppersmith, and M. A. Eriksson, “Silicon quantum electronics,” *Rev. Mod. Phys.* **85**, 961–1019 (2013).

- [38] B. M. Maune, M. G. Borselli, B. Huang, T. D. Ladd, P. W. Deelman, K. S. Holabird, A. A. Kiselev, I. Alvarado-Rodriguez, R. S. Ross, A. E. Schmitz, M. Sokolich, C. A. Watson, M. F. Gyure, and A. T. Hunter, “Coherent singlet-triplet oscillations in a silicon-based double quantum dot,” *Nature (London)* **481**, 344–347 (2012).
- [39] B. Weber, Y. H. M. Tan, S. Mahapatra, T. F. Watson, H. Ryu, R. Rahman, L. C. L. Hollenberg, G. Klimeck, and M. Y. Simmons, “Spin blockade and exchange in Coulomb-confined silicon double quantum dots,” *Nat. Nanotechnol.* **9**, 430–435 (2014).
- [40] P. Vogt, P. D. Padova, C. Quaresima, J. Avila, E. Frantzeskakis, M. C. Asensio, A. Resta, B. Ealet, and G. L. Lay, “Silicene: Compelling Experimental Evidence for Graphenelike Two-Dimensional Silicon,” *Phys. Rev. Lett.* **108**, 155 501 (5 p.) (2012).
- [41] B. Lalmi, H. Oughaddou, H. Enriquez, A. Kara, S. B. Vizzini, B. N. Ealet, and B. Aufray, “Epitaxial growth of a silicene sheet,” *Appl. Phys. Lett.* **97**, 223 109 (2 p.) (2010).
- [42] A. Resta, T. Leoni, C. Barth, A. Ranguis, C. Becker, T. Bruhn, P. Vogt, and G. L. Lay, “Atomic Structures of Silicene Layers Grown on Ag(111): Scanning Tunneling Microscopy and Noncontact Atomic Force Microscopy Observations,” *Sci. Rep.* **3**, 2399 (2013).
- [43] E. Cinquanta, E. Scalise, D. Chiappe, C. Grazianetti, B. Broek, M. Houssa, M. Fanciulli, and A. Molle, “Getting through the Nature of Silicene: An sp^2 – sp^3 Two-Dimensional Silicon Nanosheet,” *J. Phys. Chem. C* **117**, 16 719–16 724 (2013).
- [44] R. Quhe, Y. Yuan, J. Zheng, Y. Wang, Z. Ni, J. Shi, D. Yu, J. Yang, and J. Lu, “Does the Dirac Cone Exist in Silicene on Metal Substrates?” *Sci. Rep.* **4**, 5476 (8 p.) (2014).
- [45] K. Takeda and K. Shiraishi, “Theoretical possibility of stage corrugation in Si and Ge analogs of graphite,” *Phys. Rev. B* **50**, 14 916–14 922 (1994).

- [46] G. G. Guzmán-Verri and L. C. L. Y. Voon, “Electronic structure of silicon-based nanostructures,” *Phys. Rev. B* **76**, 075 131 (10 p.) (2007).
- [47] B. Feng, Z. Ding, S. Meng, Y. Yao, X. He, P. Cheng, L. Chen, and K. Wu, “Evidence of Silicene in Honeycomb Structures of Silicon on Ag(111),” *Nano Lett.* **12**, 3507–3511 (2012).
- [48] P. D. Padova, C. Ottaviani, C. Quaresima, B. Olivieri, P. Imperatori, E. Salomon, T. Angot, L. Quagliano, C. Romano, and A. Vona, “24 h stability of thick multilayer silicene in air,” *2D Mater.* **1**, 021 003 (11 p.) (2014).
- [49] D. Jose and A. Datta, “Structures and Chemical Properties of Silicene: Unlike Graphene,” *Acc. Chem. Res.* **47**, 593–602 (2014).
- [50] L. Chen, C. C. Liu, B. Feng, X. He, P. Cheng, Z. Ding, S. Meng, Y. Yao, and K. Wu, “Evidence for Dirac Fermions in a Honeycomb Lattice Based on Silicon,” *Phys. Rev. Lett.* **109**, 056 804 (5 p.) (2012).
- [51] Z. Ni, H. Zhong, X. Jiang, R. Quhe, G. Luo, Y. Wang, M. Ye, J. Yang, J. Shi, and J. Lu, “Tunable band gap and doping type in silicene by surface adsorption: Towards tunneling transistors,” *Nanoscale* **6**, 7609–7618 (2014).
- [52] T. Hussain, T. Kaewmaraya, S. Chakraborty, and R. Ahuja, “Functionalization of hydrogenated silicene with alkali and alkaline earth metals for efficient hydrogen storage,” *Phys. Chem. Chem. Phys.* **15**, 18 900–18 905 (2013).
- [53] B. Berghoff, S. Suckow, R. Röfver, B. Spangenberg, H. Kurz, A. Sologubenko, and J. Mayer, “Improved charge transport through Si based multiple quantum wells with substoichiometric SiO_x barrier layers,” *J. Appl. Phys.* **106**, 083 706 (6 p.) (2009).
- [54] W. Shockley and H. J. Queisser, “Detailed balance limit of efficiency of p-n junction solar cells,” *J. Appl. Phys.* **32**, 510–519 (1961).
- [55] E. C. Cho, M. A. Green, R. Corkish, P. Reece, M. Gal, and S. H. Lee, “Photoluminescence in crystalline silicon quantum wells,” *J. Appl. Phys.* **101**, 024 321 (6 p.) (2007).

- [56] Z. H. Lu and D. Grozea, “Crystalline Si/SiO₂ quantum wells,” *Appl. Phys. Lett.* **80**, 255–257 (2002).
- [57] Y. Kanemitsu and S. Okamoto, “Photoluminescence from Si/SiO₂ single quantum wells by selective excitation,” *Phys. Rev. B* **56**, R15 561–R15 564 (1997).
- [58] H. Peelaers, B. Partoens, and F. M. Peeters, “Formation and segregation energies of B and P doped and BP codoped silicon nanowires,” *Nano Lett.* **6**, 2781–2784 (2006).
- [59] D. J. Lockwood and L. Tsybeskov, “Nanocrystalline Silicon Superlattices,” *Encyclopedia Nanosci. Nanotechnol.* **6**, 477–494 (2004).
- [60] S. Huang, H. Xiao, and S. Shou, “Annealing temperature dependence of Raman scattering in Si/SiO₂ superlattice prepared by magnetron sputtering,” *Appl. Surf. Sci.* **255**, 4547–4550 (2009).
- [61] E.-C. Cho, P. Reece, M. A. Green, J. Xia, R. Corkish, and M. Gal, “Clear quantum-confined luminescence from crystalline silicon/SiO₂ single quantum wells,” *Appl. Phys. Lett.* **84**, 2286–2288 (2004).
- [62] R. Rölver, O. Winkler, M. Först, B. Spangenberg, and H. Kurz, “Light emission from Si/SiO₂ superlattices fabricated by RPECVD,” *Microelectron. Reliab.* **45**, 915–918 (2005).
- [63] B. T. Sullivan, D. J. Lockwood, H. J. Labbé, and Z. H. Lu, “Photoluminescence in amorphous Si/SiO₂ superlattices fabricated by magnetron sputtering,” *Appl. Phys. Lett.* **69**, 3149–3151 (1996).
- [64] G. G. Qin, S. Y. Ma, Z. C. Ma, W. H. Zong, and Y. Li-ping, “Electroluminescence from amorphous Si/SiO₂ superlattices,” *Solid State Commun.* **106**, 329–333 (1998).
- [65] J. F. Ziegler, J. P. Biersack, and U. Littmark, *The Stopping and Range of Ions in Matter* (Pergamon Press, New York, 1985).

- [66] P. M. Martin, *Handbook of Deposition Technologies for Films and Coatings: Science, Applications and Technology* (Elsevier Inc., Oxford, 2010).
- [67] H. Xiao, S. Huang, J. Zheng, G. Xie, and Y. Xie, "Optical characteristics of Si/SiO₂ multilayers prepared by magnetron sputtering," *Microelectron. Eng.* **86**, 2342–2346 (2009).
- [68] S. Cosentino, M. Miritello, I. Crupi, G. Nicotra, F. Simone, C. Spinella, A. Terrasi, and S. Mirabella, "Room-temperature efficient light detection by amorphous Ge quantum wells," *Nanoscale Res. Lett.* **8**, 128 (7 p.) (2013).
- [69] Q. Zhang and S. C. Bayliss, "The correlation of dimensionality with emitted wavelength and ordering of freshly produced porous silicon," *J. Appl. Phys.* **79**, 1351–1365 (1996).
- [70] T. Mchedlidze, T. Arguirov, M. Kittler, R. Rölver, B. Berghoff, M. Först, and B. Spangenberg, "Structural and optical properties of Si/SiO₂ multi-quantum wells," *Phys. E* **38**, 152–155 (7 p.) (2007).
- [71] F. Iacona, G. Franzo, and C. Spinella, "Correlation between luminescence and structural properties of Si nanocrystals," *J. Appl. Phys.* **87**, 1295–1303 (2000).
- [72] D. J. Lockwood, "Quantum confined luminescence in Si/SiO₂ superlattices," *Phase Transitions* **68**, 151–168 (1999).
- [73] L. Heikkilä, T. Kuusela, H. P. Hedman, and H. Ihantola, "Electroluminescent SiO₂/Si superlattices prepared by low pressure chemical vapour deposition," *Appl. Surf. Sci.* **133**, 84–88 (1998).
- [74] R. Rölver, S. Brüninghoff, M. Först, B. Spangenberg, and H. Kurz, "Fabrication of a Si/SiO₂ multiple-quantum-well light emitting diode using remote plasma enhanced chemical vapor deposition," *J. Vac. Sci. Technol.* **23**, 3214–3218 (2005).
- [75] J. R. Arthur, "Molecular beam epitaxy," *Surf. Sci.* **500**, 189–217 (2002).

- [76] E. Søndergård, R. Kofman, P. Cheyssac, and A. Stella, “Production of nanostructures by self-organization of liquid Volmer-Weber films,” *Surf. Sci.* **364**, 467–476 (1996).
- [77] J. García, G. Medeiros-Ribeiro, K. Schmit, T. Ngo, J. L. Feng, A. Lorke, J. Kotthaus, and P. Petroff, “Intermixing and shape changes during the formation of InAs self-assembled quantum dots,” *Opt. Express* **71**, 2014–2016 (1997).
- [78] O. P. Pchelyakov, Y. B. Bolkhovityanov, A. V. Dvurechenskii, A. I. Nikiforov, A. I. Yakimov, and B. Voigtländer, “Molecular beam epitaxy of silicon–germanium nanostructures,” *Thin Solid Films* **367**, 75–84 (2000).
- [79] A. Lorke, J. Garcia, R. Blossey, R. Luyken, and P. Petroff, “Self-Organized InGaAs Quantum Rings - Fabrication and Spectroscopy,” *Adv. Sol. State. Phys.* **43**, 125–138 (2003).
- [80] V. M. Fomin, *Physics of quantum rings* (Springer, Berlin - Heidelberg, 2014).
- [81] A. Cho, “Morphology of epitaxial growth of GaAs by a molecular beam method: the observation of surface structures,” *J. Appl. Phys.* **41**, 2780–2786 (1970).
- [82] W. Braun, *Applied RHEED—Reflection High Energy Electron Diffraction During Crystal Growth* (Springer, Berlin, 1999).
- [83] G. Dhanaraj, K. Byrappa, V. Prasad, and M. Dudley, *Springer Handbook of Crystal Growth* (Springer, Berlin, 2010).
- [84] Z. H. Lu, D. J. Lockwood, and J. M. Baribeau, “Visible light emitting Si/SiO₂ superlattices,” *Solid State Electron.* **40**, 197–201 (1996).
- [85] M. Nastasi and J. W. Mayer, *Ion Implantation and Synthesis of Materials* (Springer, Berlin, 2006).
- [86] D. J. Lockwood, Z. H. Lu, and J. M. Baribeau, “Quantum Confined Luminescence in Si/SiO₂ Superlattices,” *Phys. Rev. Lett.* **76**, 539–541 (1996).

- [87] D. J. Lockwood, G. F. Grom, P. M. Fauchet, and L. Tsybeskov, "Ordering and self-organized growth of Si in the Si/SiO₂ superlattice system," *J. Cryst. Growth* **237**, 1898–1903 (2002).
- [88] Y. Kanemitsu and S. Okamoto, "Quantum confinement and interface effects on photoluminescence from silicon single quantum wells," *Solid State Commun.* **103**, 573–576 (1997).
- [89] D. J. Lockwood, Z. H. Lu, and D. H. Grozea, "Photoluminescence in crystalline-Si/SiO₂ quantum wells," *Proc. SPIE* **4808**, 40–44 (2002).
- [90] S. J. MacLeod, A. M. See, Z. K. Keane, P. Scriven, A. P. Micolich, M. Aagesen, P. E. Lindelof, and A. R. Hamilton, "Radio-frequency reflectometry on an undoped AlGaAs/GaAs single electron transistor," *Appl. Phys. Lett.* **104**, 012114 (3 p.) (2014).
- [91] S. P. DenBaars, C. A. Beyler, A. Hariz, and P. D. Dapkus, "GaAs/AlGaAs quantum well lasers with active regions grown by atomic layer epitaxy," *Appl. Phys. Lett.* **51**, 1530–1532 (1987).
- [92] T. Hayakawa, T. Suyama, K. Takahashi, M. Kondo, S. Yamamoto, and T. Hijikata, "Near-ideal low threshold behavior in (111) oriented GaAs/AlGaAs quantum well lasers," *Appl. Phys. Lett.* **52**, 339–341 (1988).
- [93] X. Dai, S. Zhang, Z. Wang, G. Adamo, H. Liu, Y. Huang, C. Couteau, and C. Soci, "GaAs/AlGaAs Nanowire Photodetector," *Nano Lett.* **14**, 2688–2693 (2014).
- [94] V. Shadrin and F. Serzhenko, "The theory of multiple quantum-well GaAs-AlGaAs infrared detectors," *Infrared Physics* **33**, 345–357 (1992).
- [95] J. Radovanović, A. Mirčetić, V. Milanović, Z. Ikonić, D. I. P. Harrison, and R. W. Kelsall, "Influence of the active region design on output characteristics of GaAs/AlGaAs quantum cascade lasers in a strong magnetic field," *Semicond. Sci. Technol.* **21**, 215–220 (2002).

- [96] J. Yoon, S. Jo, I. S. Chun, I. Jung, H. S. Kim, M. Meitl, E. Menard, X. Li, J. J. Coleman, U. Paik, and J. A. Rogers, “GaAs photovoltaics and optoelectronics using releasable multilayer epitaxial assemblies,” *Nature (London)* **465**, 329–333 (2010).
- [97] D. Yan, F. H. Pollak, T. P. Chin, and J. M. Woodall, “*In situ* study of Fermi-level pinning on n- and p-type GaAs (001) grown by molecular-beam epitaxy using photorefectance,” *Phys. Rev. Lett.* **52**, 4674–4676 (1995).
- [98] K. Fujiwara, H. T. Grahn, and K. H. Ploog, “Dynamical Stokes shift due to interface nanoroughness in growth islands of GaAs single quantum wells,” *Phys. Rev. B* **56**, 1081–1083 (1997).
- [99] J. Tersoff, M. D. Johnson, and B. G. Orr, “Adatom densities on GaAs: Evidence for near-equilibrium growth,” *Phys. Rev. Lett.* **78**, 282–285 (1997).
- [100] M. H. Zhang, L. W. Guo, H. W. Li, W. Li, Q. Huang, C. L. Bao, J. M. Zhou, B. L. Liu, Z. Y. Xu, Y. H. Zhang, and L. W. Lu, “Annealing-induced evolution of defects in low-temperature-grown GaAs-related materials,” *Phys. Rev. B* **63**, 115 324 (6 p.) (2001).
- [101] X. Li, Y. Liu, Z. Feng, F. Guo, Y. Zhao, R. Zhao, R. Zhou, C. Lou, and S. Zhang, “AlGaAs/GaAs quantum well infrared photodetector focal plane array based on MOCVD technology,” *Frontiers of Optoelectronics in China* **1**, 313–317 (2008).
- [102] W. D. Goodhue, “Using molecular-beam epitaxy to fabricate quantum-well devices,” *The Lincoln Laboratory Journal* **2**, 183–205 (1989).
- [103] Y. Horikoshi, M. Kawashima, and N. Kobayashi, “Optical investigation of GaAs growth process in molecular beam epitaxy and migration—enhanced epitaxy,” *J. Cryst. Growth* **111**, 200–204 (1991).
- [104] J. I. Climente, J. Planelles, and W. Jaskólski, “Magneto-optical transitions in nanoscopic rings,” *Phys. Rev. B* **68**, 075 307 (8 p.) (2003).
- [105] V. M. Fomin, V. N. Gladilin, S. N. Klimin, J. T. Devreese, N. A. J. M. Kleemans, and P. M. Koenraad, “Theory of electron energy spectrum and Aharonov-Bohm

- effect in self-assembled InGaAs quantum rings in GaAs,” *Phys. Rev. B* **76**, 235 320 (8 p.) (2007).
- [106] I. L. Kuskovsky, W. MacDonald, A. O. Govorov, L. Mourokh, X. Wei, M. C. Tamargo, M. Tadić, and F. M. Peeters, “Optical Aharonov-Bohm effect in stacked type-II quantum dots,” *Phys. Rev. B* **76**, 035 342 (6 p.) (2007).
- [107] M. Tadić, N. Čukarić, V. Arsoski, and F. M. Peeters, “Excitonic Aharonov-Bohm effect: Unstrained versus strained type-I semiconductor nanorings,” *Phys. Rev. B* **84**, 125 307 (13 p.) (2011).
- [108] N. A. J. M. Kleemans, I. M. A. Bominaar-Silkens, V. M. Fomin, V. N. Gladilin, D. Granados, A. G. Taboada, J. M. García, P. Offermans, U. Zeitler, P. Christianen, C. J. Maan, J. T. Devreese, and P. M. Koenraad, “Oscillatory persistent currents in self-assembled quantum rings,” *Phys. Rev. Lett.* **99**, 146 808 (4 p.) (2007).
- [109] C. A. Sackett, “Quantum physics: An atomic SQUID,” *Nature (London)* **505**, 166–167 (2014).
- [110] R. W. Simmonds, “Thermal physics: Quantum interference heats up,” *Nature (London)* **492**, 358–359 (2012).
- [111] Z. C. Wen, H. X. Wei, and X. F. Han, “Patterned nanoring magnetic tunnel junctions,” *Appl. Phys. Lett.* **91**, 122 511 (3 p.) (2007).
- [112] G. Huang, W. Guo, P. Bhattacharya, G. Ariyawansa, and A. G. U. Perera, “A quantum ring terahertz detector with resonant tunnel barriers,” *Appl. Phys. Lett.* **94**, 101 115 (3 p.) (2009).
- [113] T. Mano, T. Kuroda, K. Mitsuishi, M. Yamagiwa, X. J. Guo, K. Furuya, K. Sakoda, and N. Koguchi, “Ring-shaped GaAs quantum dot laser grown by droplet epitaxy: Effects of post-growth annealing on structural and optical properties,” *J. Cryst. Growth* **301-302**, 740–743 (2007).
- [114] C. Somaschini, S. Bietti, N. Koguchi, and S. Sanguinetti, “Fabrication of multiple concentric nanoring structures,” *Nano Lett.* **9**, 3419–3424 (2009).

- [115] C. Somaschini, S. Bietti, S. Sanguinetti, N. Koguchi, and A. Fedorov, “Self-assembled GaAs/AlGaAs coupled quantum ring-disk structures by droplet epitaxy,” *Nanotechnology* **21**, 125 601 (5 p.) (2010).
- [116] T. Mano, T. Kuroda, S. Sanguinetti, T. Ochiai, T. Tateno, J. Kim, T. Noda, M. Kawabe, K. Sakoda, G. Kido, and N. Koguchi, “Self-assembly of concentric quantum double rings,” *Nano Lett.* **5**, 425–428 (2005).
- [117] T. Mano and N. Koguchi, “Nanometer-scale GaAs ringstructure grown by droplet epitaxy,” *J. Cryst. Growth* **278**, 108–112 (2005).
- [118] A. Ohtake and N. Koguchi, “Two types of structures for the GaAs(001)-c(4×4) surface,” *Appl. Phys. Lett.* **83**, 5193–5195 (2003).
- [119] K. Watanabe, N. Koguchi, and Y. Gotoh, “Fabrication of GaAs quantum dots by modified droplet epitaxy,” *Jpn. J. Appl. Phys.* **39**, L79–L81 (2000).
- [120] M. Yamagiwa, T. Mano, T. Kuroda, T. Takeno, K. Sakoda, G. Kido, N. Koguchi, and F. Minami, “Self-assembly of laterally aligned GaAs quantum dot pairs,” *Appl. Phys. Lett.* **89**, 113 115 (3 p.) (2006).
- [121] P. Offermans, P. M. Koenraad, J. H. Wolter, D. Granados, J. M. García, V. M. Fomin, V. N. Gladilin, and J. T. Devreese, “Atomic-scale structure of self-assembled In(Ga)As quantum rings in GaAs,” *Appl. Phys. Lett.* **87**, 131 902 (3 p.) (2005).
- [122] J.-H. Dai, J. H. Lee, , and S.-C. Lee, “Annealing effect on the formation of In(Ga)As quantum rings from InAs quantum dots,” *IEEE Phot. Tech. Lett.* **20**, 165–167 (2008).
- [123] V. Arsoski, M. Tadić, and F. M. Peeters, “Strain and band-mixing effects on the excitonic Aharonov-Bohm effect in In(Ga)As/GaAs ringlike quantum dots,” *Phys. Rev. B* **87**, 085 314 (14 p.) (2013).
- [124] N. Čukarić, V. Arsoski, M. Tadić, and F. M. Peeters, “Hole states in nanocups in a magnetic field,” *Phys. Rev. B* **85**, 235 425 (11 p.) (2012).

- [125] P. Y. Yu and M. Cardona, *Fundamentals of semiconductors - physics and material properties* (Springer, Berlin, 2010).
- [126] L. P. H. W. C. O'Mara, R. B. Herring, *Handbook of semiconductor silicon technology* (Noyes Publications, 1990).
- [127] <http://en.wikipedia.org/wiki/User:Benjah-bmm27>.
- [128] S. Richard, F. Aniel, and G. Fishman, "Energy-band structure of Ge, Si, and GaAs: A thirty-band $\mathbf{k} \cdot \mathbf{p}$ method," *Phys. Rev. B* **70**, 235 204 (6 p.) (2004).
- [129] Z. Wu, J. B. Neaton, and J. C. Grossman, "Quantum confinement and electronic properties of tapered silicon nanowires," *Phys. Rev. Lett.* **100**, 246 804 (4 p.) (2008).
- [130] J. P. Proot, C. Delerue, and G. Allan, "Electronic structure and optical properties of silicon crystallites: Application to porous silicon," *Appl. Phys. Lett.* **61**, 1948–1950 (1992).
- [131] C. Delerue, M. Lannoo, and G. Allan, "Excitonic and quasiparticle gaps in Si nanocrystals," *Phys. Rev. Lett.* **84**, 2457–2460 (2000).
- [132] M. E. Kurdi, S. Sauvage, G. Fishman, and P. Boucaud, "Band-edge alignment of SiGe/Si quantum wells and SiGe/Si self-assembled islands," *Phys. Rev. B* **73**, 195 327 (9 p.) (2006).
- [133] F. Michelini and I. Ouerghi, "Interband optical properties of silicon [001] quantum wells using a two-conduction-band $\mathbf{k} \cdot \mathbf{p}$ model," *Appl. Phys. Lett.* **99**, 221 912(3 p.) (2011).
- [134] N. A. Čukarić, M. Ž. Tadić, B. Partoens, and F. M. Peeters, "The interband optical absorption in silicon quantum wells: Application of the 30-band $\mathbf{k} \cdot \mathbf{p}$ model," *Appl. Phys. Lett.* **104**, 242 103 (5 p.) (2014).
- [135] O. Demichel, F. Oehler, P. Noe, V. Calvo, N. Pauc, P. Gentile, T. Baron, D. Peyrade, and N. Magnea, "Photoluminescence of confined electron-hole plasma in core-shell silicon/silicon oxide nanowires," *Appl. Phys. Lett.* **93**, 213 104 (3 p.) (2008).

- [136] F. Voigt, V. Sivakov, V. Gerliz, G. H. Bauer, B. Hoffmann, G. Z. Radnoczi, B. Pecz, and S. Christiansen, “Photoluminescence of samples produced by electroless wet chemical etching: Between silicon nanowires and porous structures,” *Phys. Stat. Sol.* **208**, 893–899 (2011).
- [137] D. C. Hannah, J. Yang, P. Podsiadlo, M. K. Chan, A. Demortière, D. J. Gosztola, V. B. Prakapenka, G. C. Schatz, U. Kortshagen, and R. D. Schaller, “On the Origin of Photoluminescence in Silicon Nanocrystals: Pressure-Dependent Structural and Optical Studies,” *Nano Lett.* **12**, 4200–4205 (2012).
- [138] H. Kallel, A. Arbouet, M. Carrada, G. B. Assayag, A. Chehaidar, P. Periwal, T. Baron, P. Normand, and V. Paillard, “Photoluminescence enhancement of silicon nanocrystals placed in the near field of a silicon nanowire,” *Phys. Rev. B* **88**, 081 302(R) (5 p.) (2013).
- [139] I. Vurgaftman, J. R. Meyer, and L. R. Ram-Mohan, “Band parameters for III–V compound semiconductors and their alloys,” *J. Appl. Phys.* **89**, 5815–5875 (2001).
- [140] W. Desrat, D. K. Maude, Z. R. Wasilewski, R. Airey, and G. Hill, “Dresselhaus spin-orbit coupling in a symmetric (100) GaAs quantum well,” *Phys. Rev. B* **74**, 193 317 (4 p.) (2006).
- [141] Y. Hao, “Rashba and Dresselhaus spin-orbit interaction in semiconductor quantum wells,” *Eur. Phys. J. B* **85**, 84 (7 p.) (2012).
- [142] I. Saïdi, S. B. Radhia, and K. Boujdaria, “Band parameters of GaAs, InAs, InP, and InSb in the 40-band $\mathbf{k} \cdot \mathbf{p}$ model,” *J. Appl. Phys.* **107**, 043 701 (8 p.) (2010).
- [143] N. Fraj, I. Saïdi, S. B. Radhia, and K. Boujdaria, “Band structures of AlAs, GaP, and SiGe alloys: A 30 $\mathbf{k} \times \mathbf{p}$ model,” *J. Appl. Phys.* **102**, 053 703 (6 p.) (2007).
- [144] A. R. Denton and N. W. Ashcroft, “Vegard’s law,” *Phys. Rev. A* **43**, 3161–3164 (1991).
- [145] F. B. Pedersen and Y. C. Chang, “Energy levels of one and two holes in parabolic quantum dots,” *Phys. Rev. B* **53**, 1507–1516 (1996).

- [146] M. E. Kurdi, G. Fishman, S. Sauvage, and P. Boucaud, “Comparison between 6-band and 14-band $\mathbf{k} \cdot \mathbf{p}$ formalisms in SiGe/Si heterostructures,” *Phys. Rev. B* **68**, 16 533 (16 p.) (2003).
- [147] V. V. Kishore, N. Čukarić, B. Partoens, M. Tadić, and F. M. Peeters, “Hole subbands in freestanding nanowires: six-band versus eight-band $\mathbf{k} \cdot \mathbf{p}$ modelling,” *J. Phys. Condens. Matter* **24**, 135 302 (10 p.) (2012).
- [148] E. O. Kane, “Band structure of indium antimonide,” *J. Phys. Chem. Sol.* **1**, 249–261 (1957).
- [149] G. Dresselhaus, A. Kip, and C. Kittel, “Cyclotron resonance of electrons and holes in silicon and germanium crystals,” *Phys. Rev.* **98**, 368–384 (1955).
- [150] J. M. Luttinger and W. Kohn, “Motion of Electrons and Holes in Perturbed Periodic Fields,” *Phys. Rev.* **97**, 869–883 (1955).
- [151] F. Stern and R. M. Talley, “Impurity Band in Semiconductors with Small Effective Mass,” *Phys. Rev.* **100**, 1638–1643 (1955).
- [152] S. Datta and B. Das, “Electronic analog of the electrooptic modulator,” *Appl. Phys. Lett.* **56**, 665–667 (1990).
- [153] D. Grundler, “Large Rashba Splitting in InAs Quantum Wells due to Electron Wave Function Penetration into the Barrier Layers,” *Phys. Rev. Lett.* **84**, 6074–6077 (2000).
- [154] J. Fabian, A. M.-Abiaguea, C. Ertlera, P. Stanoa, and I. Žutić, “Semiconductor Spintronics,” *Acta Phys. Slovaca* **57**, 565–907 (2007).
- [155] V. V. R. Kishore, B. Partoens, and F. M. Peeters, “Electronic structure and optical absorption of GaAs/Al_xGa_{1-x}As and GaAsAl_xGa_{1-x}As/GaAs core-shell nanowires,” *Phys. Rev. B* **82**, 235 425 (9 p.) (2010).
- [156] N. Čukarić, M. Tadić, and F. M. Peeters, “Electron and hole states in a quantum ring grown by droplet epitaxy: Influence of the layer inside the ring opening,” *Superlattices Microstruct.* **48**, 491–501 (2010).

- [157] O. Stier, M. Grundmann, and D. Bimberg, “Electronic and optical properties of strained quantum dots modeled by 8-band $\mathbf{k} \cdot \mathbf{p}$ theory,” *Phys. Rev. B* **59**, 5688–5701 (1999).
- [158] V. Mlinar, M. Tadić, B. Partoens, and F. M. Peeters, “Nonsymmetrized Hamiltonian for semiconducting nanostructures in a magnetic field,” *Phys. Rev. B* **71**, 205 305 (12 p.) (2005).
- [159] S. Tomić, “Intermediate-band solar cells: Influence of band formation on dynamical processes in InAs/GaAs quantum dot arrays,” *Phys. Rev. B* **82**, 195 321 (15 p.) (2010).
- [160] M. Tadić and F. M. Peeters, “Binding of electrons, holes, and excitons in symmetric strained InP/In_{0.49}Ga_{0.51}P triple quantum-dot molecules,” *Phys. Rev. B* **70**, 195 302 (11 p.) (2004).
- [161] B. A. Foreman, “Effective-mass Hamiltonian and boundary conditions for the valence bands of semiconductor microstructures,” *Phys. Rev. B* **48**, 4964–4967 (1993).
- [162] D. W. Bailey, C. J. Stanton, and K. Hess, “Numerical studies of femtosecond carrier dynamics in GaAs,” *Phys. Rev. B* **42**, 3423–3434 (1990).
- [163] N. Fraj, I. Saïdi, S. B. Radhia, and K. Boujdaria, “Band parameters of AlAs, Ge and Si in the 34-band $\mathbf{k} \cdot \mathbf{p}$ model,” *Semicond. Sci. Technol.* **23**, 085 006 (6 p.) (2008).
- [164] M. Cardona and F. H. Pollak, “Energy band structure of germanium and silicon: the $\mathbf{k} \cdot \mathbf{p}$ method,” *Phys. Rev.* **142**, 530–543 (1966).
- [165] S. Richard, F. Aniel, and G. Fishman, “Band diagrams of Si and Ge quantum wells via the 30-band $\mathbf{k} \cdot \mathbf{p}$ method,” *Phys. Rev. B* **72**, 245 316 (7 p.) (2005).
- [166] N. A. Čukarić, M. Ž. Tadić, B. Partoens, and F. M. Peeters, “30-band $\mathbf{k} \cdot \mathbf{p}$ model of electron and hole states in silicon quantum wells,” *Phys. Rev. B* **88**, 205 306 (8 p.) (2013).

- [167] R. Winkler, *Spin-orbit coupling effects in two-dimensional electron and hole systems* (Springer, Berlin, 2003).
- [168] L. C. L. Y. Voon and M. Willatzen, *The $\mathbf{k} \cdot \mathbf{p}$ method: Electronic properties of semiconductors* (Springer, Berlin, 2008).
- [169] C. R. Pidgeon and R. N. Brown, “Interband magneto-absorption and Faraday rotation in InSb,” *Phys. Rev.* **146**, 575–583 (1966).
- [170] G. Bastard, *Wave Mechanics Applied to Semiconductor Heterostructures* (Les Editions de Physique, Les Ulis Cedex, 1988).
- [171] J. J. Sakurai, *Modern Quantum Mechanics* (Addison-Wesley, Reading, Massachusetts, 1994).
- [172] T. B. Badher, “Eight-band $\mathbf{k} \cdot \mathbf{p}$ model of strained zinc-blende crystals,” *Phys. Rev. B* **41**, 11 992–12 001 (1990).
- [173] S. Boyer-Richard, F. Raouafi, A. Bondi, L. Pédesseau, C. Katan, J.-M. Jancu, and J. Even, “30-band $\mathbf{k} \cdot \mathbf{p}$ method for quantum semiconductor heterostructures,” *Appl. Phys. Lett.* **98**, 251 913 (3 p.) (2011).
- [174] R. A. Morrow and K. R. Brownstein, “Model effective-mass Hamiltonians for abrupt heterojunctions and the associated wave-function-matching conditions,” *Phys. Rev. B* **30**, 678–680 (1984).
- [175] R. A. Morrow, “Establishment of an effective-mass Hamiltonian for abrupt heterojunctions,” *Phys. Rev. B* **35**, 8074–8079 (1987).
- [176] M. G. Burt, “The justification for applying the effective-mass approximation to microstructures,” *J. Phys. Condens. Matter* **4**, 6651–6690 (1992).
- [177] P. Lawaetz, “Valence-band parameters in cubic semiconductors,” *Phys. Rev. B.* **4**, 3460–3467 (1971).
- [178] G. L. Bir and G. E. Pikus, *Symmetry and Strain-induced Effects in Semiconductors* (Wiley, New York, 1974).

- [179] B. Jogai, “Three-dimensional strain field calculation in coupled InAs/GaAs quantum dots,” *J. Appl. Phys.* **88**, 5050–5055 (2000).
- [180] J. H. Davies, “Elastic and piezoelectric fields around a buried quantum dot: A simple picture,” *J. Appl. Phys.* **84**, 1358–1365 (1998).
- [181] P. N. Keating, “Effect of invariance Requirements on the elastic strain energy of crystals with application to the diamond structure,” *Phys. Rev.* **145**, 637–645 (1966).
- [182] J. D. Eshelby, “The Determination of the Elastic Field of an Ellipsoidal Inclusion, and Related Problems,” *Proc. R. Soc. Lond. A* **241**, 376–396 (1957).
- [183] M. Tadić, F. M. Peeters, K. L. Janssens, M. Korkusiński, and P. Hawrylak, “Strain and band edges in single and coupled cylindrical InAs/GaAs and InP/InGaP self-assembled quantum dots,” *J. Appl. Phys.* **92**, 5819–5829 (2002).
- [184] M. Tadić, F. M. Peeters, and K. L. Janssens, “Effect of isotropic versus anisotropic elasticity on the electronic structure of cylindrical InP/In_{0.49}Ga_{0.51}P self-assembled quantum dots,” *Phys. Rev. B* **65**, 165 333 (13 p.) (2002).
- [185] R. Eppeng, M. F. H. Schuurmans, and S. Colak, “New $\mathbf{k}\cdot\mathbf{p}$ theory for GaAs/Ga_{1-x}Al_xAs-type quantum wells,” *Phys. Rev. B* **36**, 1554–1564 (1987).
- [186] M. G. Burt, “Direct derivation of effective-mass equations for microstructures with atomically abrupt boundaries,” *Phys. Rev. B* **50**, 7518–7525 (1994).
- [187] B. A. Foreman, “Analytical envelope-function theory of interface band mixing,” *Phys. Rev. Lett.* **81**, 425–428 (1998).
- [188] M. G. Burt, “Fundamentals of envelope function theory for electronic states and photonic modes in nanostructures,” *J. Phys. Condens. Matter* **11**, R53–R83 (1999).
- [189] W. Yang and K. Chang, “Origin and elimination of spurious solutions of the eight-band $\mathbf{k}\cdot\mathbf{p}$ theory,” *Phys. Rev. B* **72**, 233 309 (4 p.) (2005).
- [190] B. A. Foreman, “Elimination of spurious solutions from eight-band $\mathbf{k}\cdot\mathbf{p}$ theory,” *Phys. Rev. B* **56**, R12 748–R12 751 (1997).

- [191] Q. Zhao, T. Mei, and D. H. Zhang, “Elimination of spurious solutions from $\mathbf{k}\cdot\mathbf{p}$ theory with Fourier transform technique and Burt-Foreman operator ordering,” *J. Appl. Phys.* **111**, 053 702 (7 p.) (2012).
- [192] R. G. Veprek, S. Steiger, and B. Witzigmann, “Ellipticity and the spurious solution problem of $\mathbf{k}\cdot\mathbf{p}$ envelope equations,” *Phys. Rev. B* **76**, 165 320 (9 p.) (2007).
- [193] T. Eissfeller and P. Vogl, “Real-space multiband envelope-function approach without spurious solutions,” *Phys. Rev. B* **84**, 195 122 (9 p.) (2011).
- [194] E. Bersch, S. Rangan, R. A. Bartynski, E. Garfunkel, and E. Vescovo, “Band offsets of ultrathin high- κ oxide films with Si,” *Phys. Rev. B* **78**, 085 114 (10 p.) (2008).
- [195] J. L. Alay and M. Hirose, “The valence band alignment at ultrathin SiO_2/Si interfaces,” *J. Appl. Phys.* **81**, 1606–1608 (1997).
- [196] G. L. Tan, M. F. Lemon, D. J. Jones, and R. H. French, “Optical properties and London dispersion interaction of amorphous and crystalline SiO_2 determined by vacuum ultraviolet spectroscopy and spectroscopic ellipsometry,” *Phys. Rev. B* **72**, 205 117 (10 p.) (2005).
- [197] C. L. Chuang, *Physics of Optoelectronic Devices* (Wiley, New York, 1995).
- [198] D. E. Aspnes and J. B. Theeten, “Spectroscopic analysis of the interface between Si and its thermally grown oxide,” *J. Electrochem. Soc.* **127**, 1359–1365 (1980).
- [199] M. Nishida, “Theoretical study of luminescence enhancement in oxidized $\text{Si}(001)$ ultrathin films,” *Phys. Rev. B* **58**, 7103–7112 (1998).
- [200] G. Dresselhaus, “Spin-Orbit Coupling Effects in Zinc Blende Structures,” *Phys. Rev.* **100**, 580–586 (1955).
- [201] U. Ekenberg and M. Altarelli, “Exciton binding energy in a quantum well with inclusion of valence-band coupling and nonparabolicity,” *Phys. Rev. B* **35**, 7585–7595 (1987).
- [202] U. Ekenberg, “Nonparabolicity effects in a quantum well: Sublevel shift, parallel mass, and Landau levels,” *Phys. Rev. B* **40**, 7714–7726 (1989).

- [203] W. Zawadski and P. Pfeffer, “Spin splitting of subband energies due to inversion asymmetry in semiconductor heterostructures,” *Semicond. Sci. Technol.* **19**, R1–R17 (2004).
- [204] D. M. Govzdić and U. Ekenberg, “Rapid spin flip in a spin subband at an anticrossing region in a slightly asymmetric modulation-doped quantum well,” *Physica E* **40**, 2081–2083 (2008).
- [205] B. Jia, Z. Yu, Y. Liu, W. Yao, H. Feng, and H. Ye, “Six-band $\mathbf{k} \cdot \mathbf{p}$ calculation of strained InAs/GaAs quantum rings,” *Superlattices Microstruct.* **47**, 714–722 (2010).
- [206] M. W. Kim and P. C. Ku, “Semiconductor nanoring lasers,” *Appl. Phys. Lett.* **98**, 201 105 (3 p.) (2011).
- [207] A. Lorke, R. Luyken, A. Govorov, J. Kotthaus, J. García, and P. Petroff, “Spectroscopy of nanoscopic semiconductor rings,” *Phys. Rev. Lett.* **84**, 2223–2226 (2000).
- [208] B. C. Lee, O. Voskoboynikov, and C. P. Lee, “III–V semiconductor nano-rings,” *Physica E* **24**, 87–91 (2004).
- [209] A. Chaplik, “Magnetoexcitons in quantum rings and in antidots,” *JETP Lett.* **62**, 885–889 (1995).
- [210] M. Grochol, F. Grosse, and R. Zimmermann, “Optical exciton Aharonov-Bohm effect, persistent current, and magnetization in semiconductor nanorings of type I and II,” *Phys. Rev. B* **74**, 115 416 (12 p.) (2006).
- [211] R. Okuyama, M. Eto, and H. Hyuga, “Optical Aharonov-Bohm effect on Wigner molecules in type-II semiconductor quantum dots,” *Phys. Rev. B* **83**, 195 311 (9 p.) (2011).
- [212] T. Lin, C. Lin, H. Ling, Y. Fu, W. Chang, S. Lin, and C. Lee, “Impacts of structural asymmetry on the magnetic response of excitons and biexcitons in single self-assembled In(Ga)As quantum rings,” *Phys. Rev. B* **80**, 081 304(R) (4 p.) (2009).

- [213] M. D. Teodoro, V. L. C. Jr., V. Lopez-Richard, E. M. Jr., G. E. Marques, G. Gobato, F. Iikawa, M. J. S. P. Brasil, Z. Y. AbuWaar, V. G. Dorogan, Y. I. Mazur, M. Benamara, and G. J. Salamo, “Aharonov-Bohm interference in neutral excitons: Effects of built-in electric fields,” *Phys. Rev. Lett.* **104**, 086 401 (4 p.) (2010).
- [214] L. M. Thu, W. T. Chiu, and O. Voskoboynikov, “Effects of geometrical shape dispersion on inhomogeneous broadening of excitonic peaks of semiconductor nano-objects,” *Phys. Rev. B* **83**, 125 301 (6 p.) (2011).
- [215] C. Y. Chao and S. L. Chuang, “Spin-orbit-coupling effects on the valence-band structure of strained semiconductor quantum wells,” *Phys. Rev. B.* **46**, 4110–4122 (1992).
- [216] J. Planelles, J. I. Climente, F. Rajadell, M. F. Doty, A. S. Bracker, and D. Gammon, “Effect of strain and variable mass on the formation of antibonding hole ground states in InAs quantum dot molecules,” *Phys. Rev. B.* **82**, 155 307 (8 p.) (2010).
- [217] J. Planelles and W. Jaskólski, “ $\mathbf{k} \cdot \mathbf{p}$ Hamiltonians for quantum dots in a magnetic field,” *J. Phys. Condens. Matter* **15**, L67–L75 (2003).
- [218] M. Bayer, A. Kuther, A. Forchel, A. Gorbunov, V. B. Timofeev, F. Schäfer, J. P. Reithmaier, T. L. Reinecke, and S. N. Walck, “Electron and hole g factors and exchange interaction from studies of the exciton fine structure in $\text{In}_{0.60}\text{Ga}_{0.40}\text{As}$ quantum dots,” *Phys. Rev. Lett.* **82**, 1748–1751 (1999).
- [219] E. Ribeiro, A. O. Govorov, W. C. Jr., and G. Medeiros-Ribeiro, “Aharonov-Bohm signature for neutral polarized excitons in type-II quantum dot ensembles,” *Phys. Rev. Lett.* **92**, 126 402 (4 p.) (2004).
- [220] A. O. Govorov, S. E. Ulloa, K. Karrai, and R. J. Warburton, “Polarized excitons in nanorings and the optical Aharonov-Bohm effect,” *Phys. Rev. B* **66**, 081 309(R) (4 p.) (2002).

Appendix A

Si, GaAs and AlAs band parameters

Table A.1: Band-edge states energies in Si , GaAs and AlAs.

Band-edge energies (eV)	Si [25]	GaAs [128]	AlAs [143]
Γ_{1l}	-12.7	-12.55	-11.95
Γ_{25l}	0.00	0.00	0.00
Γ_{15}	3.335	4.569	4.69
Γ_{2l}	4.15	1.519	3.13
Γ_{1u}	8.4	8.56	9.89
Γ_{12}	8.54	10.17	10.5
Γ_{25u}	11.7	11.89	12.5
Γ_{2u}	15.8	13.64	13.64

Table A.2: Nonzero spin-orbit coupling parameters in Si, GaAs and AlAs.

SO coupling strength (meV)	Si [25]	GaAs [128]	AlAs [143]
$\Delta_{\Gamma_{25l}}$	44	341	300
$\Delta_{\Gamma_{25u}}$	12	0	0
$\Delta_{\Gamma_{15}}$	33	81	150
$\Delta_{\Gamma_{25l}, \Gamma_{25u}}$	22	0	0

Table A.3: Nonzero matrix elements of linear momentum \mathbf{p} in Si, GaAs and AlAs.

Matrix element (eVnm)	Si [25]	GaAs [128]	AlAs [143]
$P_0 = \frac{\hbar}{m_0} \langle \Gamma_{25l} \mathbf{p} \Gamma_{2l} \rangle$	0.878	0.9232	0.8597
$P_1 = \frac{\hbar}{m_0} \langle \Gamma_{25u} \mathbf{p} \Gamma_{2l} \rangle$	-0.0058	0.0195	0.0617
$P_2 = \frac{\hbar}{m_0} \langle \Gamma_{25l} \mathbf{p} \Gamma_{2u} \rangle$	0.1123	0.4892	0.0349
$P_3 = \frac{\hbar}{m_0} \langle \Gamma_{25u} \mathbf{p} \Gamma_{2u} \rangle$	1.0255	0.9392	0.9762
$Q_0 = \frac{\hbar}{m_0} \langle \Gamma_{25l} \mathbf{p} \Gamma_{15} \rangle$	0.7686	0.7998	0.7379
$Q_1 = \frac{\hbar}{m_0} \langle \Gamma_{25u} \mathbf{p} \Gamma_{15} \rangle$	-0.4718	0.4068	0.5687
$R_0 = \frac{\hbar}{m_0} \langle \Gamma_{25l} \mathbf{p} \Gamma_{12} \rangle$	0.3906	0.4328	0.3899
$R_1 = \frac{\hbar}{m_0} \langle \Gamma_{25u} \mathbf{p} \Gamma_{12} \rangle$	0.6004	0.5819	0.5949
$T_0 = \frac{\hbar}{m_0} \langle \Gamma_{1u} \mathbf{p} \Gamma_{15} \rangle$	0.8392	0.8648	0.7808
$T_1 = \frac{\hbar}{m_0} \langle \Gamma_{1l} \mathbf{p} \Gamma_{15} \rangle$	0.2087	0.3045	0.2612
$S_0 = \frac{\hbar}{m_0} \langle \Gamma_{15} \mathbf{p} \Gamma_{2l} \rangle$	0	0.05 i	0.073 i

Nemanja Čukarić

Curriculum Vitae

Personal details

Born: 17.08.1985, Priština, Serbia

Address: School of Electrical engineering, Bulevar kralja Aleksandra 73, Belgrade

Phone: +381113218315

Email: nemanja.cukaric@etf.bg.ac.rs

Education

2008-2009 *MSc in Electrical Engineering, highest honors*

Department of Physical Electronics, School of Electrical Engineering,
University of Belgrade

2004-2008 *BSc in Electrical Engineering, highest honors*

Department of Physical Electronics, School of Electrical Engineering,
University of Belgrade

Work experience

2010-present *Teaching assistant*

Department of Physical Electronics, School of Electrical Engineering,
University of Belgrade

2009-2010 *Associate teaching assistant*

Department of Physical Electronics, School of Electrical Engineering,
University of Belgrade

Computer skills

Operating systems: Windows, Linux
Programming languages: C, Fortran
Mathematical software: Matlab, Mathematica, Comsol
Office: Word, Excel, PowerPoint
Other: Latex, CorelDraw, OriginPro

Languages

Serbian (native)
English (fluent)

List of Publications

1. N. A. Čukarić, M. Ž Tadić, B. Partoens, and F. M. Peeters, “*The interband optical absorption in silicon quantum wells: Application of the 30-band $\mathbf{k} \cdot \mathbf{p}$ model*”, Appl. Phys. Lett **104**, 242103 (5 p.) (2014). (Chapter 4)
2. N. A. Čukarić, M. Ž Tadić, B. Partoens, and F. M. Peeters, “*30-band $\mathbf{k} \cdot \mathbf{p}$ model of electron and hole states in silicon quantum wells*”, Phys. Rev. B **88**, 205306 (8 p.) (2013). (Chapter 3)
3. N. A. Čukarić, V. Arsoski, M. Ž Tadić, and F. M. Peeters, “*Hole states in nanocups in a magnetic field*”, Phys. Rev. B **85**, 235425 (11 p.) (2012). (Chapter 7)
4. V. V. Ravi Kishore, N. A. Čukarić, B. Partoens, M. Tadić, and F. M. Peeters, “*Hole subbands in freestanding nanowires: six-band versus eight-band $\mathbf{k} \cdot \mathbf{p}$ modelling*”, J. of Phys.: Condens. Matter **24**, 135302 (10 p.) (2012).
5. V. Arsoski, N. A. Čukarić, M. Tadić, and F. M. Peeters, “*Exciton states in a nanocup in the presence of a perpendicular magnetic field*”, Phys. Scripta **T149**, 014054 (5 p.) (2012).
6. M. Tadić, N. A. Čukarić, V. Arsoski, and F. M. Peeters, “*Excitonic Aharonov-Bohm effect: Unstrained versus strained type-I semiconductor nanorings*”, Phys. Rev. B **84**, 125307 (13 p.) (2011).
7. N. A. Čukarić, M. Ž Tadić, and F. M. Peeters, “*Electron and hole states in a quantum ring grown by droplet epitaxy: Influence of the layer inside the ring opening*”, Superlattices Microstruct. **48**, 491-501 (2010). (Chapter 6)
8. M. Tadić, V. Arsoski, N. A. Čukarić, and F. M. Peeters, “*The Optical excitonic Aharonov-Bohm Effect in a few nanometer wide type-I nanorings*”, Acta. Phys. Pol. A **117**, 947-977 (2010).
9. N. A. Čukarić and M. Ž Tadić, “*Multiband model of the valence-band electronic structure in cylindrical GaAs nanowires*”, HEM. IND. **64**, 165-170 (2010).

Прилог 1.

Изјава о ауторству

Потписани-а Nemanja Ćukarić

број индекса 2009/5030

Изјављујем

да је докторска дисертација под насловом

Modelovanje elektronskih i šupljinskih stanja u poluprovodničkim nanostrukturama pomoću višezonske k·p teorije

(Modelling the electron and hole states in semiconductor nanostructures by the multiband k·p theory)

- резултат сопственог истраживачког рада,
- да предложена дисертација у целини ни у деловима није била предложена за добијање било које дипломе према студијским програмима других високошколских установа,
- да су резултати коректно наведени и
- да нисам кршио/ла ауторска права и користио интелектуалну својину других лица.

Потпис докторанда

У Београду, 9.2.2015.



Прилог 2.

Изјава о истоветности штампане и електронске верзије докторског рада

Име и презиме аутора Nemanja Ćukarić

Број индекса 2009/5030

Студијски програм Nanoelektronika i fotonika

Наслов рада Modelovanje elektronskih i šupljinskih stanja u poluprovodničkim nanostrukturama pomoću višezonske k-p teorije (Modelling the electron and hole states in semiconductor nanostructures by the multiband k-p theory)

Ментор prof. dr Milan Tadić, prof. dr François Peeters

Потписани/а Nemanja Ćukarić

Изјављујем да је штампана верзија мог докторског рада истоветна електронској верзији коју сам предао/ла за објављивање на порталу **Дигиталног репозиторијума Универзитета у Београду**.

Дозвољавам да се објаве моји лични подаци везани за добијање академског звања доктора наука, као што су име и презиме, година и место рођења и датум одбране рада.

Ови лични подаци могу се објавити на мрежним страницама дигиталне библиотеке, у електронском каталогу и у публикацијама Универзитета у Београду.

Потпис докторанда

У Београду, 9. 2. 2015.



Прилог 3.

Изјава о коришћењу

Овлашћујем Универзитетску библиотеку „Светозар Марковић“ да у Дигитални репозиторијум Универзитета у Београду унесе моју докторску дисертацију под насловом:

Modelovanje elektronskih i šupljinskih stanja u poluprovodničkim nanostrukturama pomoću višezonske k·p teorije

(Modelling the electron and hole states in semiconductor nanostructures by the multiband k·p theory)

која је моје ауторско дело.

Дисертацију са свим прилозима предао/ла сам у електронском формату погодном за трајно архивирање.

Моју докторску дисертацију похрањену у Дигитални репозиторијум Универзитета у Београду могу да користе сви који поштују одредбе садржане у одабраном типу лиценце Креативне заједнице (Creative Commons) за коју сам се одлучио/ла.

1. Ауторство

2. Ауторство - некомерцијално

3. Ауторство – некомерцијално – без прераде

4. Ауторство – некомерцијално – делити под истим условима

5. Ауторство – без прераде

6. Ауторство – делити под истим условима

(Молимо да заокружите само једну од шест понуђених лиценци, кратак опис лиценци дат је на полеђини листа).

Потпис докторанда

У Београду, 9. 2. 2015.